Okinawa Institute of Science and Technology
Graduate University

Thesis submitted for the degree

Doctor of Philosophy

Evanescent Field Mediated Interactions of Cold Rubidium Atoms with Optical Nanofiber Guided Light

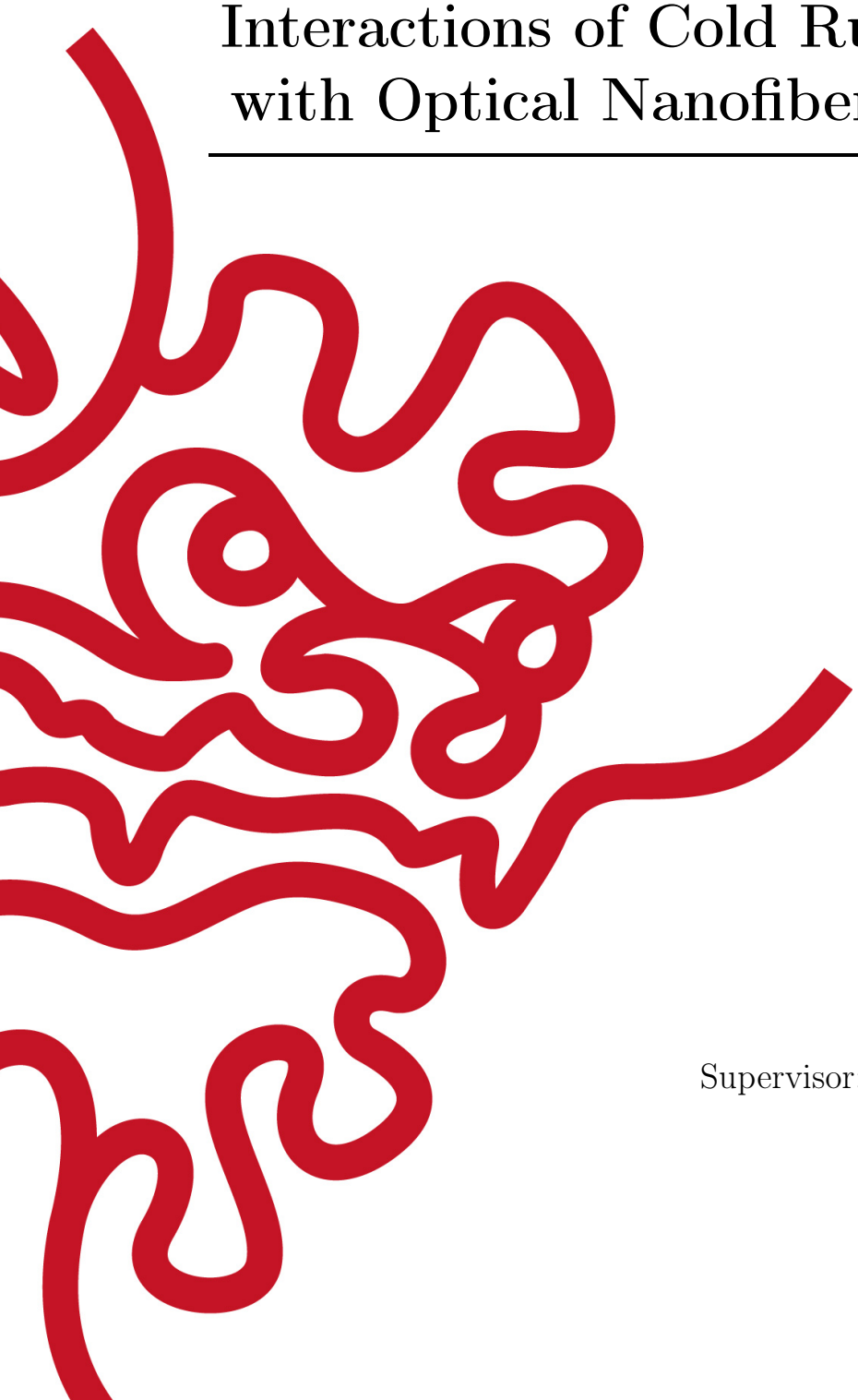

by

Ratnesh Kumar Gupta

Supervisor: **Prof. Síle Nic Chormaic**

May 2022

Declaration of Original and Sole Authorship

I, Ratnesh Kumar Gupta, declare that this thesis entitled *Evanescent Field Mediated Interactions of Cold Rubidium Atoms with Optical Nanofiber Guided Light* and the data presented in it are original and my own work. I confirm that:

- No part of this work has previously been submitted for a degree at this or any other university.
- References to the work of others have been clearly acknowledged. Quotations from the work of others have been clearly indicated, and attributed to them.
- In cases where others have contributed to part of this work, such contribution has been clearly acknowledged and distinguished from my own work.
- None of this work has been previously published elsewhere, with the exception of the following:
  - T. Ray, R.K. Gupta, V. Gokhroo, J.L. Everett, T. Nieddu, K.S. Rajasree and S. Nic Chormaic, "Observation of the ^{87}Rb $5S_{1/2} \rightarrow 4D_{3/2}$ electric quadrupole transition at 516.6 nm mediated via an optical nanofibre", New J. Phys. **22**, 062001 (2020) *Fast Track Communication*
  - K.S. Rajasree, R.K. Gupta, V. Gokhroo, F. Le Kien, T. Nieddu, T. Ray, S. Nic Chormaic and G. Tkachenko, "Spin selection in single-frequency two-photon excitation of alkali-metal atoms", Phys. Rev. Research **2**, 033341 (2020)
  - R.K. Gupta, J.L. Everett, A.D. Tranter, R. Henke, V. Gokhroo, P.K. Lam and S. Nic Chormaic, "Machine learner optimization of optical nanofiber-based dipole traps", AVS Quantum Sci. **4**, 026801 (2022)

Date: May 2022
Signature: Ratnesh K. Gupta

Abstract

Optical nanofibers (ONFs) have shown promising potential for quantum technology developments. The tight transverse confinement of guided light over an extended length ($> 1000\lambda$) offers strong atom-light interactions with potential long-range atom-atom interactions mediated by the guided light, allowing for better scalability in many quantum information applications than their corresponding free-space implementations. We demonstrated, experimentally, an electric quadrupole transition and a single-frequency two-photon transition in cold ^{87}Rb atoms driven by nanofiber-guided light, establishing ONFs as excellent platforms for potential applications in compact fiber-based clocks and correlated photon pair sources. ONFs are well-suited for nonlinear collective interactions, such as four-wave mixing and superradiance, that require an ensemble of phase-matched quantum emitters coupled to a common radiation field. An effective system is a 1D array of few hundred atoms trapped near an ONF surface and coupled with the guided mode. A crucial requirement is maximizing the number of trapped atoms which remains challenging in the absence of a quantitative description of atom dynamics during the trap-loading process involving many-body interactions and complex scattering process. We experimentally optimized, leveraging the ability of machine learning algorithms, the number of ^{87}Rb atoms loaded in a shallow fiber-based dipole trap by parametrizing the control of magneto-optical trap parameters. This sets the first step toward planned studies on optical nanofiber mediated collective atom-light interactions and nearest-neighbor interactions in a 1D lattice of Rydberg atoms.

Acknowledgment

First and foremost, I would like to offer my sincerest gratitude to my supervisor, Prof. Síle Nic Chormaic, who has supported me throughout my thesis with her patience and knowledge. Your tireless work in keeping the unit organized and motivated is truly amazing, and is key to the success enjoyed by myself and others. Thank you for accepting me as your PhD student and for the invaluable teachings, opportunities and exposure to the scientific research.

I would like to thank Prof. Thomas Busch and Prof. Keshav Dani for being on my thesis committee and offering support and suggestions time and again. I would also like to acknowledge the OIST Student Support section for their help in countless matters, making the life of an international student so much easier.

I thank Jesse, with whom I got to work closely, I have learned so much from you. Your knowledge in physics never ceases to amaze me. To Vandna, thank you for being there as a colleague and a guide. I would have broken without your support during my weakest times. I thank Thomas (Nieddu), Jinjin, Krishnapriya and Tridib for welcoming me into the cold atoms group. Thank you for many enjoyable lab sessions. To Georgiy, thank you. From you, I need to learn how to be very professional and organized with work.

I would like to extend my gratitude to all the group members. During these years, I had the pleasant opportunity to interact with and know many like Aili, Alex, Antoine, Aswathy, Cindy, Christina, Domna, Dylan, Fuchuan, Giang, Jameesh, Jean-Baptiste, Jibo, Jonathan (Ward), Ke Tian, Kristoffer, Lewis, Maki, Mark, Metin, Peter, Priscilla, Ramgopal, René, Shou, Theo, Xue, Zia, Zohreh and others. I would like to specially thank Jonathan (Ward) for being as amazing as you are. You are the most resourceful person I know, it is awesome to watch you build things in the lab. Last but not the least of all the group members, I would like to thank Emi, our research unit administrator, for helping me go through any administrative nightmares without ever complaining. I would like to pay my regards to Dr. Fam Le Kien for useful discussions whenever I approached him. I would also like to thank Aaron and Prof. Ping Koy Lam for their valuable suggestions and comments.

Many thanks to Prof. Aidan Arnold for being generous and giving me an opportunity to work in his lab at the University of Strathclyde in Glasgow. The experience was enriching. It was great interacting with a lovely bunch of people in the group. Special thanks to Rachel and Johnathan (Conway) for bringing me up to speed with the lab system. I take a moment to express my gratitude toward Prof. Sonja Franke-Arnold who arranged this opportunity in the first place.

With fondness, I thank Prof. Ayan Banerjee who has a big role in shaping where

I am today. A big thanks to Prof. David Dorfan for your guidance and inspiring confidence in me. I would like to pay special mention to my dear friends Anna, Justin, Matthew, Naman, Sanidhya, Sergey and Wasi. To Anna, thank you for your infectious energy. I have always enjoyed our banter. To Justin and Matthew, thank you both for all the great tea-time conversations. To Naman, for always being there. Your constant support and motivation means a lot. To Sanidhya and Wasi, for never letting me feel away from home. To Sergey, thank you for all those casual but intense philosophical discussions. This acknowledgement could not be complete without thanking my uncle, Dr. Rakesh Kumar Gupta, and my aunt, Sudha Gupta, who were always there for me and my family.

Finally, I mention the people for whom words cannot express my gratitude. To mummy, papa and Rashmi, thank you for your support throughout the years. I could not be here without your sacrifices. And to Sayu for always being by my side, for your help, and care. Love, support, and patience of you all is what keeps me going.

Abbreviations

4X	Four-way cross
6X	Six-way cross
ANN	Artificial neural networks
AOM	Acousto-optic modulator
AR	Anti-reflection
BS	Beam splitter
CBL	Coherent blue light
CF	ConFlat
CG	Clebsch-Gordon coefficients
CMOS	Complementary metal oxide semiconductor
CW	Continuous wave
DM	Dichroic mirror
ECDL	Extended cavity diode laser
EIT	Electromagnetically induced transparency
EM	Electromagnetic
EMCCD	Electron-multiplying charge coupled devices
FWHM	Full-width-half-maximum
FWM	Four-wave mixing
GELU	Gaussian error linear unit
GPIB	General purpose interface bus
GR	Ruled grating
HBT	Hanbury-Brown and Twiss
HWP	Half-wave plate
IGBT	Insulated-gate bipolar transistor
L-BFGS	Limited-memory Broyden-Fletcher-Goldfarb-Shanno algorithm
LG	Laguerre-Gaussian
ML	Machine learning
MOT	Magneto-optical trap
MSE	Mean squared error
NDF	Neutral density filters
NIR	Near-infrared
NPBS	Non-polarizing beam splitter
OAM	Orbital angular momentum
OBE	Optical Bloch equations
OD	Optical depth
ONF	Optical nanofiber

PBS	Polarizing beam splitter
PC	Polarization compensator
PD	Photodiode
PM	Polarization maintaining
PMT	Photo-multiplier tube
PNC	Parity non-conservation
QED	Quantum Electrodynamics
QWP	Quarter-wave plate
RMS	Root-mean-square
RWA	Rotating wave approximation
SANN	Stochastic artificial neural networks
SAS	Saturated absorption spectroscopy
SEM	Scanning electron microscope
SHG	Second harmonic generator
SIM	Scanning ion microscope
SLM	Spatial light modulation
SPCM	Single-photon counting module
SPD	Single-photon detectors
TA	Tapered amplifier
TTL	Transistor-transistor logic
UHV	Ultra high vacuum
VBG	Volume Bragg grating
VR	Variable retarder

Nomenclature

a	Radius of the fiber
$\alpha(\omega)$	Atomic polarizability
$\alpha(\omega_{\text{red}})$, $\alpha(\omega_{\text{blue}})$	Polarizabilities due to red- and blue-detuned light
β	Propagation constant of an optical mode
β_{jk}	Relative transition strength for $\|j\rangle \rightarrow \|k\rangle$ transition
$\mathcal{B}$	Magnetic field
c	Speed of light ($2.997\ 924\ 58 \times 10^{8}$ ms^{-1})
$\chi_{(3)}$	Susceptibility, third-order
$\|\|d\|\|$	Reduced dipole matrix element
$\mathbf{d}$	Electric dipole operator
$\delta\left(m_F, \boldsymbol{\mathcal{E}}_{\text{probe}}\right)$	Optical transition shift due to the trapping fields
Δ	Frequency detuning
e	Electric charge ($1.602\ 177 \times 10^{-19}$ C)
$\boldsymbol{\epsilon}$	Polarization vector
ϵ_0	Free space permittivity ($8.854\ 188 \times 10^{-12}$ Fm^{-1})
$\mathcal{E}$	Electric field amplitude
$\mathcal{E}_{\text{red}}$, $\mathcal{E}_{\text{blue}}$	Electric field amplitude of the red- and the blue-detuned field
$\boldsymbol{\mathcal{E}}$	Elecric field of a mode
$\boldsymbol{\mathcal{E}}_+, \boldsymbol{\mathcal{E}}_-$	Elecric field of a quasi-circularly polarized mode
E1	Electric dipole interaction
E2	Electric quadrupole interaction
η	Quantum efficiency of the detector
η_{osc}	Electric quadrupole oscillator strength enhancement factor
$f_{FF'}$	Quadrupole oscillator strength
$\mathbf{F}_{\text{dip}}$	Dipole force
$\mathbf{F}_{\text{sc}}$	Scattering force
γ	Coherence decay rate
Γ	Spontaneous decay rate
$\hbar$	Reduced Planck's constant ($1.054\ 572\ 66 \times 10^{-34}$ Js^{-1})
$\mathcal{H}$	Total Hamiltonian
$\mathcal{H}_{\mathcal{A}}$	Free-atom Hamiltonian
$\mathcal{H}_{\mathcal{I}}$	Atom-field interaction Hamiltonian
I	Electromagnetic field intensity
I_{sat}	Saturation intensity
$I_T(\Delta \neq 0)$	Transmitted intensity of off-resonant light
J_l	Bessel function of the first kind

k	Wavenumber of a light field
$\mathbf{k}$	Wavevector of a light field
k_B	Boltzmann constant ($1.380\ 648\ 5 \times 10^{-23}$ $\mathrm{Js^{-2}K^{-1}}$)
κ	Attenuation factor
K_l	Bessel function of the second kind
λ	Wavelength
m_a	Atomic mass
m_e	Mass of an electron ($9.109\ 383\ 56 \times 10^{-31}$ kg)
μ_B	Bohr magneton ($9.274\ 009 \times 10^{-24}$ $\mathrm{JT^{-1}}$)
n	Number density of atoms
n_1	Refractive index of the core
n_2	Refractive index of the cladding
N_{atoms}	Number of atoms in the cloud
od	Optical depth
ω	Angular frequency
ω_{eg}	Resonant angular frequency for ground to excited state transition
Ω	Rabi frequency
Ω_{eff}	Effective Rabi frequency
$\bar{\Omega}_{FF'}$	RMS Quadrupole Rabi frequency
P	Power of the radiated field
P_{ge}	Transition rate
$P_l(\cos\theta)$	Legendre Polynomial
Q_{ij}	Quadrupole tensor components
$\mathbf{r}$	Position vector
ρ	Density operator
$\boldsymbol{\rho}$	Thermal ensemble density
R_{jk}	Absorption rate for $\lvert j\rangle \rightarrow \lvert k\rangle$ transition
s	Saturation parameter
σ	Scattering cross-section
σ_0	Resonant absorption cross-section
σ_h	Helicity parameter of an optical field
$\sigma_x, \sigma_y, \sigma_z$	Pauli spin matrices
$\sigma_+(\sigma_-)$	Right (Left) circular polarization
$\hat{\sigma}_\pm$	Atomic transition operators
Σ_1, Σ_2	Summation of brightness of light scattered from the ONF
t_{sweep}	Duration of the *Sweep-phase* in the experimental sequence
t_{exp}	Exposure time of the camera
T_{cloud}	Temperature of the atom cloud
T_{avg}	Average temperature of the trapped atoms
Θ	Field-of-view of the imaging telescope
u_q	Spherical unit vector
U_{dip}, U_{vdW}	Dipole and van der Waals potential
$U(r, \phi, z)$	Ground-state potential at position (r, ϕ, z) given in cylindrical coordinates
V_{eg}	Two-photon transition operator
w_0	Beam waist diameter at focus
x_1, x_2, x_3	Cartesian coordinates

$Y_l^m(\theta, \phi)$	Spherical harmonic function
z_R	Rayleigh range

To Maa and Papa, for their endless love.

Contents

List of Figures

Chapter 1

Introduction

In recent years, quantum technologies [1] such as quantum control, quantum metrology [2], quantum communication [3] and quantum computation [4] have attracted immense interest. In the context of quantum communication, a significant goal has been the development of quantum networks [5] consisting of spatially separated quantum nodes interconnected by quantum channels. The information can be mapped to quantum states that are generated, manipulated, and stored in the quantum nodes, while quantum channels distribute this quantum information over the network via entanglement. A variety of candidates such as photons [6], neutral atoms [7], ions [8], nitrogen-vacancy centers in diamond [9], cavity quantum electrodynamics (QED) systems [10], and superconducting circuits [11] are being investigated for physical implementations. Each has its own advantages and disadvantages [12]. Photons are widely agreed to be the ideal candidate for transmitting quantum information as they travel quickly, interact weakly with the environment, and, therefore, do not decohere easily. Atomic internal states are well-suited for coherent manipulation and long-term storage of quantum information.

A key goal has been to realize an efficient interface for the coherent transfer of information between two systems, viz., photons and atoms. In that context, a strong interaction between atoms and photons has become an essential task to be achieved. The strength of the interaction is determined by the overlap between the transverse spread of the photonic mode and the atomic absorption cross-section ($\sigma_0 = 3\lambda^2/2\pi$) of resonant light with a wavelength λ. Therefore, a strong transverse confinement of photonic modes is an essential requirement for efficient interaction. In free-space, strong transverse confinement of a Gaussian mode may be achieved by tightly focusing the beam; however, it is achieved at the expense of the effective interaction volume, which depends on the Rayleigh range ($z_R = \pi w_0^2/\lambda$, where w_0 is the diameter of the transverse spread at the focus) of the focused beam. The strength may be enhanced by implementing a longitudinal confinement of the photonic mode in high-finesse optical cavities enabling multiple interactions between the photons and atoms confined within the cavity [5]. This has been investigated in numerous studies [10, 13, 14] over the past several decades, leading to the achievement of the ideal limit of single photon-single atom interactions, thereby opening opportunities for fundamental interaction studies [15], and several quantum computation and quantum networking schemes [16].

The quest for full control over the quantum state of cold atoms and photons has

evolved into the vision of what is called ensemble-based quantum information and quantum interfaces. These systems have demonstrated their potential with the successful experimental implementation of quantum memories [17], and single-photon generation [18]. A desired control over light-matter interactions in a dense atomic ensemble can be achieved by using electromagnetically induced transparency (EIT) [19] with applications in light storage [20, 21] and precision measurements [22]. As well as this, dense mesoscopic atom samples allow for the production of very long range Rydberg molecular states [23], and fast dipole-blockade based Rydberg quantum manipulation [24] becomes possible. These applications of cold and dense atomic ensembles require sophisticated cooling and trapping of cold atoms in an optical dipole trap lattice in which a few 100s of atoms are confined for long durations.

More recently, in the past decade, significant advances have been made toward the realization of hybrid quantum interfaces based on nanophotonic devices, waveguides, and cavities interfaced with quantum emitters. In particular, optical nanofibers (ONFs) have opened promising prospects for future developments in quantum technologies. Atoms coupled to ONFs (and nanofiber cavities) offer an alternative to the free-space, light-matter interfaces described before, as their effective interaction length can be several times longer than the Rayleigh length (z_R). Nanofiber optical modes feature diffraction-free strong transverse confinement, over the entire length of the subwavelength diameter section of the tapered optical fiber, leading to a strong interaction with atoms exposed to the evanescent field, thus achieving high optical depth (OD) with a few atoms. The spontaneous emission of atoms is strongly coupled to the nanofiber and is shown to be preferentially channelled to it [25, 26]. Atoms trapped in an evanescent field lattice around an ONF [27, 28] have long lifetimes and useful collective properties [29–31], while allowing direct integration into a fiber network, further increasing their attractiveness for practical quantum communication schemes.

In this thesis, we primarily explore evanescent field mediated interactions in cold rubidium atoms with nanofiber guided light, potentially extending the range of applications of the nanofiber-atom interface. The results of our studies are reported in subsequent chapters. Here, we start by introducing ONFs and their advantages as a platform for light interaction studies. This is followed by a brief review of research and applications of ONFs in atomic and quantum physics. The layout of the rest of the thesis is outlined at the end of the chapter.

1.1 ONF as a Light-Atom Interface: A Brief Review

A conventional step-index optical fiber tapered down to subwavelength diameter, referred to as an optical nanofiber (ONF), has gained much attention over the last decade, paving the way toward a versatile platform for quantum optics and sensing experiments. A schematic of an ONF is shown in Figure 1.1 The development in the manufacturing processes of such ultrathin fibers in the early 2000s [32, 33] have enabled us to produce adiabatically tapered ONFs with nearly 100% optical transmission. The adiabaticity here means that the optical field guided into the core of the standard step-index fiber is coupled to the optical mode guided in the subwavelength diameter region, i.e., the waist, of the ONF without any significant loss. Often we will use the term ONF to only

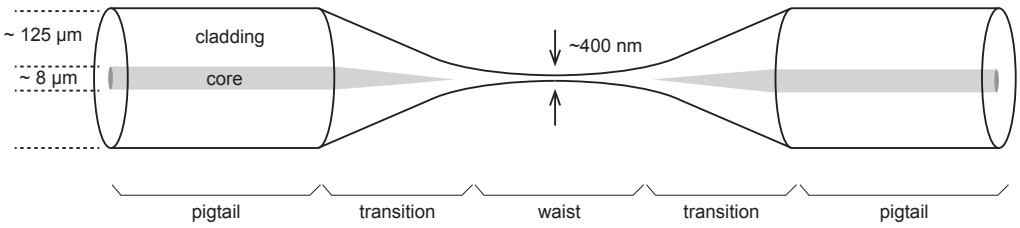

Figure 1.1: Schematic of a tapered optical fiber. A single-mode commercial fiber with typical diameter ∼125 µm is adiabatically tapered down to a subwavelength diameter of a few 100s of nanometers in the waist region. Typical dimensions of the core, cladding, and the waist of a single-mode ONF for 780 nm light are given.

refer to this waist region of the tapered fiber. A review by Ward et al. [34] discusses several ONF fabrication techniques.

As all the power coupled to the fiber can be adiabatically transfered to the ONF, ONFs feature strong transverse confinement and diffraction-free propagation of the guided optical mode. Additionally, a significant portion of the power propagates outside the ONF in the form of an intense evanescent field surrounding the fiber. It is worth noting that the medium surrounding the ONF (the core) is what forms the cladding for the step-index fiber structure supporting the mode-guiding. In addition, ONFs have excellent mechanical properties allowing them to be bent and manipulated without damage, thereby facilitating the fabrication of highly compact devices [35–37].

Following the theoretical proposal from Patnaik et al. [38] in 2002, a series of theoretical studies have been reported on the interaction of atoms with an ONF [26, 27, 39–41]. The ONFs enable interactions between the guided optical fields and the atoms, via the evanescent field, within a distance of a few hundred nanometers from the surface of the ONF. The effects of surface-atom interactions in the context of an ONF were investigated in a number of theoretical [25, 26, 39, 42–46] and experimental [47, 48] papers. It was demonstrated that the ONF modifies the boundary conditions and the density of modes, affecting the decay properties of the atoms. An apparent consequence is the modification of the spontaneous emission rate of atoms in the vicinity of an ONF, with the possibility of a significant fraction of the spontaneous emission being coupled to the guided mode of the ONF [26]. This was experimentally demonstrated by Nayak et al. [47]. The effects of van der Waals and Casimir-Polder forces manifest as a red-shifted asymmetry in the fluorescence spectra as shown by a series of theoretical works [42, 43]. Furthermore, it was shown that the Casimir-Polder force is negligible compared to the van der Waals interactions [42]. In a different research direction, for circularly polarized light confined in the fundamental mode of an ONF, theoretical calculations identified that the light possesses a finite angular momentum, with both spin and orbital components [40], which not only affects the internal state of an atom but also the center-of-mass motion, in particular rotating the atoms around the ONF [41].

Many pioneering experiments demonstrating atom-nanofiber interfaces have been undertaken since then and have enabled ONFs as a workbench for quantum optics studies and applications. With warm atoms, nonlinear optics was demonstrated [49,

50] showing, in particular, saturation effects at low power levels (nW). Morrissey et al. [51] measured several magneto-optical trap (MOT) characteristics such as MOT size, shape and atom number by collecting the fluorescence with the ONF. Das et al. [52] measured the fluorescence emission spectrum of a few atoms with an ONF combined with optical heterodyne and photon correlation spectroscopy, and measured the Mollow triplet spectrum of atoms at high excitation intensity. Nayak et al.[53] performed intensity autocorrelation measurements by splitting the coupled fluorescence on to a polarizing beam spitter (PBS) and detecting by two detectors in a Hanbury-Brown and Twiss (HBT) setup showing anti-bunching effects, revealing the presence of a single atom emitting photons into the guided mode. Grover et al. [54] performed a similar correlation measurement to measure the temperature of an atomic cloud. Another experiment performed in a cold ^{87}Rb atom cloud created in a MOT, measured the Autler-Townes splitting generating up-converted photons at 420 nm [55]. In a similar setup, Kumar et al. [56] realized electro-magnetically induced transparency (EIT) in a ladder configuration which they used to demonstrate optical switching in an all-fiber system.

Employing the trapping scheme proposed by Le Kien et al. [27], Cs atoms were trapped in a one-dimensional array around a nanofiber using ONF-guided fields [28]. The physical idea behind nanofiber-based trap is discussed in Section 1.3 which we followed for our implementation of a trap for Rb atoms (discussed in Chapter 6). The trapping of atoms around an ONF has provided an optically dense quantum interface, opening routes toward quantum nonlinear optics and cavity QED with atomic ensembles (see Figure 1.2). Photon storage experiments with an ensemble of trapped cold atoms were demonstrated where fiber-guided optical pulses at the single photon level were stored in the ensemble and retrieved on-demand [57].

Interactions between the nanofiber-guided mode and atoms could be further enhanced by combining the features of ONFs and cavities. Some proposals have highlighted the advantages of creating a cavity network in which each cavity is linked to others via fibers [59, 60]. In this regard, integrated cavity structures, either with fiber Bragg-gratings [61–65] or ring-cavities [66, 67], have been investigated (see Figure 1.3).

1.2 Collective Effects in an ONF-Atom System: Potential Applications in Quantum Information

With fiber-based traps as a stepping-stone, researchers were able to study collective near-resonant light scattering from a coherently driven ensemble of atoms. In a system with interatomic distances on the order of the wavelength of light or smaller, atom-atom correlations become significant. Chang et al. [58] theoretically showed that an ensemble of periodically arranged two-level atoms in an evanescent field lattice around an ONF can form an effective high-finesse cavity within the ONF using collective enhancement effects. Coherent Bragg scattering from an array of trapped atoms around an ONF was experimentally demonstrated [68, 69], paving the way toward strong coupling in 1D atom-photon systems. Corzo et al. [30] experimentally observed a single collective atomic excitation in an array of cesium atoms trapped along an ONF. The stored, collective entangled state can be efficiently read out, leading to on-demand emission of

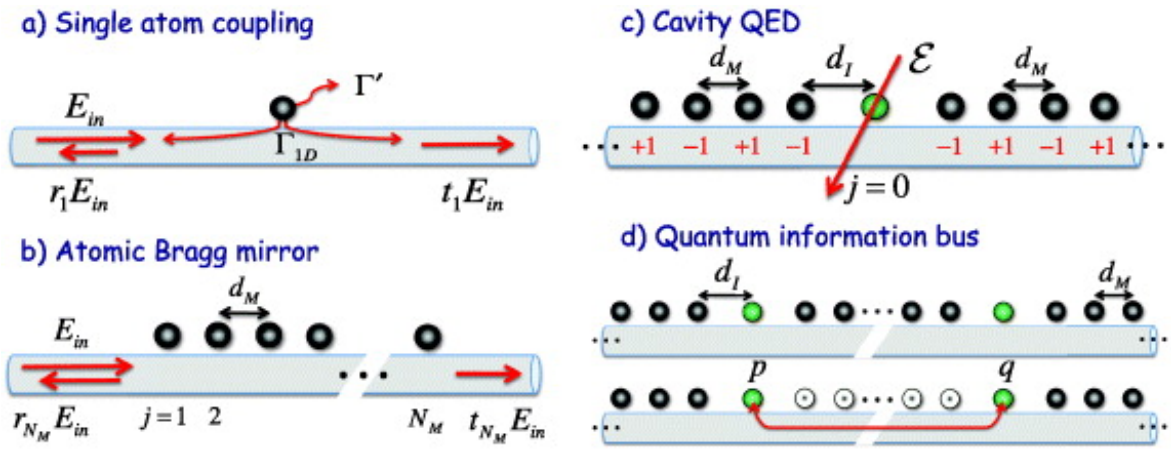

Figure 1.2: Different configurations of a coupled atom-fiber system with atoms trapped around a nanofiber. (a) Single atom scatters ONF-guided input with reflection (r_1) and transmission (t_1) amplitudes. (b) A chain of atoms form an atomic Bragg mirror. (c) Two atomic Bragg mirrors form a cavity which enhances the coupling of an impurity atom (shown in green). (d) Quantum information transfer can occur between two initially separated impurity atoms p, q in cavities separated by a chain of mirror atoms. The mirror atoms between the impurity atoms are flipped into a transparent hyperfine state, essentially loading p, q into a common cavity mode defined by the remaining mirror atoms positioned external to them. The figure is reproduced from [58].

single photons into a guided mode. This paves the way to herald, store, and read out a single collective atomic excitation in waveguide-QED platforms.

Superradiance and Subradiance Spontaneous emission for an ensemble of closely spaced identical atoms may be modified due to collective effects, leading to either enhancement (superradiance) or suppression (subradiance) of the spontaneous emission [70]. Superradiance occurs if all the atoms contribute constructively to the emission process through a constructive interference between the radiation from different atoms. This is strongest for a symmetric collective state. Subradiance occurs for an anti-symmetric collective state where the expectation value of the total dipole moment is minimized or even reduced to zero via destructive interference between the radiation from different atoms.

Owing to their suppressed radiation, the anti-symmetric states that constitute a sub-radiant system can store quantum information encoded in photons over long time scales. In contrast, a superradiant state is promising for a fast readout of the quantum information for high-speed quantum networks, owing to their radiation speed-up which is much faster than the single atom spontaneous emission.

Recently, Zhou et al. [71] investigated the dependence of the single photon superradiant emission rate on the interatomic distance in a 1D chain of atoms around a waveguide. Kornovan et al. [72] showed that long-lived subradiant states could be obtained in a similar periodic chain of two-level atoms with proper system paramters. Solano et al. [70] reported infinite-range atom-atom interactions between macroscopically separated (typically hundreds of resonant wavelengths) ^{87}Rb atoms in the vicinity

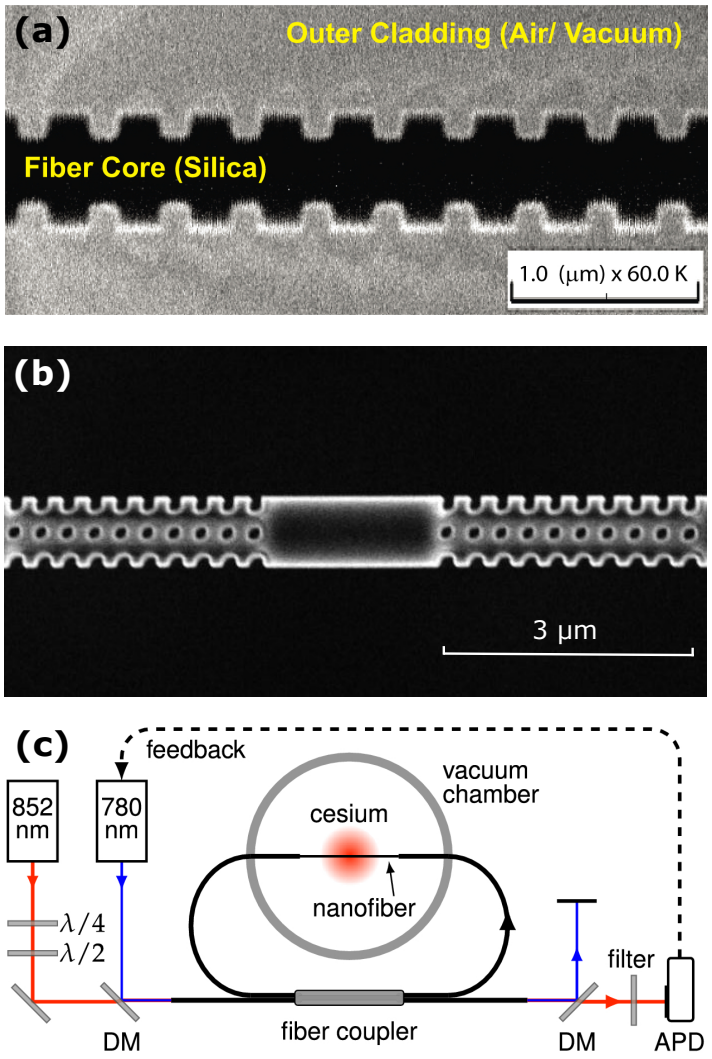

Figure 1.3: Nanofiber-integrated cavity structures. (a) Scanning ion microscope (SIM) image of a nanofiber Bragg grating fabricated via focused-ion beam (FIB) milling. Reproduced from [62]. (b) Scanning electron microscope (SEM) image of a cavity fabricated on an ONF. Reproduced from [65]. (c) Experimental schematic with a nanofiber-integrated cavity interfacing a cold Cs ensemble, reproduced from [67]. Collectively enhanced strong coupling of the Cs ensemble with a fiber cavity was demonstrated.

of an ONF, constituting a proof-of-principle demonstration of collective behavior of macroscopically delocalized atomic states. This opens up new proposals in quantum information and many-body physics.

Four-wave mixing Four-wave mixing (FWM) is a third-order nonlinear process in which the simultaneous interaction of atoms with two near-resonant laser fields leads to the generation of two additional coherent fields. In the field of quantum communication, a great deal of attention is being paid to developing quantum-correlated photon pairs from atomic ensembles [73, 74]. This is due, in part, to the proposal of an atomic ensemble-based quantum repeater, the DLCZ protocol [75]. Long distance

quantum communication relies on the distribution of entanglement over large distances and entangled photon pairs are currently the leading candidates to provide entanglement distribution. Quantum-correlated photon pairs have been an important resource enabling a range of quantum optical technologies, including the fundamental tests for quantum mechanics [76–79] and for the implementation of quantum-information protocols [6, 80, 81]. One of the most promising approaches to generate photon pairs is to use nonlinear optical effects in atomic media, such as parametric FWM processes. Another promising application of FWM is in the generation of squeezed light [82, 83], which is a fundamental building block for photonic quantum technologies [84] and an invaluable resource for quantum metrology applications [22, 85]. FWM processes are typically achieved at high OD (≈30-40) which requires us to increase the OD in our ONF-atom system.

1.3 Nanofiber-Based Dipole Traps for Cold Atoms

The optical dipole force, that will be discussed in Section 2.1.3, can be used to create conservative traps. For laser frequencies red-detuned with respect to the atomic transition, the ac-Stark effect (see Section 2.1.4) produces a negative shift to the ground state energy of the atom. The shift is proportional to the electric field intensity and, for a spatially varying intensity, the atom experiences a dipole force toward the intensity maximum region. In contrast, the ground state energy experiences a positive shift for a blue-detuned beam: the atom is pushed away from the intensity maximum region.

A simple way to construct an optical dipole trap is to focus a collimated red-detuned Gaussian beam. A focused Gaussian beam possesses an intensity profile that decreases both radially and axially away from the focal point. A 1D optical lattice can be constructed by overlapping two counter-propagating red-detuned beams with the same polarizations. The counter-propagating beams create a standing wave with a spatial intensity variation of the form $\cos^2(kz)$ along the axis of propagation z, with k being the wavenumber of the light. The intensity profiles for the two cases are illustrated in Figure 1.4.

The dipole force exerted by far-detuned light guided through a nanofiber is significant, even with relatively low optical power, due to the strong transverse field confinement. This is utilized in fiber-based evanescent field trapping to confine atoms in a lattice in the vicinity of a nanofiber [28]. The basic idea is to use a two-color dipole trap [27] as depicted in Figure 1.5(a). For a red-detuned beam propagating in the fundamental, HE_{11}, mode through the ONF, an atom (ground state) in the evanescent field experiences a dipole force toward the nanofiber surface since the evanescent field intensity decreases radially away from the surface (see Figure 3.10). However, this would result in atoms either getting deposited on the ONF surface or being heated up by the fiber and lost from the interaction region altogether. Stable trapping in the vicinity of the ONF can be achieved by an additional blue-detuned beam propagating in the HE_{11} mode, which pushes the atoms away from the surface. Since the evanescent field for the blue-detuned light (shorter wavelength) decays faster than that for the red-detuned light (longer wavelength), the attractive potential decays slower than the repulsive potential. The combintation of these two colors, with appropriate

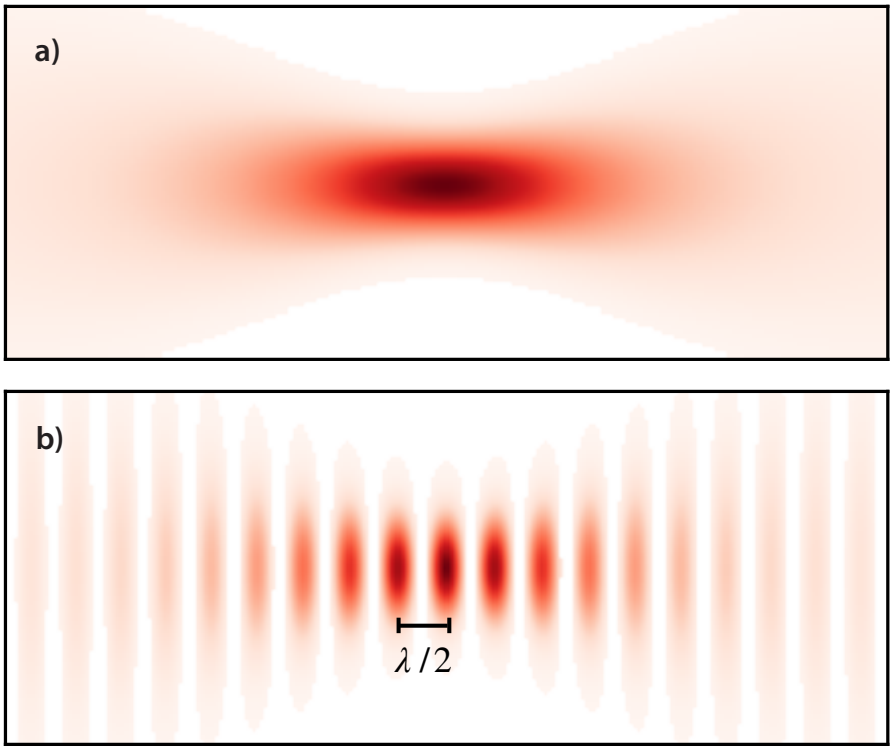

Figure 1.4: Illustration of (a) a dipole trap created by a single focused Gaussian beam and (b) a 1D optical lattice created by two counter-propagating focused Gaussian beams. For red-detuned beams, atoms experience a dipole force toward the intensity maxima. The counter-propagating beams create a standing-wave pattern with half-wavelength ($\lambda/2$) separation between the consecutive intensity maxima.

intensities, creates a trapping potential located a few hundred nanometers from the surface thereby confining atoms in the radial direction. The confinement along the fiber axis is obtained with a standing wave similar to the 1D lattices in free-space (see Figure 1.5(b)). The azimuthal confinement depends on the guided mode symmetry. For a quasi-circularly polarized mode, the trapping potential is rotationally invariant around the ONF, but for quasi-linearly polarized mode, the trapping potential depends on the overlap of the polarizations of the two light fields and, in general, is azimuthally asymmetric.

The trapping potential is a consequence of the intrinsic ac-Stark (light) shifts of the ground state energy level of atoms by optical trapping fields. However, this intrinsic shift is also an important issue as, together with the light shifts of the excited states, the optical transition energies are shifted. This is an important parameter for coherent state control of the atoms. Additionally, there are differential shifts within the hyperfine manifold of states owing to the vector and the tensor parts of the polarizability (see Section 2.2.2). The differential shifts within the excited state hyperfine manifold are typically several orders of magnitude larger than those of the ground state. For a typical far off-resonant trap with ∼1 mK depth, the state-dependent excited state differential light shifts can easily exceed tens of MHz [86], which is larger than the typical excited

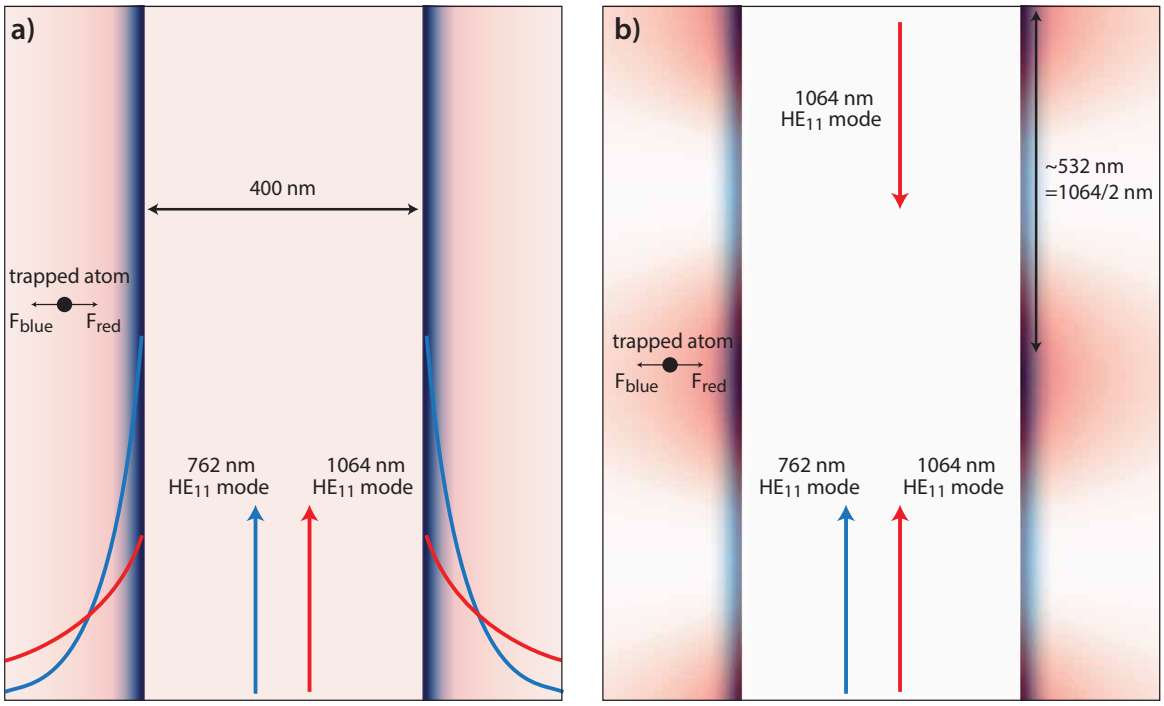

Figure 1.5: Schematic of the two-color fiber trap configuration. (a) The intensity profile for 762 nm (blue-detuned) and 1064 nm (red-detuned) light propagating through an ONF of 400 nm diameter. The blue field decays faster than the red field such that with a suitable balance of power an atom is trapped at a certain distance from the nanofiber surface. (b) Evenly spaced intensity maxima for the red field are created with counter-propagating 1064 nm light.

state transition linewidth. The ground state differential shift is of the order of 100 kHz.

For many applications, trapping alkali atoms without affecting the energies between the relevant atomic levels is desirable, as a deep trap potential can be achieved without broadening the relevant transition beyond usefulness. For example, in frequency metrology, atomic clock, and quantum computing applications, the differential light shifts of the hyperfine transition are a major source of decoherence. For certain transitions, this can be achieved by tuning the two-color trapping lasers - the red- and blue-detuned lasers - to magic wavelengths [87, 88] that shift the ground and the excited states by the same amount so that the optical transition itself is not shifted. Cancellation of differential light shifts, in free-space, can be achieved for circularly [89] and elliptically polarized [90] optical traps and, in some cases, with additional quadratic Zeeman shifts [91, 92].

In an ONF, the presence of the longitudinal component of the electric field of the guided modes with a $\pi/2$ phase relative to the transverse component causes the field to have a non-zero ellipticity, leading to a large vector and tensor polarizabilities. A state-insensitive compensated two-color fiber-based dipole trap can be achieved by using two pairs of guided counter-propagating beams, one attractive red- and another repulsive blue-detuned, operating at the magic wavelengths [93, 94]. In this state-insensitive compensated trap, the differential vector and tensor shifts are strongly suppressed.

Such a compensated ONF-based dipole trap has been demonstrated for laser-cooled Cs atoms [30, 68] with around 2000 atoms trapped.

For Rb atoms, the situation is somewhat more complicated than for Cs; there are magic wavelengths [88–90, 95], but these are either too close to resonant transitions, causing heating, or are not convenient to use in nanofiber-based traps, due to absorption by the silica fiber. There has been only one report of a (non state-compensated) ONF-based dipole trap for Rb atoms [96]. The authors estimated that 302 ^{87}Rb atoms were trapped, with a lower bound of 123 atoms. This number is relatively low compared to that reported for Cs. One of our goals was to improve this number.

1.4 Thesis Outline

Chapter 2: We start with a discussion of the basics of light-matter interactions and atomic physics concepts relevant to the works presented in the following chapters.
Chapter 3: This chapter presents the description of the ONF-MOT hybrid setup we used for all the experiments with laser-cooled ^{87}Rb atoms interfacing to the ONF. The properties of the installed ONF and the method of polarization control for a single-mode ONF adapted from [97] are detailed. The polarization control is a crucial element for the $S \rightarrow S$ single-frequency two-photon transition (Chapter 5) and the fiber-trap (Chapter 6) experiments.
Chapter 4: Here we report on our experimental demonstration of an electric quadrupole transition driven by nanofiber-guided pump light. We probed a quadrupole transition in laser-cooled ^{87}Rb atoms using only a few μW of laser power propagating through the ONF; exploiting the large electric field gradient in the evanescent field of the ONF guided mode. This established the ONF as an easily accessible platform to drive quadrupole transitions, which are usually harder to access in free-space because of the requirement of a large field gradient.
Chapter 5: Here, we discuss single-frequency two-photon excitation in ^{87}Rb, both in a warm vapor cell with a paraxial pump beam and in a cold MOT ensemble with a nonparaxial pump beam guided through the ONF. We first detail the theoretical framework for polarization dependence in an $S \rightarrow S$ transition. The results of the experiments on the excitation efficiency of the $5S_{1/2} \rightarrow 6S_{1/2}$ two-photon transition in ^{87}Rb on the polarization of the pump beams are presented.
Chapter 6: Here we report on our implementation of a two-color evanescent field fiber trap [27, 28, 96], where a pair of counter-propagating red-detuned light fields and a single traveling blue-detuned light field were used to create a 1D array of trapping potentials along the ONF. The effects of the inherent ellipticity in polarization of the fiber modes on the trapping is outlined, explaining the limiting condition on permissible trap depth for ^{87}Rb atoms. We discuss machine learning based optimzation of the loading of the laser-cooled ^{87}Rb atoms into the trap array to optimize the final number of trapped atoms and the OD of the system.
Chapter 7: In this chapter, we discuss a degenerate four-wave mixing (FWM) process in a hot rubidium vapor cell. While this is an incomplete work, we discuss our motivation, the limitations and the improvements that can be made.

Finally, we conclude the thesis summarizing the work so far and presenting some

outlook on future experiments that can be performed.

Chapter 2

Light-Matter Interactions

In this chapter, we will give a brief theoretical description of the interaction of atoms with electromagnetic (EM) fields. We will consider the treatment of a two-level atom coupled to a classical light field (specifically, an intense monochromatic laser field) within the semi-classical picture. We will restrict our discussion to hydrogen-like atoms with one valence electron in their outer shell. This is followed by a generalization to multilevel atoms. Finally, we will introduce how the cooling and trapping of atoms can be achieved using appropriate spatially structured laser light fields.

2.1 Two-Level Atoms

Let us start by assuming we have a single atom with an excited and a ground state, labelled $|e\rangle$ and $|g\rangle$, respectively. The two states are coupled by an electric dipole transition frequency, ω_{eg}. It is convenient to define some atomic operators in the basis $\{|e\rangle, |g\rangle\}$. We define the operators as

$$\hat{\sigma}_+ = \hat{\sigma}_x + i\hat{\sigma}_y = |e\rangle\langle g| \tag{2.1}$$

$$\hat{\sigma}_- = \hat{\sigma}_x - i\hat{\sigma}_y = |g\rangle\langle e| \tag{2.2}$$

$$\hat{\sigma}_z = |e\rangle\langle e| - |g\rangle\langle g|. \tag{2.3}$$

The $\hat{\sigma}_x$, $\hat{\sigma}_y$ and $\hat{\sigma}_z$ are the Pauli spin matrices that represent the intrinsic angular momentum components of electronic spin. The operators $\hat{\sigma}_\pm$ are the atomic transition operators and account for the atomic coherence.

We will consider a monochromatic classical field, $\mathbf{E}(t)$, with amplitude, $\mathcal{E}$, polarization vector, $\boldsymbol{\epsilon}$, and angular frequency, ω, which is detuned, Δ, from the atomic transition frequency, ω_{eg}, such that

$$\begin{aligned}\mathbf{E}(t) = \boldsymbol{\epsilon}\mathcal{E}\cos(\omega t) &= \frac{\boldsymbol{\epsilon}\mathcal{E}}{2}\left(e^{-i\omega t} + e^{i\omega t}\right) \\ &= \mathbf{E}^+(t) + \mathbf{E}^-(t).\end{aligned} \tag{2.4}$$

The total Hamiltonian, $\mathcal{H}$, of the system can be written as the sum of the free atom

Hamiltonian, $\mathcal{H}_\mathcal{A}$, and the atom-field interaction Hamiltonian, $\mathcal{H}_\mathcal{I}$, as

$$\mathcal{H} = \mathcal{H}_\mathcal{A} + \mathcal{H}_\mathcal{I}. \tag{2.5}$$

Defining the zero-point energy as the midway between the ground and the excited state energy, $\mathcal{H}_\mathcal{A}$ takes the form

$$\mathcal{H}_\mathcal{A} = \frac{1}{2}\hbar\omega_{eg}|e\rangle\langle e| - \frac{1}{2}\hbar\omega_{eg}|g\rangle\langle g| = \frac{1}{2}\hbar\omega_{eg}\hat{\sigma}_z. \tag{2.6}$$

Considering the interaction between the atom and the field to be the electric dipole interaction, the atom-field interaction Hamiltonian in the dipole approximation is

$$\mathcal{H}_\mathcal{I} = -\mathbf{d}\cdot\mathbf{E}. \tag{2.7}$$

Here, $\mathbf{d}$ is the electric dipole operator, which can be expanded into its constituent transition dipole matrix elements as

$$\mathbf{d} = \langle g|\mathbf{d}|e\rangle\,(\hat{\sigma}_+ + \hat{\sigma}_-) = \mathbf{d_{ge}}\,(\hat{\sigma}_+ + \hat{\sigma}_-) \tag{2.8}$$

$$= \mathbf{d}^+ + \mathbf{d}^-, \tag{2.9}$$

where we have introduced the notation $\mathbf{d_{ge}} = \langle g|\mathbf{d}|e\rangle$. Only the off-diagonal matrix elements are nonzero due to parity symmetry ($\langle g|\mathbf{d}|g\rangle = \langle e|\mathbf{d}|e\rangle = 0$). The dipole term oscillates at the atomic resonance frequency, $\mathbf{d}^\pm \sim e^{\mp i\omega_{eg}t}$. Then, the interaction Hamiltonian, $\mathcal{H}_\mathcal{I}$, contains terms oscillating at $\omega + \omega_{eg}$ and terms oscillating at $\omega - \omega_{eg}(= \Delta)$. When $|\Delta| \ll \omega + \omega_{eg}$, the rotating wave approximation (RWA) is made by neglecting the fast oscillation terms. The interaction Hamiltonian is approximated as

$$\mathcal{H}_\mathcal{I} \approx -\mathbf{d}^+\cdot\mathbf{E}^- - \mathbf{d}^-\cdot\mathbf{E}^+. \tag{2.10}$$

The RWA focuses on slow dynamics, replacing the terms rotating at optical frequencies by their zero average value. The Hamiltonian can be written in terms of the Rabi frequency, Ω,

$$\mathcal{H}_\mathcal{I} = \frac{\hbar\Omega}{2}(\hat{\sigma}_+ e^{-i\Delta t} + \hat{\sigma}_- e^{i\Delta t}), \tag{2.11}$$

where $\Omega = -\mathbf{d_{ge}}\cdot\boldsymbol{\epsilon}\mathcal{E}/\hbar$. The Rabi frequency describes the strength of coupling between the atom and the field.

2.1.1 Optical Bloch equations

The Schrödinger equation suffices to describe the dynamics of the atom-light system in the absence of any decoherence. However, such a description does not account for any dissipative or relaxation processes. A real atomic system exhibits finite lifetimes of the excited states, with the excited states decaying back to the ground state via spontaneous emission. Considering the interaction Hamiltonian we have constructed in Equation 2.11, the evolution of the system can be described in the density matrix

formalism by the Schrödinger-von Neumann [98] equation in the rotating frame

$$i\hbar\partial_t\rho = [\mathcal{H}, \rho], \tag{2.12}$$

where $\rho = |\psi\rangle\langle\psi|$ is the density operator. We can determine the following equations for the density matrix elements

$$\begin{aligned}
\partial_t\rho_{ee} &= i\frac{\Omega}{2}(\tilde{\rho}_{eg} - \tilde{\rho}_{ge}),\\
\partial_t\rho_{gg} &= -i\frac{\Omega}{2}(\tilde{\rho}_{eg} - \tilde{\rho}_{ge}),\\
\partial_t\tilde{\rho}_{ge} &= -i\Delta\tilde{\rho}_{ge} - i\frac{\Omega}{2}(\rho_{ee} - \rho_{gg}),\\
\partial_t\tilde{\rho}_{eg} &= -i\Delta\tilde{\rho}_{eg} + i\frac{\Omega}{2}(\rho_{ee} - \rho_{gg}).
\end{aligned} \tag{2.13}$$

Equations 2.13 describe the evolution of populations (ρ_{ee} and ρ_{gg}) and coherences (ρ_{ge} and ρ_{eg}) in the two-level atom system. Here, the tilde is used to denote the density matrix elements in the rotating frame ($\tilde{\rho}_{eg} = \rho_{eg}\exp(-i\Delta t)$ and $\tilde{\rho}_{ge} = \tilde{\rho}^*_{ge}$). We arrive at the optical Bloch equations (OBE) by adding the phenomenological damping terms to the evolution terms:

$$\begin{aligned}
\partial_t\rho_{ee} &= i\frac{\Omega}{2}(\tilde{\rho}_{eg} - \tilde{\rho}_{ge}) - \Gamma\rho_{ee}\\
\partial_t\rho_{gg} &= -i\frac{\Omega}{2}(\tilde{\rho}_{eg} - \tilde{\rho}_{ge}) + \Gamma\rho_{ee}\\
\partial_t\tilde{\rho}_{ge} &= -(\gamma + i\Delta)\tilde{\rho}_{ge} - i\frac{\Omega}{2}(\rho_{ee} - \rho_{gg})\\
\partial_t\tilde{\rho}_{eg} &= -(\gamma - i\Delta)\tilde{\rho}_{eg} + i\frac{\Omega}{2}(\rho_{ee} - \rho_{gg}),
\end{aligned} \tag{2.14}$$

where Γ is the spontaneous decay rate and γ corresponds to the coherence decay rate, which models dephasing effects such as atom-atom collisions that do not affect the populations.

2.1.2 Useful results and definitions

Here, we summarize several useful results and definitions obtained from the solutions to the OBE, Equations 2.14, that will be referred to throughout this work.

Steady state solution The dissipation introduced by the spontaneous emission allows the system to reach a steady state. In the asymptotic limit, the populations ρ_{gg} and ρ_{ee} in Equations 2.14 are constant. Hence, letting the time derivatives be zero, and by further assuming purely radiative damping ($\gamma = \Gamma/2$), the excited state population settles to the steady state

$$\rho_{ee}(t \to \infty) = \frac{(\Omega/\Gamma)^2}{1 + 2(\Omega/\Gamma)^2 + 4(\Delta/\Gamma)^2}. \tag{2.15}$$

Saturation The maximum population of the excited state is $\rho_{ee} = 1/2$, which is achieved only asymptotically as the laser intensity (I) is increased (since $\Omega^2 \propto I$). This effect is known as *saturation*. We can define a saturation parameter, s, given by

$$s = \frac{\Omega^2/\gamma\Gamma}{1 + \Delta^2/\gamma^2}. \tag{2.16}$$

Scattering cross-section The total scattering rate is given by $\Gamma\rho_{ee}$. The scattering cross-section, σ, defined as the power radiated by the atom divided by the incident energy flux, is then given by

$$\sigma = \frac{\sigma_0}{1 + 2(\Omega/\Gamma)^2 + 4(\Delta/\Gamma)^2}, \tag{2.17}$$

where the on-resonance cross-section is defined by

$$\sigma_0 = \frac{\hbar\omega_{eg}\Gamma}{2I_{\text{sat}}}. \tag{2.18}$$

In writing Equation 2.18, we defined the *saturation intensity*, I_{sat}, such that

$$s \equiv \frac{I}{I_{\text{sat}}} = 2\left(\frac{\Omega}{\Gamma}\right)^2. \tag{2.19}$$

Power broadening The scattering rate has a Lorentzian lineshape, with a full-width-half-maximum (FWHM), $\Gamma' = \Gamma\sqrt{1+s}$. At low intensity ($s \ll 1$), the width is equal to the natural linewidth, Γ. The width increases with intensity, leading to power broadening of the absorption line.

2.1.3 The polarizability of a two-level atom

The steady-state solution of the OBE yields an induced dipole moment of the atom described by the expectation value of the dipole operator. Thus, the induced dipole moment is given as

$$\begin{aligned} \mathbf{d} = \langle \mathbf{d} \rangle &= \text{Tr}(\rho \mathbf{d}) \\ &= d_{ge}(\tilde{\rho}_{eg} e^{i\Delta t} + \tilde{\rho}_{ge} e^{-i\Delta t}), \end{aligned} \tag{2.20}$$

where $\text{Tr}(\hat{O}) = \sum_n \langle n|\hat{O}|n\rangle$ denotes the trace of a matrix. The polarizabilty, $\alpha(\omega)$, is then given as the ratio of the induced dipole moment of an atom to the electric field that produces it, such that

$$\mathbf{d} = \alpha(\omega)\mathbf{E}. \tag{2.21}$$

The steady state polarizability (plotted in Figure 2.1) can then be found by substituting the steady state value of $\tilde{\rho}_{ge}$ from the OBE (Equations 2.14) into Equation 2.20 and

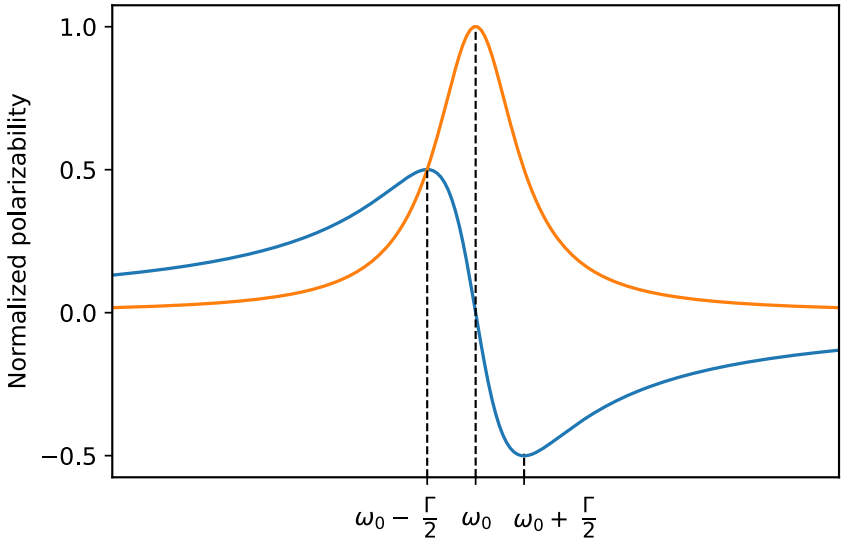

Figure 2.1: Real (blue) and imaginary (orange) parts of the polarizability, $\alpha(\omega)$, as a function of angular frequency, ω, of the driving field.

then comparing it with Equation 2.21:

$$\mathrm{Re}\left[\alpha(\omega)\right] = -\frac{d_{ge}^2}{\hbar}\frac{4\Delta/\Gamma^2}{1+4(\Delta/\Gamma)^2+2(\Omega/\Gamma)^2}, \tag{2.22}$$

$$\mathrm{Im}\left[\alpha(\omega)\right] = \frac{d_{ge}^2}{\hbar}\frac{2/\Gamma}{1+4(\Delta/\Gamma)^2+2(\Omega/\Gamma)^2}. \tag{2.23}$$

Scattering rate and the scattering force The time-averaged power absorbed by the atom from the driving field and subsequently re-emitted as dipole radiation is described by

$$\mathrm{P} = \langle \dot{\mathbf{d}} \cdot \mathbf{E} \rangle = \frac{\omega I}{\epsilon_0 c}\,\mathrm{Im}\left[\alpha(\omega)\right]. \tag{2.24}$$

The absorption and subsequent scattering results obtained from the imaginary part of the polarizability (Equation 2.23) is related to the out-of-phase component of the dipole moment. The energy dissipation is quantized and photons are emitted when atoms transition back to the ground state $|g\rangle$ from the excited state $|e\rangle$ with a scattering rate

$$\Gamma_{\mathrm{sc}} = \frac{P}{\hbar\omega} = \frac{\Gamma}{2}\frac{s_0}{1+s_0+4(\Delta/\Gamma)^2}. \tag{2.25}$$

Comparing this with Eq. 2.15, we notice that $\Gamma_{\mathrm{sc}} = \Gamma\rho_{ee}$. This follows naturally since the total scattering rate is obtained from the spontaneous decay of the excited state population. The force associated with this scattering is given as

$$\mathbf{F}_{\mathrm{sc}} = (\hbar\mathbf{k}) \times \Gamma_{\mathrm{sc}}, \tag{2.26}$$

where $\hbar\mathbf{k}$ is the momentum of incoming photons and $\mathbf{k}$ is the associated wavevector. The scattering is a dissipative process, which allows for cooling atoms down to μK temperatures.

Saturated absorption and optical depth An important effect to consider while working with an ensemble of atoms is saturated absorption. The intensity of light, $I(z)$, propagating through a vapor cell filled with atoms at a density n will be attenuated due to scattering by atoms as it propagates a distance dz through the cell, $I(z) = I_0 e^{-\kappa z}$. The attenuation then relates to the imaginary component of the polarizability as

$$\kappa = nk\frac{\mathrm{Im}\,\alpha(\omega)}{\epsilon_0}. \tag{2.27}$$

This gives us the relation,

$$\frac{dI}{dz} = -nkI\frac{\mathrm{Im}\,\alpha(\omega)}{\epsilon_0} = -n\hbar\omega\frac{\Gamma}{2}\frac{I/I_{\mathrm{sat}}}{1 + I/I_{\mathrm{sat}} + 4(\Delta/\Gamma)^2}. \tag{2.28}$$

In the high intensity limit $I \gg I_{\mathrm{sat}}$ we have,

$$\frac{dI}{dz} = -n\hbar\omega\frac{\Gamma}{2}. \tag{2.29}$$

It is worth noticing that, in this limit, the attenuation of intensity is independent of the intensity and decreases linearly only with the distance propagated through the medium, i.e., the absorption saturates at high intensity. This principle underlies the basis of saturated absorption spectroscopy (SAS) [99] often used to lock the operating frequency of lasers.

In the weak intensity limit $I \ll I_{sat}$, a useful quantity that describe the strength of interaction of light with an ensemble of atoms is optical depth. Optical depth (OD) is defined as the quantity, od, such that an incident resonant field is attenuated by a factor e^{-od} while transmitted through the medium. The optical depth may then be determined by sending an on-resonant field with intensity I_0 through the ensemble and measuring the transmitted intensity I_T.

$$od = \ln\frac{I_0}{I_T} \tag{2.30}$$

Such a measurement may however be challenging for ensembles with very high optical depth as such an ensemble will attenuate the incident light beyond measuring capacity. Thus it is practical to define the optical depth in terms of transmitted off-resonant light. It follows from Equation 2.28 that

$$od = (1 + 4(\Delta/\Gamma)^2) \cdot \ln\frac{I_0}{I_T(\Delta \neq 0)}. \tag{2.31}$$

Dipole potential and the dipole force The time averaged interaction of the

induced dipole moment in the driving field (linearly polarized) is given by

$$U_{\text{dip}} = -\frac{1}{2}\langle \mathbf{d} \cdot \mathbf{E} \rangle = -\frac{I}{2\epsilon_0 c} \text{Re}\left[\alpha(\omega)\right]. \tag{2.32}$$

The factor 1/2 accounts for the fact that the dipole is induced and not permanent. Atoms subjected to a spatially varying light field will experience a spatially varying induced dipole potential and a resulting dipole force from the gradient of the interaction potential, which is given by

$$\mathbf{F}_{\text{dip}}(\mathbf{r}, \omega) = \nabla U_{\text{dip}}(\mathbf{r}) = \frac{1}{2\epsilon_0 c} \text{Re}\left[\alpha(\omega)\right] \nabla I(\mathbf{r}). \tag{2.33}$$

2.1.4 AC-Stark shift or the light shift

An alternative picture to understand the dipole potential described in the previous section is in terms of the light shift of the ground state energy of an atom due to the interaction Hamiltonian. The ac-Stark shift or the light shift corresponds to the shift in energy levels of the bare atoms due to interaction with an EM field. Going back to the total Hamiltonian for a two-level atom interacting with a monochromatic classical field (Equations 2.6 and 2.11),

$$\mathcal{H} = \frac{1}{2}\hbar\omega_{eg}\hat{\sigma}_z + \frac{\hbar\Omega}{2}(\hat{\sigma}_+ e^{-i\Delta t} + \hat{\sigma}_- e^{i\Delta t}). \tag{2.34}$$

We can diagonalize this Hamiltonian to find the eigensolutions which are given as

$$E_\pm = \frac{1}{2}\hbar\omega_{eg} \pm \frac{1}{2}\hbar\sqrt{\Omega^2 + \Delta^2}. \tag{2.35}$$

$E^+(E^-)$ is the excited (ground) state energy eigenvalue of the atom in the presence of the field. The excited state is thus shifted up by $\hbar\Omega_{\text{eff}}/2$ while the ground state is shifted down by $\hbar\Omega_{\text{eff}}/2$, where we have used the notation $\Omega_{\text{eff}} = \sqrt{\Omega^2 + \Delta^2}$ for effective Rabi frequency. Figure 2.2 shows the light shifts in a two-level atom in a presence of a detuned light field. The gradient of the energy describes the dipole force on the atom and thus an atom in the ground state and in a red-detuned field can be trapped in the region of high intensity of the light field.

In general, a real atom has a complex electronic substructure with each sublevel having slightly different interactions with the field and associated different shifts. This may lead to some interesting effects, including the inhomogenous broadening of the absorption (see Chapter 6).

2.2 Multilevel Atoms

Each sublevel in the electronic substructure of the atom couples to the radiation field slightly differently depending on the orientation of its dipole moment and the polarization of the light. Rewriting the standard interaction Hamiltonian Equation 2.7 in a

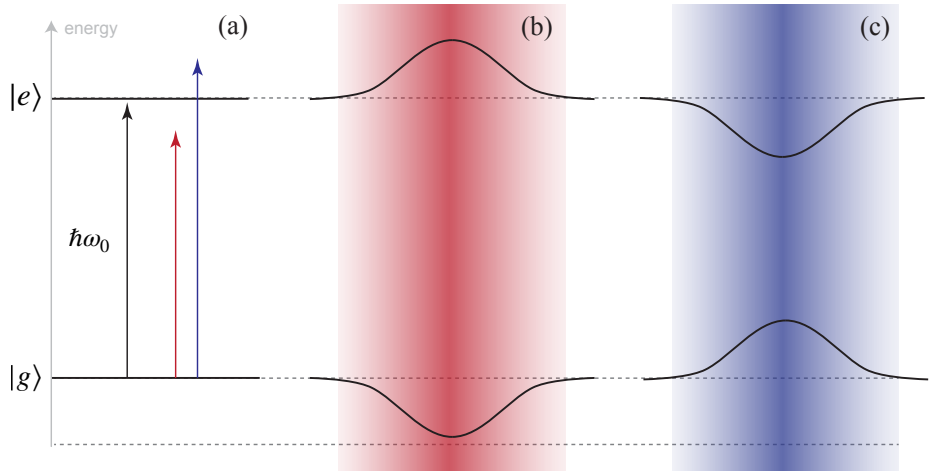

Figure 2.2: AC-stark shift of a two-level atom in a focused red- and blue-detuned light field, detuned with respect to the atomic transition energy. (a) Unperturbed energy levels of the ground $|g\rangle$ and excited $|e\rangle$ state. The red and blue arrows indicate the energy of the red- and blue-detuned light respectively. (b) Shifted energies of $|g\rangle$ and $|e\rangle$ in the red-detuned light field. The shift is proportional to the intensity with higher intensity represented by darker region. (c) The sign of the shift is inverted for the blue-detuned light field.

slightly different way gives

$$\mathcal{H}_{\mathcal{I}} = -e\mathbf{r}\cdot\boldsymbol{\epsilon}\mathcal{E}, \tag{2.36}$$

where $\mathbf{r}$ is the position of the electron, $\boldsymbol{\epsilon}$ is the polarization of the light, e is the electronic charge and $\mathcal{E}$ is the amplitude of the electric field. Expressed in terms of atomic operators $\sigma_{ij} = |i\rangle\langle j|$ between any two atomic energy levels, we can write

$$e\mathbf{r}\cdot\boldsymbol{\epsilon} = \sum_{i,j} e|i\rangle\langle j|\mathbf{r}\cdot\boldsymbol{\epsilon}|i\rangle\langle j| = \sum_{i,j} d_{ij}\sigma_{ij} \tag{2.37}$$

with $d_{ij} = e\langle i|\mathbf{r}\cdot\boldsymbol{\epsilon}|j\rangle$ denoting the electric-dipole transition element. The calculation of this transition element depends on the wavefunctions of the involved energy levels and in general is not an easy task. The calculation, however, is simplified in spherical coordinates. The factor $\mathbf{r}\cdot\boldsymbol{\epsilon}$ can be written in terms of spherical unit vectors u_q as

$$\mathbf{r}\cdot\boldsymbol{\epsilon} = \mathbf{r}\cdot u_q = \sqrt{\frac{4\pi}{3}}\cdot r\cdot Y_1^q(\theta,\phi) \tag{2.38}$$

with

$$u_+ = \frac{1}{\sqrt{2}}(e_x + ie_y), \quad u_- = \frac{1}{\sqrt{2}}(e_x - ie_y), \quad u_0 = e_z, \tag{2.39}$$

where

$$Y_l^m(\theta,\phi) = \sqrt{\frac{(2l+1)}{4\pi}\cdot\frac{(l+m)!}{(l-m)!}}\cdot P_l(\cos\theta)e^{im\phi}. \tag{2.40}$$

$Y_l^m(\theta,\phi)$ is the spherical harmonics function, $P_l(\cos\theta)$ is the Legendre polynomial and $q = 0, \pm 1$ specifies the polarization of the light field.

In a simple case without fine and hyperfine interactions and n, l, m are the principal, orbital and magnetic quantum numbers, respectively, the electric-dipole transition element may be written as

$$e\langle i|\mathbf{r}\cdot\boldsymbol{\epsilon}|j\rangle = e\langle n'l'm'|\mathbf{r}\cdot\boldsymbol{\epsilon}|nlm\rangle = e\langle n'l'||\mathbf{r}||nl\rangle\langle l'm'|\sqrt{\frac{4\pi}{3}}\cdot Y_1^q|lm\rangle. \tag{2.41}$$

The term $\langle n'l'||\mathbf{r}||nl\rangle$ is the reduced matrix element and depends only on the orbital wavefunction. This is a special notation used in conjunction with the Wigner-Eckart theorem [100, 101]. The angular contribution of the matrix elements relates to the Clebsch-Gordon (CG) coefficients, involving the integrals of the products of spherical harmonics, that can be conveniently evaluated in terms of Wigner 3j-symbol [102]

$$\langle l'm'|\sqrt{\frac{4\pi}{3}}\cdot Y_1^q|lm\rangle = (-1)^{(l'-m')}\sqrt{\max(l,l')}\begin{pmatrix} l' & 1 & l \\ -m' & q & m \end{pmatrix}. \tag{2.42}$$

2.2.1 Fine and hyperfine interactions

Spin-orbit interaction that couples the electronic spin with its orbital angular momentum leads to the splitting principal energy levels called fine structures. This leads naturally to the introduction of total angular momentum $J = L + S$. Fine energy levels are further split into hyperfine levels due to the coupling of nuclear spin I with the total angular momentum J. Similar to J, this introduces the quantum number $F = J + I$.

Analogous to Equation 2.41, the two hyperfine levels $|F, m_F\rangle$ and $|F', m'_F\rangle$ couples via the dipole interaction, resulting in a reduced matrix element which is independent of magnetic sublevels and coupling coefficient that only depends on the magnetic quantum number.

$$e\langle F\ m_F|\mathbf{r}\cdot\boldsymbol{\epsilon}|F'\ m'_F\rangle = e\langle F||\mathbf{r}||F'\rangle\cdot(-1)^{F'-1+m_F}\sqrt{2F+1}\cdot\begin{pmatrix} F' & 1 & F \\ m'_F & q & -m_F \end{pmatrix}. \tag{2.43}$$

The full calculation involves the expansion of F states in the $L-S$ basis and recoupling of all CG coefficients [100, 101]. Further simplification of the reduced matrix element is done by factoring out the F, F' dependence

$$e\langle F||\mathbf{r}||F'\rangle = e\langle J||\mathbf{r}||J'\rangle\cdot(-1)^{F'+J+1+I}\sqrt{(2F'+1)(2J+1)}\cdot\begin{Bmatrix} J & J' & 1 \\ F' & F & I \end{Bmatrix}. \tag{2.44}$$

The term in the curly braces is the Wigner 6j-symbol. They are the generalization of the CG coefficients and Wigner 3j-symbols that appear in the coupling of three angular momenta [100, 101]. The J, J' dependence can further be factored out by expanding the J basis in to the $L-S$ basis resulting only in L dependent reduced matrix element,

$$e\langle J||\mathbf{r}||J'\rangle = e\langle L||\mathbf{r}||L'\rangle \cdot (-1)^{J'+L+1+S}\sqrt{(2J'+1)(2L+1)} \cdot \begin{Bmatrix} L & L' & 1 \\ J' & J & S \end{Bmatrix}. \quad (2.45)$$

The numerical values of the reduced matrix element can be calculated from the radiative lifetime measurements of the involved states or the Einstein A coefficients [103].

$$\frac{1}{\tau} = A_{ij} = \frac{\omega_{ij}^3}{3\pi\epsilon_0\hbar c^3} \cdot \frac{2J+1}{2J'+1} \cdot |\langle J||\mathbf{r}||J'\rangle|^2. \quad (2.46)$$

Following these, the dipole matrix element, d_{ij}, can be factorized into a reduced matrix element $||d||$ and a real transition coefficients c_{ij} [100, 101]

$$d_{ij} = c_{ij}||d||. \quad (2.47)$$

The coefficients, c_{ij}, take into account the coupling strength between the specific sub-levels, and the electronic and nuclear angular momenta involved.

2.2.2 Light shift and the polarizability for multilevel atoms

As a general result, the effect of a weak variable far-detuned EM field on the atomic levels can be treated as a perturbation in second order of the electric field [98]. The energy shift of the i-th unperturbed state for non-degenerate states is given by [104]

$$\Delta E_i = -\frac{\mathcal{E}^2}{4\hbar}\sum_{j\neq i} \mathrm{Re}\left(\frac{|e\langle j|\mathbf{r}\cdot\boldsymbol{\epsilon}|i\rangle|^2}{\omega_{ji} - \omega - \imath\gamma_{ji}/2} + \frac{|e\langle i|\mathbf{r}\cdot\boldsymbol{\epsilon}|j\rangle|^2}{\omega_{ji} + \omega + \imath\gamma_{ji}/2}\right). \quad (2.48)$$

The ac-Stark shift Equation 2.48 can be conveniently recasted in terms of polarizability through the Equation 2.21 as

$$\Delta E_i = -\frac{1}{2}\alpha_i(\omega)\mathcal{E}^2, \quad (2.49)$$

where $\alpha_i(\omega)$ is the total dynamic polarizability for the state $|i\rangle \equiv |F, m_F\rangle$, which can be further decomposed into m_F-independent scalar $\alpha_F^{(0)}$, vector $\alpha_F^{(1)}$ and tensor $\alpha_F^{(2)}$ components such that [90]

$$\alpha_i(\omega) = \alpha_F^{(0)}(\omega) + \beta_{\boldsymbol{\epsilon}}\frac{m_F}{2F}\alpha_F^{(1)}(\omega) + \gamma_{\boldsymbol{\epsilon}}\frac{3m_F^2 - F(F+1)}{F(2F-1)}\alpha_F^{(2)}(\omega). \quad (2.50)$$

The $\beta_{\boldsymbol{\epsilon}}$ and $\gamma_{\boldsymbol{\epsilon}}$ depend on the polarization vector of the light field given as

$$\beta_{\boldsymbol{\epsilon}} = \imath(\boldsymbol{\epsilon}\times\boldsymbol{\epsilon}^*)\cdot\mathbf{e_q} \quad \text{and} \quad \gamma_{\boldsymbol{\epsilon}} = \frac{1}{2}\left[3(\boldsymbol{\epsilon}^*\cdot\mathbf{e_q})(\boldsymbol{\epsilon}\cdot\mathbf{e_q}) - 1\right] \quad (2.51)$$

with $\mathbf{e_q}$ being the quantization axis unit vector. The expressions for the three components of the polarizabilities are given as follows [89, 104]:

$$\alpha_F^{(0)}(\omega) = \frac{1}{3(2J+1)} \sum_{J' \neq J} |e\langle J'||\mathbf{r}||J\rangle|^2 \times \frac{1}{\hbar} Re\left(\frac{1}{\omega_{J'J} - \omega - \imath\gamma_{JJ'}/2} + \frac{1}{\omega_{J'J} + \omega + \imath\gamma_{J'J}/2}\right), \quad (2.52)$$

$$\alpha_F^{(1)}(\omega) = (-1)^{F+I} \sqrt{\frac{6F(2F+1)}{F+1}} \begin{Bmatrix} F & 1 & F \\ J & I & J \end{Bmatrix} \sum_{J' \neq J} (-1)^{J'} \begin{Bmatrix} 1 & 1 & 1 \\ J & J' & J \end{Bmatrix} \times |e\langle J'||\mathbf{r}||J\rangle|^2 \frac{1}{\hbar} Re\left(\frac{1}{\omega_{J'J} - \omega - \imath\gamma_{JJ'}/2} + \frac{1}{\omega_{J'J} + \omega + \imath\gamma_{J'J}/2}\right), \quad (2.53)$$

$$\alpha_F^{(2)}(\omega) = (-1)^{F+I} \sqrt{\frac{10F(2F-1)(2F+1)}{3(F+1)(2F+3)}} \begin{Bmatrix} F & 2 & F \\ J & I & J \end{Bmatrix} \sum_{J' \neq J} (-1)^{J'} \begin{Bmatrix} 1 & 2 & 1 \\ J & J' & J \end{Bmatrix} \times |e\langle J'||\mathbf{r}||J\rangle|^2 \frac{1}{\hbar} Re\left(\frac{1}{\omega_{J'J} - \omega - \imath\gamma_{JJ'}/2} + \frac{1}{\omega_{J'J} + \omega + \imath\gamma_{J'J}/2}\right). \quad (2.54)$$

A detailed theoretical treatment of the formalism introduced in this section can be found in the appendix of [104].

2.2.3 Optical pumping

The symmetries of the dipole moment dictate that all the excited state sublevels $|F_e, m_{F_e}\rangle$ decay with the same rate, Γ, with the population branching into various ground state sublevels $|F_g, m_{F_g}\rangle$ according the the relative transition strengths (essentially the same as the square of the CG coefficients). This couples the ground state populations in the presence of a light field driving $|F_g\rangle \rightarrow |F_e\rangle$, with average rates determined by the absorption rates and the relative transition strengths, leading to an incoherent redistribution of population between ground state sublevels. This process is called optical pumping.

The steady-state ground level population distribution can be approximated by calculating the rate of optical pumping following a simplified approach described in [105]. Consider a set of ground $|g\rangle$ and excited $|e\rangle$ energy state manifolds, as shown in Figure 2.3, coupled via a light field driving the transitions between them. For any sublevel $|g_j\rangle$ in the ground manifold and $|e_k\rangle$ in the excited manifold, R_{jk} represents the absorption rate and β_{jk} represents the relative transition strength. We assume the transitions are driven below saturation in which case the time scale for the total process will be dominated by the slow driving rate. The spontaneous decay rate will then essentially be instantaneous, on the time scale relevant for the experiment. The rate of change of

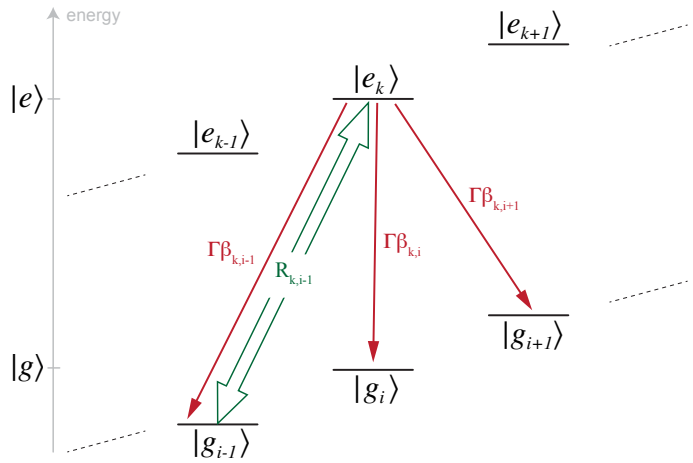

Figure 2.3: Two sets of discrete energy states manifold: one stable manifold labelled $|g_i\rangle$ and another consisting levels with short radiative lifetimes, labelled $|e_k\rangle$. The green double arrow represents the driving rate $R_{k,i-1}$ and the red arrow represents the spontaneous decay from the upper level. $\beta_{k,i-1}, \beta_{k,i}, \beta_{k,i+1}$ represents the relative transition strengths from the level $|e_k\rangle$. Contributions from all other pairs of ground-excited state can be similarly considered.

ground state populations g_i can then be evaluated by

$$\frac{d}{dt}g_i(t) = \sum_{j\neq i} g_j(t)\left[\sum_k R_{jk}\beta_{jk}\beta_{ik}\right] - g_i(t)\sum_k R_{ik}\beta_{ik}(1-\beta_{ik}). \tag{2.55}$$

The sum over j is over all ground state levels, and the sums over k go over all excited states. The first term expresses the transfer of population to the $|g_i\rangle$ ground state from all other ground states, while the second term expresses the population transferring out of the $|g_i\rangle$ ground state.

2.3 Cooling and Trapping of Neutral Atoms

A particularly useful tool for studying atom-light interactions is to cool the ensemble of atoms downs to low temperatures, thereby reducing their thermal motion and increasing the interaction time which is key for precise measurements. The interaction time can be further increased by trapping the cold atoms in some form of an atomic trap. A detailed discussion on different types of traps can be found in [99]. We will be considering the magneto-optical trap (MOT), successfully developed in 1985, which uses a method of laser cooling to cool a gas of neutral atoms down to few tens of μK and a quadrupolar magnetic field distribution to assist in trapping at the zero of the magnetic field.

Laser cooling Laser cooling relies on slowing down atoms due to transfer of momentum from the resonant laser field. With the laser field tuned to near resonance, an atom scatters an incoming photon by absorbing and spontaneously emitting a photon

in a random direction. While the photon absorption results in a momentum transfer to the atom in the direction of the laser field propagation, the momentum kick due to spontaneous emission averages to zero over many scattering event. Atoms thus get a net momentum kick in the direction of laser field propagation.

The cooling is achieved by making the photon scattering rate velocity dependent. Considering the 1-dimensional case of two counter-propagating laser fields (in the low intensity limit), the total scattering force experienced by an atom with a velocity $\mathbf{v}$ is given as (refer Equation 2.26)

$$\mathbf{F} = \hbar\mathbf{k}\frac{\Gamma}{2}\left[\frac{s_0}{1+s_0+4(\Delta-\mathbf{k}\cdot\mathbf{v})^2/\Gamma^2} - \frac{s_0}{1+s_0+4(\Delta+\mathbf{k}\cdot\mathbf{v})^2/\Gamma^2}\right]. \tag{2.56}$$

While writing this equation, we have included the Doppler shift $\pm\mathbf{k}\cdot\mathbf{v}$ experienced by the moving atom with respect to the two counter-propagating fields. In the limit of small velocities, $|\mathbf{k}\cdot\mathbf{v}| \ll \Gamma$, Equation 2.56 reduces to

$$\mathbf{F} \approx \frac{8\hbar k^2\Delta s_0}{\Gamma(1+s_0+2(\Delta/\Gamma)^2)}\cdot\mathbf{v} = -\beta_D\cdot\mathbf{v}, \tag{2.57}$$

where we have introduced β_D as a damping coefficient, acting against the atomic velocity. We can see that the atomic motion is viscously damped for the case $\Delta < 0$. The atoms selectively scatter photons that they see Doppler-shifted into resonance and thus, by detuning the laser field to the red of resonance, atoms scatter photons at a higher rate if moving toward the laser field than if moving away from it. This configuration is known as 1D optical molasses because of the viscous nature of the damping force. The atoms can be slowed down in all three spatial dimensions and thus cooled down with three pairs of counter-propagating laser beams, a pair in each dimensions. **Magneto-optical trap (MOT)** The atoms in the optical molasses created via laser cooling would simply diffuse out of the molasses region without any spatial dependence of the optical force. A MOT uses an inhomogeneous magnetic field to achieve the required spatial dependence of the optical force via the position-dependent Zeeman shift of the magnetic states of the atoms in order to localize them to a particular region.

A quadrupolar magnetic field is generated with a pair of coils in an anti-Helmholtz[1] configuration. This produces a linearly increasing magnetic field away from the center of the anti-Helmholtz pair where the magnetic field $\mathcal{B} = 0$ (refer Figure 2.4). This is particularly useful as it provides an easy way to define a central region for trapping atoms. As the atoms move further away from the trap, the detuning of the magnetic states shifts relative to the magnetically insensitive state $m_F = 0$. This asymmetry in detuning causes the atoms to scatter light preferentially from the cooling beams that are counter to the atoms motion away from the trap, hence pushing the atoms toward the center of the trap where there is no preferential scattering.

We will consider a simplified one dimensional model with two-level atoms to understand the principle of the MOT. We assume the atom has a ground (excited) state with

[1] An anti-Helmholtz pair consists of two identical circular coils with radius R each placed symmetrical along a common axis and separated by distance R, with equal currents going through the coils in opposite direction.

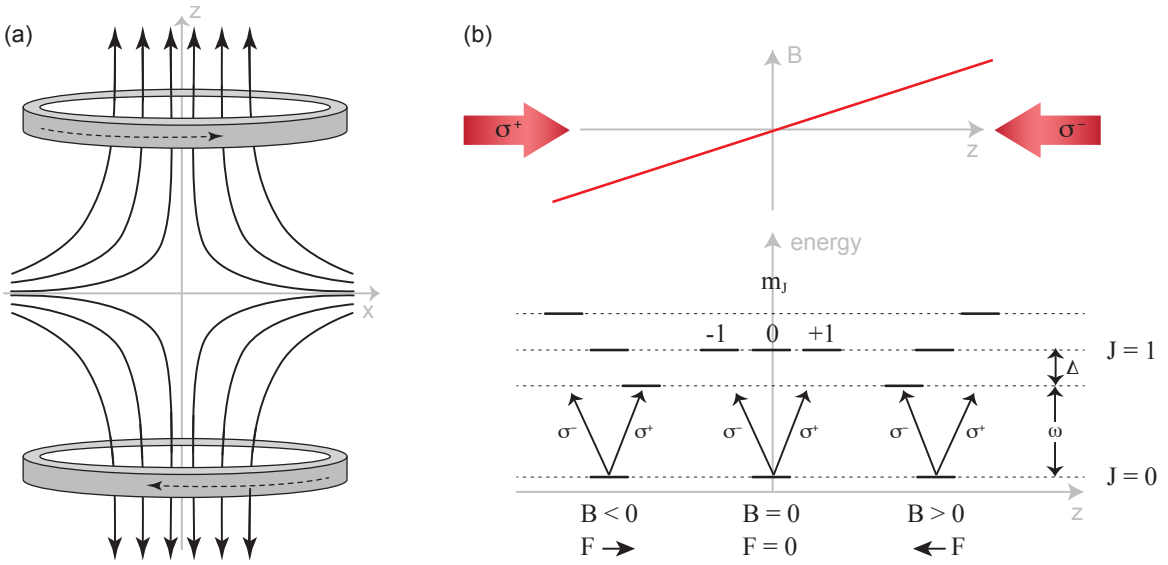

Figure 2.4: Principle of a MOT. (a) Coil geometry in an anti-Helmholtz configuration with their magnetic field lines. The arrow on the coils shows the direction of the current through them. (b) Mechanism of the MOT for an atom with $J = 0 \rightarrow J = 1$ transition. (Top) The coil configuration creates a linear magnetic field across the center of the trap with the zero field at the center. (Bottom) The spatially-dependent Zeeman-splitting and the selection rules for dipole transitions cause a particular sublevel to be resonant with each of the circularly polarized light beams. The net scattering force pushes the atoms toward the center of the MOT.

total angular momentum $F_g = 0$ ($F_e = 1$) and we only consider the dynamics in the z-direction. The principle of the MOT is schematized in Figure 2.4b. Along the z-axis, the excited state split into the three magnetic states given by $m_F = 0, \pm 1$ with the detuning of the form κz, where z is the position of the atom and $\kappa = \mu_B \hbar (d\mathcal{B}/dz)^{-1}$. In the region $z < 0$, $m_F = +1$ is shifted down while $m_F = -1$ is shifted up. The inverse is true for the region $z > 0$. For the cooling beams along the z-direction, we shine a right (σ_+) circularly polarized beam propagating from the left and a left (σ_-) circularly polarized beam propagating from the right. The selection rules impose that σ^+ (σ^-) can only cause transitions to $m_F = +1$ ($m_F = -1$). For appropriate red detuning of the cooling beams, atoms moving left are more likely to scatter the σ^+ light in the region $z < 0$ as the σ^+ light is closer to resonance while the opposite is true for the region $z > 0$. Thus the net effect on atoms from the cooling beams is toward the center of the trap where $\mathcal{B} = 0$.

2.4 Conclusion

This chapter introduced the main theoretical ideas and concepts that are relevant to the work presented in this thesis. A simple treatment of a two-level atom interacting with a classical field was discussed. Using the optical Bloch equations, the concept of polarizability was first introduced for the case of a two-level atom and then was

extended for multilevel atoms. It is particularly useful for the understanding of light shifts and dipole trapping. Finally, the physical idea behind laser cooling and trapping of atoms in a magneto-optical trap was explained. The next chapter will outline the technical details of the experimental setup we used.

Chapter 3

Experimental Details

In the preceding chapter, the theoretical background for the experiments has been discussed. This chapter focuses on the design[1] and the important technical details for the experiments reported in the following chapters.

3.1 Cold Atomic Ensemble of Rubidium Atoms

Experiments carried out in this thesis research use ^{87}Rb, which is a non-stable isotope of rubidium albeit with an extremely slow decay rate [106] having a half-life of 4.88×10^{10} years. Alkali atoms are often chosen for atom-light experiments because they have a relatively strong interaction of the induced dipoles with the EM field via D-transitions. They offer almost perfectly closed cyclic transitions (see Figure 3.1) which are accessible by readily available commercial tunable diode lasers, allowing for laser cooling and trapping in a MOT. Additionally, it is simpler to study and predict their behavior owing to their hydrogen-like structure with a single outer electron.

3.1.1 Vacuum setup

The preparation of cold atoms in a MOT critically depends on the collision rate between the atoms and any background gas. In order to maximize the trap lifetime, the experiments require ultra high vacuum (UHV) conditions (i.e., pressure $< 10^{-8}$ mbar). UHV is created using a combination of a scroll and a turbo-molecular pump TPS Compact (with TV81M turbo-molecular pump, Agilent Technologies) initially and is maintained with the continuous operation of an ion-pump (VacIon Plus Starcell 55, Varian). Our setup (see Figure 3.2) consists of a main MOT chamber, a custom-made octagonal stainless steel chamber with 10 ConFlat (CF) flanges: $8 \times 2.75''$ and $2 \times 4.5''$ CF, that contains a U-shaped aluminum mount for the ONF passing vertically through the center of the chamber. The U-mount fits in a cylindrical base, which is attached to one of the flanges of the MOT chamber. Optical access for the MOT beams, probe beams, and the cameras is provided by the seven viewports ($6 \times 2.75''$ and $1 \times 4.5''$ CF ports) which are anti-reflection (AR) coated for near-infrared (NIR) wavelengths.

[1] The cold atom system has been built by previous unit members over many years. The setup is modified as per requirements for each of the experiments carried out in this thesis research.

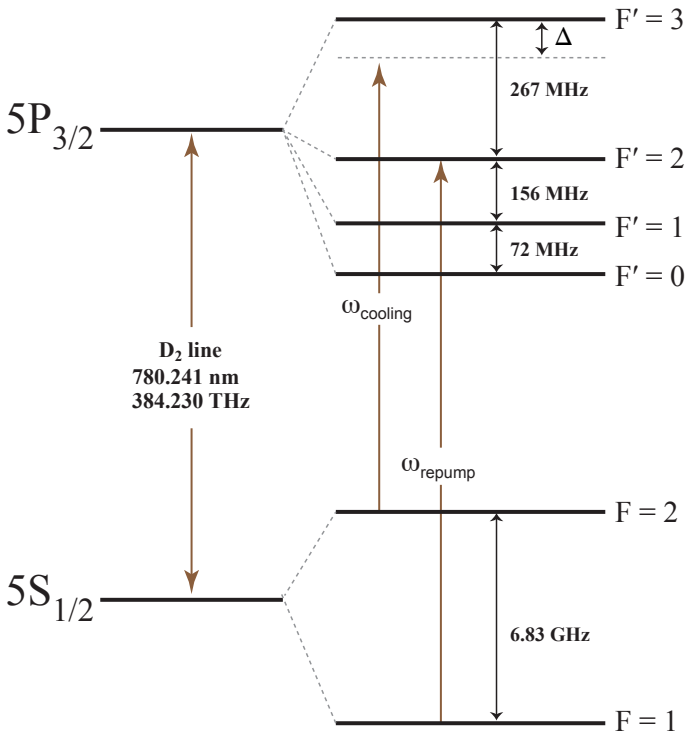

Figure 3.1: Hyperfine energy levels of the D_2 line of ^{87}Rb showing the cooling and the repump transitions.

The two pigtail ends of the ONF enter and exit the chamber from the top and bottom 2.75″ flanges through teflon-based vacuum feedthroughs. The back port of the MOT chamber is connected to a pneumatic valve via a four-way cross (4X), with the remaining two ports of the 4X fitted with the electric feed throughs where rubidium dispensers (SAES Rb Getters) containing chemically bound rubidium are attached. They release atomic rubidium when electrically heated to about 500°C. The other side of the penumatic valve is connected to a six-way cross (6X), with the diametrically opposite CF port fitted with a 4.5″ CF viewport with AR coating for the MOT beams access. The top flange of the 6X is connected to a titanium sublimation pump (Agilent TSP Filament Cartridge). On one side a 4X is fitted and blanks on the remaining two flanges. The 4X is connected to the ion-pump using a stainless steel bellows. The top flange of the 4X is connected to a vacuum gauge (Dual Filament Bayard-Alpert Pirani Guage, FRG730CF35S, Agilent Tehnologies). The bottom flange is connected to a T-valve (rated to 10^{-12} mbar) and to a TPS Compact via a flexible metal bellow. All the flanges are CF and copper gaskets are used to seal the vacuum. This system was originally designed in 2003 and has been used for all ONF-atom work from the group since then [42, 51, 55, 56, 107–111].

3.1.2 Laser system

^{87}Rb has two D-lines: the D_1 transition $5S_{1/2} \rightarrow 5P_{1/2}$ and the D_2 transition $5S_{1/2} \rightarrow 5P_{3/2}$. We chose the D_2 transition for cooling and trapping of ^{87}Rb atoms using the

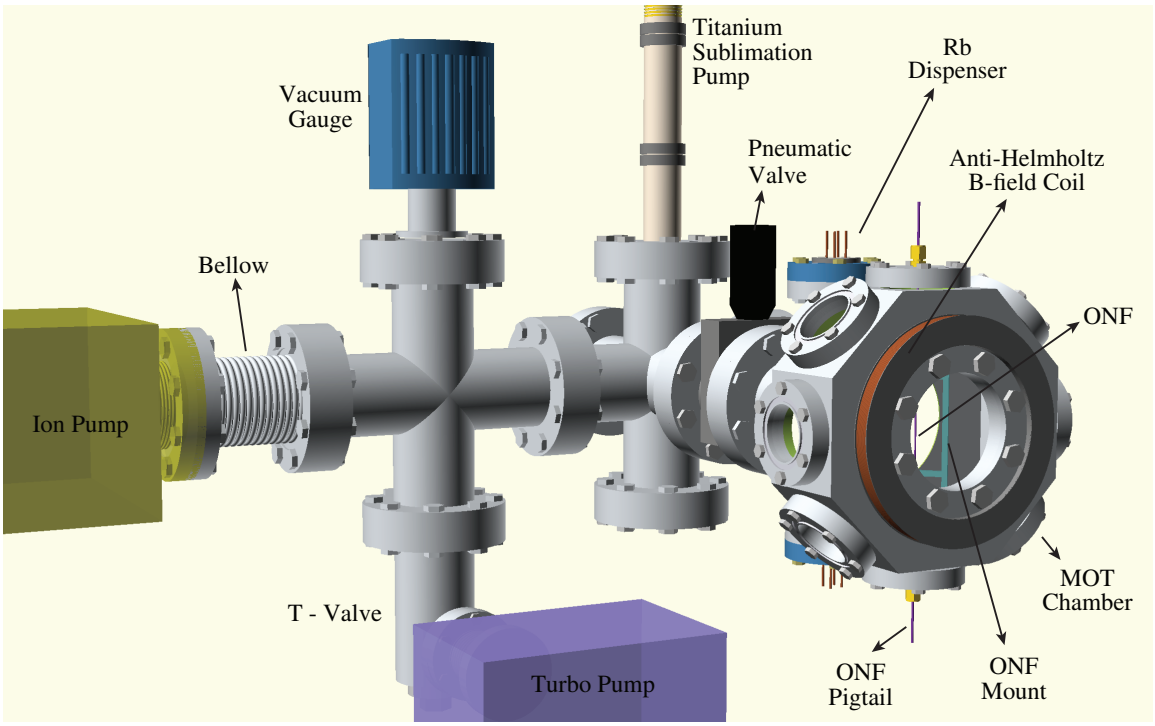

Figure 3.2: Illustration of the vaccum assembly of the experimental setup.

scheme described in Section 2.3. The hyperfine structure of ^{87}Rb and the relevant transitions for cooling are shown in Figure 3.1. The *cooling laser* addresses the closed cycle transition $5S_{1/2}(F = 2) \rightarrow 5P_{3/2}(F' = 3)$, which we term the *cooling transition* from this point onwards. While the cooling transition is closed, the atoms can still be lost due to the finite probability of the $5S_{1/2}(F = 2) \rightarrow 5P_{3/2}(F' = 2)$ transition followed by spontaneous decay to the $5S_{1/2}(F = 1)$ ground state. For a typical condition in our setup, 1 in 1000 photon scatterings can take the atoms out of the cooling cycle. An additional *repump laser* tuned to the $5S_{1/2}(F = 1) \rightarrow 5P_{3/2}(F' = 2)$ transition is used along with the cooling beams to bring the lost atoms back into the cooling cycle.

A schematic of the laser cooling system is shown in Figure 3.3. The cooling beam is derived from a commercial extended-cavity diode laser (ECDL) with a tapered amplifier (TA) system (Toptica TA Pro) running at $\approx$ 780.241 nm. The laser is locked with a computer-controlled laser-locking module (Toptica DigiLock110) to the $5S_{1/2}(F = 2) \rightarrow 5P_{3/2}(F' = [2,3]_{co})$ line in the D_2 spectrum which is obtained through saturated absorption spectroscopy using a Toptica CoSy. The $[2,3]_{co}$ corresponds to the crossover line between the $5S_{1/2}(F = 2) \rightarrow 5P_{3/2}(F' = 2)$ and $5S_{1/2}(F = 2) \rightarrow 5P_{3/2}(F' = 3)$ transitions. Figure 3.4 shows the hyperfine-resolved saturated absorption spectrum for the D_2 lines. The cooling beam is passed through an acousto-optic modulator (AOM, ATM-602DA2B, IntraAction Corp, central frequency: 60 MHz) in a double-pass configuration producing a shift of 120 MHz. With this setup, we could maintain the frequency of the cooling laser at anywhere between 0 to ~40 MHz red-detuned from the cooling transition. We typically used 14 MHz red-detuning for most of the work in this thesis except for that reported in Chapter 6 where different detunings were explored by a machine learner in optimization of the cooling process for loading atoms

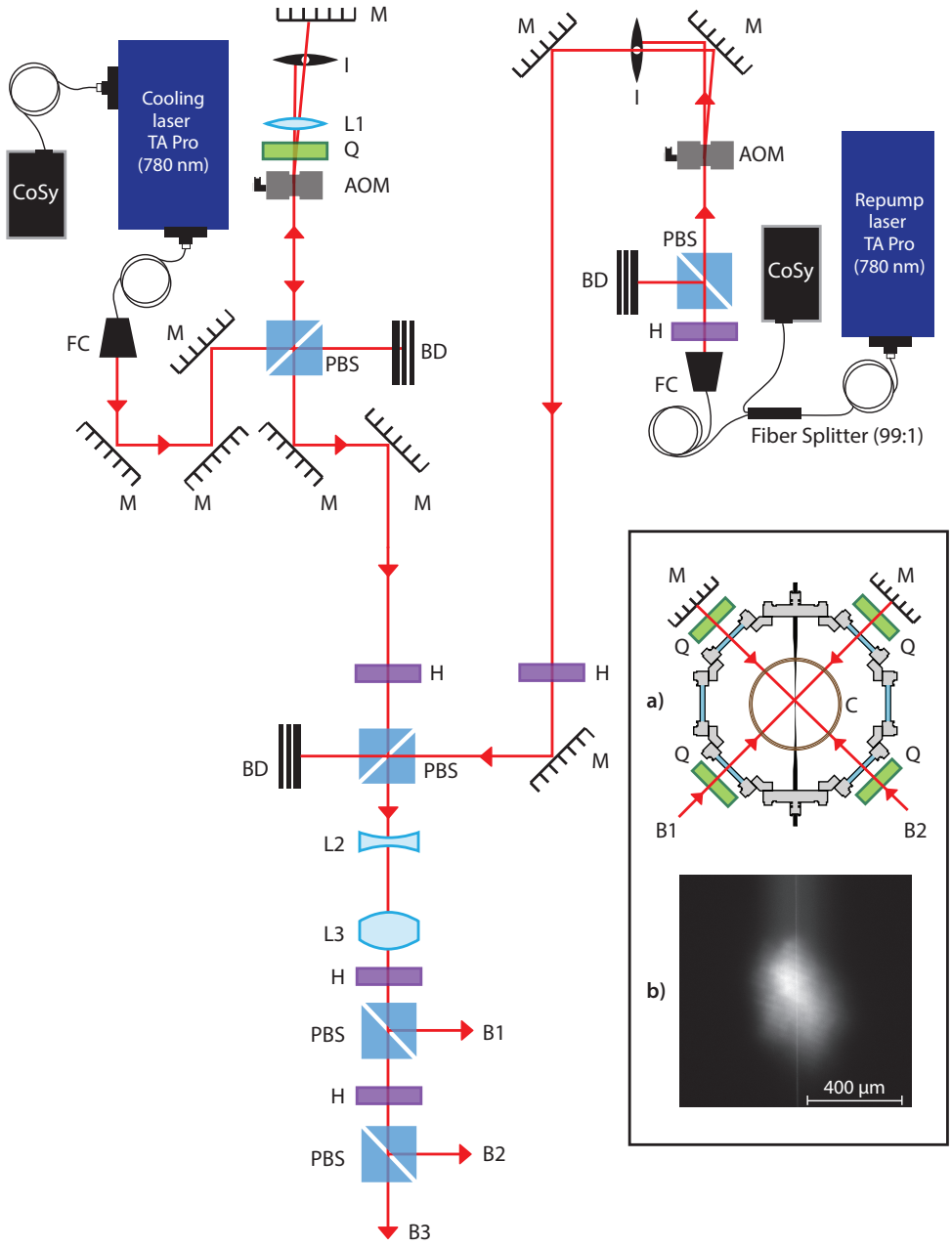

Figure 3.3: Detailed schematic of the optics for spatial and frequency control of the *cooling* and *repump* laser beams. Inset (a): Beams B1 and B2 retro-reflected in the MOT chamber at $+45°$ and -45° with respect to the x-axis in the xz-plane respectively. Beam B3 retro-reflected along the y-axis is omitted from the sketch. A ring like structure designated C and illustrated around the point of beams' intersection shows the anti-Helmholtz coils arrangement placed at $y = \pm 45$ mm with ONF in the $y = 0$ plane. Inset (b): An image of a typical cold atom cloud produced in our experiments. FC: Fiber coupler, M: Mirror, I: Iris, L1: Convex lens ($f = 75$ mm), Q: Quarter-wave plate, AOM: Acousto-optic modulator, BD: Beam dump, H: Half-wave plate, L2: Concave lens ($f = -50$ mm), L3: Convex lens ($f = 100$ mm), B1,B2,B3: Laser cooling beams retro-reflected in the MOT chamber.

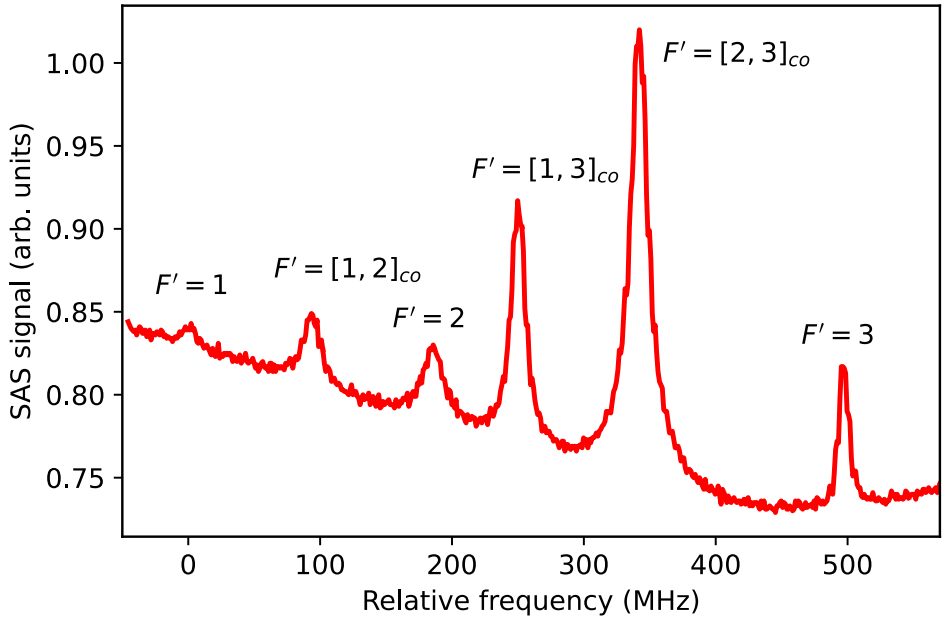

Figure 3.4: Saturated absorption spectrum showing the transition peaks in the D_2 $5S_{1/2}(F = 2) \rightarrow 5P_{3/2}$ lines of ^{87}Rb. The frequency is relatve to the $F = 2 \rightarrow F' = 1$ transition peak. The spectrum is obtained from the Toptica DigiLock interface.

in a fiber-based dipole trap.

The repump beam is derived from another ECDL (Toptica DL100 Pro), locked to $5S_{1/2}(F = 1) \rightarrow 5P_{3/2}(F' = [1, 2]_{co})$, which then is single-passed through an AOM (central frequency: 80 MHz) running at 78 MHz. Both the cooling and repump lasers have a typical linewidth of the order of 100 kHz. The cooling (60 mW) and repump (2 mW) beams are overlapped and expanded to a beam size of 15 mm in diameter. The overlapped and expanded beams are then split into three beams of equal intensities, passed through a quarter-wave plate (QWP) each, and aligned to intersect mutually orthogonally at the center of the vacuum chamber. The QWP transforms the original linear polarization of the beams to a circular polarization in accordance with the MOT requirement discussed in Section 2.3. The cooling configuration with counter-propagating orthogonal circular polarizations (σ^+-σ^-) is achieved by retroreflecting each of the beams through another QWP.

3.1.3 Magnetic fields

As discussed before in Section 2.3, the spatial localization of the atoms in a MOT is achieved through a combined effect of an optical and magnetic field. The magnetic field is provided by two coils in an anti-Helmholtz configuration. Two identical, circular, copper coils with 200 turns and radii 75 mm are placed symmetrically outside the vacuum chamber such that they are 90 mm apart and the zero of the magnetic field nearly coincides with the center of the chamber (see Figures 3.2 and 3.3). During a

typical steady-state loading of the MOT, the magnetic field gradient in the trapping volume and along the axis of the coils is set to 10-15 G/cm.

Additionally, three pairs of Helmholtz coils, along each of the three orthogonal directions, are used either to cancel any stray unwanted magnetic field or to add a uniform magnetic field in a certain direction such as to shift the center of the trap. The coils are individually connected to an insulated-gate bipolar transistor (IGBT) switch, which allows this magnetic field to be switched on and off during an experimental cycle.

3.1.4 Characterization of the cold ^{87}Rb atom cloud

Under suitable UHV conditions (pressure $\sim 3.0 \times 10^{-9}$ mbar, in our case), a cold atom cloud is formed in a MOT. In our case, the MOT is formed around an ONF (see Section 3.2 for details). Atoms in the cloud can be overlapped with the ONF by either using the three pairs of mutually orthogonal Helmholtz coils putting a bias magnetic field to shift the zero position of the magnetic field in the MOT, or by slightly misaligning the MOT cooling beams. Two cameras, imaging from the orthogonal directions, help identify the position of the atom cloud with respect to the ONF. The cloud overlap with the ONF is further optimized by monitoring the fluorescence coupled to the ONF.

Imaging The MOT cloud centered on the ONF is imaged with an EMCCD[2] camera (Luca^{EM} R, DL-604M-OEM, ANDOR Technologies) through one of the viewports in the MOT chamber, via a 2:1 telescope arrangement composed of two achromatic doublet lenses (L1: AC508-150B f=150 mm and L2: AC508-300B f=300 mm). The imaging system, as shown in Figure 3.5, is used for the characterization of the MOT cloud, including the temperature and the atom number and density. An additional triggerable CMOS[3] camera (Thorlabs DCC3240N) images the atom cloud from the orthogonal direction.

Temperature The atom cloud temperature is estimated via time-of-flight measurements, which are based on a measurement of the rate of thermal expansion of the cloud. The cloud expansion rate, $\Delta\tau$, is related to the temperature via

$$T_{\text{cloud}} = \frac{m_a \Delta\tau}{k_B} \tag{3.1}$$

where m_a is the mass of the atom and k_B is the Boltzmann constant. The anti-Helmholtz coils, the cooling, and the repump lasers are turned off to allow for the ballistic expansion of the cloud. The cloud diameter is imaged after a time t by simultaneously switching on the cooling beams to scatter fluorescence from the atom cloud and triggering the EMCCD camera for a snapshot. The images are collected by varying t in steps of 1–2 ms (see Figure 3.6). The cloud expansion rate is determined as the slope of the curve when the square of the cloud diameter is plotted as a function of the square of the expansion time.

Atom number and density The number of atoms in the atom cloud can be de-

[2]Electron-Multiplying Charge Coupled Device
[3]Complementary Metal Oxide Semiconductor

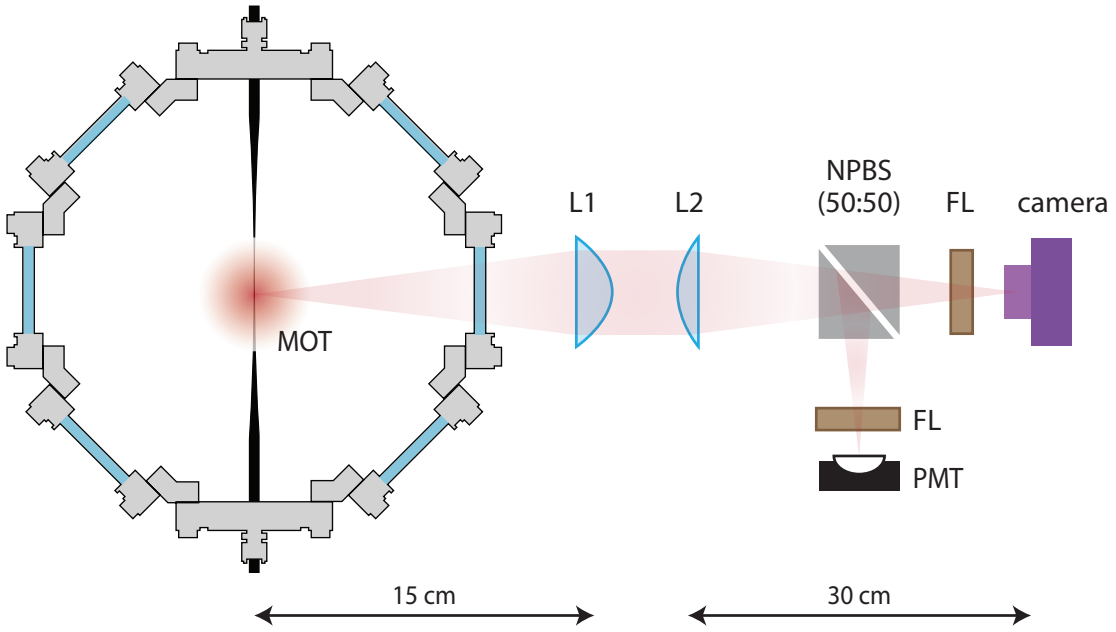

Figure 3.5: Sketch of fluorescence imaging of the atom cloud. L1,L2: Achromatic doublets, NPBS: Non-polarizing beam splitter, FL: Dichroic 780 nm narrow bandpass filter, PMT: Photo-multiplier tube.

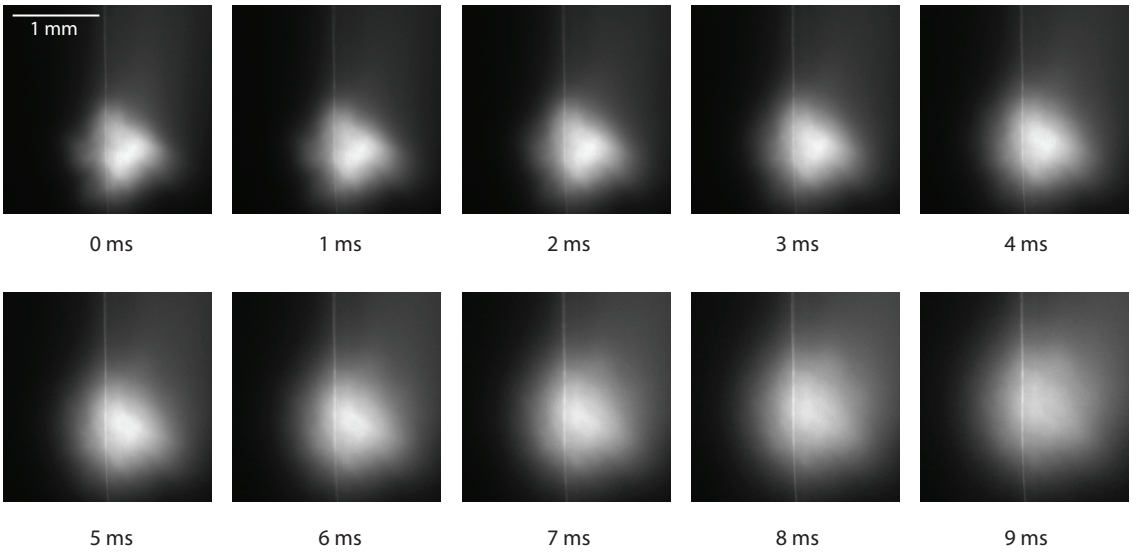

Figure 3.6: A series of snapshots of an atom cloud ballistically expanding when the MOT cooling laser and magnetic field are turned off. The value under each image corresponds to the amount of time the cloud was left to expand before taking the picture.

termined by either considering the image obtained through the EMCCD camera or a fluorescence signal collected on a photomultiplier tube (PMT). The PMT signal is obtained by splitting the fluorescence collected from the imaging telescope arrangement (see Figure 3.5) on a 50 : 50 beam splitter (BS). The power, P, corresponding to the PMT signal relates to the number of atoms, N_{atoms}, according to the following equation

$$P = N_{\text{atoms}}\Gamma_{\text{sc}}\Theta, \tag{3.2}$$

where Γ_{sc} is the scattering rate of atoms (see Equation 2.25) and Θ is the fraction of the solid angle from which the fluorescence is collected, i.e., the field-of-view of the imaging telescope. The counts, N_{counts}, collected on the EMCCD camera is also a measure of the number of atoms via

$$\frac{N_{\text{counts}}}{\eta t_{\text{exp}}} = N_{\text{atoms}}\Gamma_{\text{sc}}\Theta, \tag{3.3}$$

where η is the quantum efficiency of the EMCCD (48% at 780 nm) and t_{exp} is the exposure time. The average density is then calculated by estimating the volume of the MOT cloud from the image, with the knowledge that each pixel of the EMCCD is 8 µm × 8 µm in size. We typically measured around 5.0×10^6 atoms trapped in our MOT, with an average density of around 10^9 cm^{-3}.

3.2 ONF Embedded in the MOT Chamber

We began this chapter with a description of the first important tool of our experiments: the cold atomic ensemble. The second tool is the optical nanofiber, which was fabricated from a commercial single-mode optical fiber (SM800-5.6-125, Fibercore) via a flame-brushing technique [34]. The initial fiber diameter of 125 µm was exponentially tapered to around 400 nm at the waist, thereby producing a single-mode ONF for 780 nm wavelength light.

The ONF was mounted in the MOT vacuum chamber with a U-shaped aluminum holder attached to one of the CF flanges, as mentioned in Section 3.1.1, with the pigtails exiting from the top and the bottom CF flanges, respectively. The two pigtails provided access to the light fields coupled to the ONF. The installation procedure is described in the thesis of Dr. K.S. Rajasree [112][4]. Figure 3.7 shows a schematic of the optical paths coupling in and out of the ONF. During a typical operation, 100 µW of 1064 nm light was coupled into both the ends of the ONF, which kept the ONF hot and avoided atom deposition on the ONF surface. Additonally, it attracted atom toward the ONF surface due to the dipole force, thereby increasing the density of atoms in the evanescent field. Note that, when we refer to light power through the ONF, the values given are those measured at the output port of the fiber and not at the ONF waist. For this we assumed that most losses are at the input coupling and the down-taper of the ONF. In our case, the ONF was optimized for 780 nm propagation and the adiabaticity criterion may not be matched for other wavelengths leading to high loss at the down-taper. There may be additional wavelength-specific material losses,

[4]The single-mode ONF was fabricated and installed by Dr. K.S. Rajasree and Dr. T. Ray before the beginning of my PhD.

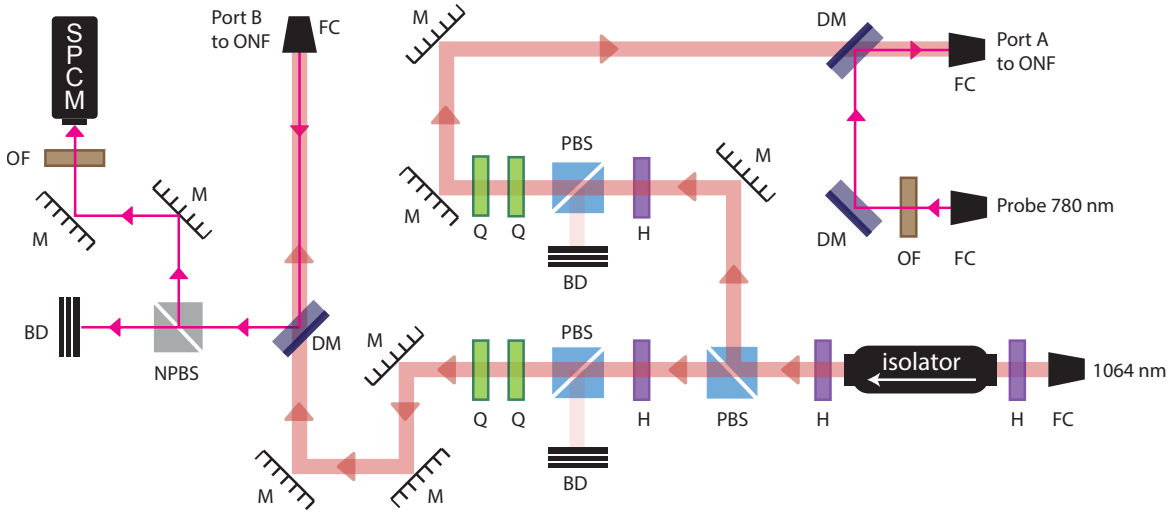

Figure 3.7: Optical layout for coupling light in and out of the ONF. Light field transmitted through the ONF from Port B was directed on to an SPCM. OF: 780 nm narrow bandpass optical filter, M: Mirror, BD: Beam dump, NPBS: Non-polarizing beam splitter, DM: Dichroic mirror (Thorlabs DMLP950), PBS: Polarizing beam splitter, Q: Quarter-wave plate, H: Half-wave plate, FC: Fiber coupler.

which we assumed to be minimal. The 1064 nm light was from a Mephisto 1064 nm high power laser providing up to 450 mW of power. The same 1064 nm laser was used as a source of counter-propagating red-detuned beams for the evanescent field dipole trap reported in Chapter 6. The 1064 nm beam was passed through an AOM (MT80-A1-1064, AA Optoelectronics, central frequency: 80 MHz) to control the power of the beam via amplitude modulation.

The output from one of the ONF ports was coupled to a single-photon counting module (SPCM, SPCM-AQRH-14-FC, Excelitas Technologies). The quantum efficiency of the SPCM at 780 nm is 60% and the dark count is 100 counts/s. The fluorescence from the atoms in the vicinity of the ONF was coupled into the fiber and then registered on the SPCM as photon counts. Figure 3.8 shows typical photon counts during a MOT loading process.

3.2.1 Single-mode ONF and the fundamental HE_{11} mode

A commercial step-index optical fiber is composed of a cylindrical dielectric core with refractive index n_{co} surrounded by a cladding with a slightly lower refractive index n_{cl}, such that $n_{co} - n_{cl} \ll 1$. The cladding and the core regions are made of pure and doped silica respectively, with a typical refractive index difference of ~ 0.001. This is called the weakly-guiding regime. For weakly-guiding fibers, the field mode solutions can be approximated to homogeneous linearly polarized (LP) modes. In the case of an ONF, the cladding of the original fiber forms the core of the ONF, while the cladding is formed by the material in which the ONF is embedded. For the case relevant to this thesis, the ONF was embedded in vacuum + Rb atoms and thus the transverse confinement of the field mode is due to the silica-vacuum refractive index difference

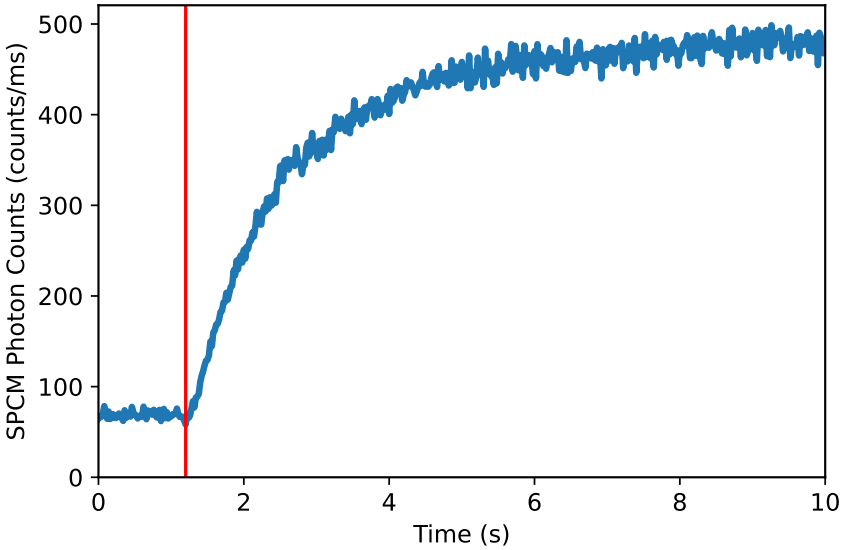

Figure 3.8: SPCM photon counts from the atom cloud fluorescence coupled to the ONF as a function of time, during a typical MOT loading sequence. The vertical red line indicates the time at which the cooling and repump beams were switched on.

(~ 0.45), ignoring the small effect due to the Rb atoms. In this strongly-guiding regime, the previous approximation is not valid and a full vector model had to be considered to find the exact solutions of Maxwell's equations. The properties of the EM field in waveguides are described in much detail in [113]. This includes the case of step-index fibers and ONFs. A short summary of guided and radiated modes in ONFs can be found, for example, in the appendices of [114].

An ONF can be modeled as a dielectric cylinder of radius a and refractive index n_1 surrounded by an infinite background medium of refractive index n_2, where $n_2 < n_1$. A general solution has six-hybrid field components. The TE modes have a transverse electric field, but have both a transverse and longitudinal magnetic field. The TM modes have a transverse magnetic field, and have both transverse and longitudinal electric field. The HE and EH modes (hybrid modes) consist of both transverse and longitudinal components for both electric and magnetic field components. For a guided light field of frequency ω (vacuum wavelength $\lambda = 2\pi c/\omega$ and wave number $k = \omega/c$), the allowed modes are characterized by the propagation constant, β, determined by the eigenvalue equation [114]

$$\left[\frac{J_l'(ha)}{haJ_l(ha)} + \frac{K_l'(qa)}{qaK_l(qa)}\right]\left[\frac{n_1^2 J_l'(ha)}{haJ_l(ha)} + \frac{n_2^2 K_l'(qa)}{qaK_l(qa)}\right] = l^2\left(\frac{1}{h^2a^2} + \frac{1}{q^2a^2}\right)^2 \frac{\beta^2}{k^2}. \quad (3.4)$$

The parameters $h = (n_1^2k^2 - \beta^2)^{1/2}$ and $q = (\beta^2 - n_2^2k^2)^{1/2}$ characterize the scales of the fields inside ($r < a$) and outside ($r > a$) the ONF. The integer index $l = 0, 1, 2, ...$ is the azimuthal mode order, which determines the phase gradient in the transverse plane. The J_l and K_l denote the Bessel functions of the first kind and the modified Bessel

functions of the second kind, respectively. One can limit the number of allowed modes by decreasing a dimensionless quantity called the normalized frequency, or V-number, defined as

$$V = \frac{2\pi}{\lambda} a \sqrt{n_1^2 - n_2^2}. \tag{3.5}$$

For a given wavelength, the number of allowed modes reduces with decreasing fiber radius. Each mode exhibits a cut-off for the V-number, see Figure 3.9, below which the mode cannot propagate. Only one mode remains for $V < 2.405$, this is the fundamental mode, HE_{11}. The ONF is then termed single-mode. The ONF embedded in our MOT chamber was ∼400 nm in diameter and was therefore single-mode for all the wavelengths involved in this thesis work except for 516.6 nm (used for the quadrupole transition work reported in Chapter 4) for which the first group of higher order modes, TE_{01}, TM_{01}, and $HE_{21,eo}$, could propagate. We have seen elsewhere that, by coupling the HE_{11} mode into the input fiber pigtail to the ONF, the amount of coupling into higher order modes is minimal [115, 116].

We restrict our discussion to the fundamental, HE_{11}, mode as we only worked with this. Figure 3.10 shows the intensity profile of the HE_{11} mode for a 400 nm diameter ONF with linear polarization along the x-axis at the fiber input with the ONF axis along z. While fully transverse polarization is possible in free-space propagation, the transverse confinement of the field in the ONF produces a longitudinal field along the direction of the propagation. Thus, the polarization of the HE_{11} at the ONF waist is not strictly linear and is referred to as *quasi-linearly polarized* along the x-axis. A derivation of the mode solutions and relevant field expressions for inside and outside the ONF are given in Appendix A. There is a strong discontinuity of the electric field intensity at the ONF surface. In the evanescent field region, the intensity is maximal in the plane $y = 0$. In this plane, the polarization is elliptic, rotating around the y-axis with opposite directions in the $y > 0$ and $y < 0$ region. This chiral behavior on the two sides of the ONF has been studied [117] and led to demonstrations of chiral light-matter interactions with ONFs, directional spontaneous emission [118], and nonreciprocal light transmission [119].

3.2.2 Setting the polarization of the guided HE_{11} mode

We adapted the technique developed by Dr. G. Tkachenko in our unit for complete control of the polarization state in a single-mode ONF [97]. The commercial fibers used for the fabrication of the ONFs were not polarization maintaining (PM)[5]. The polarization transformation from the input of the fiber to the ONF waist depends strongly on the birefringence of the whole fiber including the pigtail and the down-taper region. The birefringence, sensitive to any stress[6] in the fiber and to its temperature, could be compensated by placing a free-space polarization compensator (PC) before the

[5] This is mostly due to the rotational invariant nature of the PM-fibers that makes it simpler to work with. Additional simplicity comes from the fabrication perspective as the fabrication of an ONF from a PM-fiber is technically challenging due to its highly birefringent construction.

[6] One unavoidable source of stress is from the teflon ferrules in the vacuum feedthroughs through which the ONF pigtails enter and exit the MOT chamber. The ferrules have to be squeezed tightly around the pigtail in order to avoid any leakage and to maintain UHV conditions.

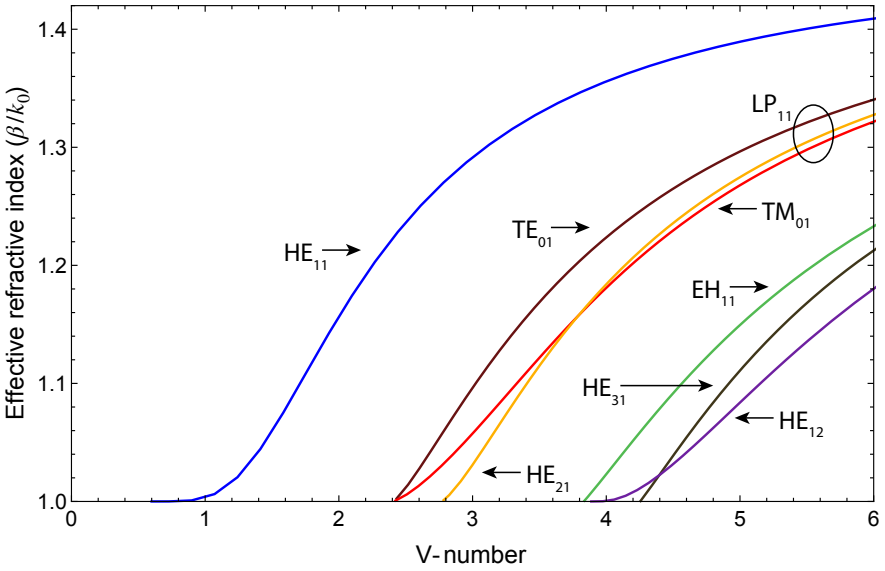

Figure 3.9: Effective refractive indices for few fiber modes plotted against V-number.

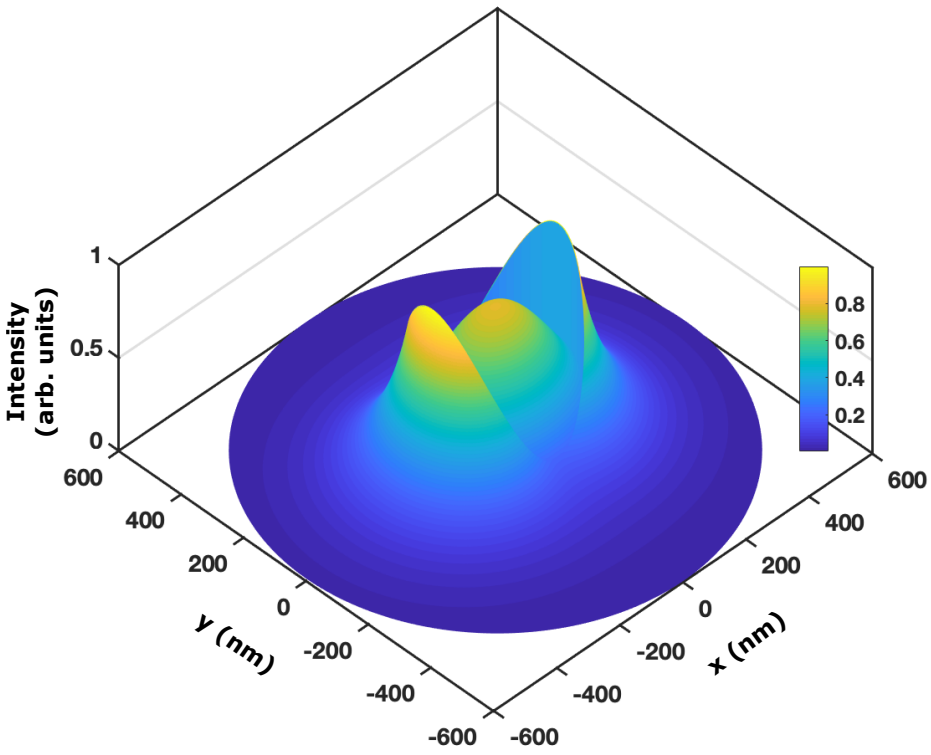

Figure 3.10: Intensity profile inside and outside the ONF (diameter 400 nm) for 780 nm light propagating in the HE_{11} mode, quasi-linearly polarized along x. The color bar indicates the intensity in arbitrary units.

fiber. This method relies on the fact that, in adiabatically tapered fibers, polarization transformations are restricted to 3D rotations of the Poincaré sphere. The key to the

method is sequentially mapping two different nonorthogonal linear polarization states at the input to their respective polarization states at the ONF waist.

A crucial component for the polarization mapping is identification of the polarization in the ONF. It is typically identified with Rayleigh imaging [120, 121] of the light scattered from the ONF, due to inherent imperfections, in a direction orthogonal to the ONF axis. The imperfections are supposed to be dipole Rayleigh scatterers which means the scattered light preserves the polarization and no light is scattered in the direction of linearly polarized excitation. Filtering out the inherent longitudinal component of the HE_{11} mode, an arbitrary polarization state of the transversal part of the HE_{11} mode can be determined by monitoring the Rayleigh scattering from two different directions, both orthogonal to the ONF axis.

Tkachenko et al. [97] developed a method that requires only one lens and a video camera, greatly reducing the optical access requirements. It is particularly useful for experiments with severe geometric constraints, like ours where the ONF was mounted inside a vacuum chamber with limited optical access. The method relies on capturing a blurred image of the ONF at the y' plane in contrast to a diffraction-limited sharp image in the imaging plane (at $y = y_{im}$), see Figure 3.11. For the blurred image, the integrated brightness Σ_1 and Σ_2 (corresponding to $x > 0$ and $x < 0$ respectively) shows a noticeable change with varying polarization states, while there is no noticeable change for the sharp image. The quantity $\Sigma = \Sigma_1 + \Sigma_2$ has the global maximum (minimum) when the transverse component of the HE_{11} mode is x-polarized (y-polarized). In turn $\Delta = \Sigma_2 - \Sigma_1$ has the global maximum (minimum) when the mode is in diagonal (anti-diagonal) linear polarization, oriented at $+45°$ (-45°) with respect to x. To maximize the precision of Δ measurements, we used the lenses L1 and L2 (in Figure 3.11) with a diameter of 50 mm, thus achieving a maximum collection angle $\alpha \approx 18°$. The errors in the state identification are expected to be less than 10° on the Poincaré sphere [97].

The polarization compensation is then achieved in two steps. First, x-polarized light at input is mapped to a quasi-linear x-polarized HE_{11} by putting a pair of QWPs at the input. The QWPs are independently rotated until Σ is maximized. Second, the input is switched to the diagonal polarization and a variable retarder (VR, liquid-crystal type, Thorlabs LCC1111-C) is introduced before the QWPs. The VR is rotated to maximize Δ, mapping the input diagonal polarization with the diagonal polarization in the ONF. Application of this polarization control technique will be discussed in Chapters 5 and 6.

3.3 Conclusion

This chapter provided most of the details of the experimental systems, including the laser systems, vacuum components and imaging system, that were used in this thesis work. The properties of a single-mode ONF and its guided mode were discussed. The chapter concluded with the description of the method to control the polarization of the ONF-guided HE_{11} mode. In the following chapters, we will discuss results obtained using this experimental setup.

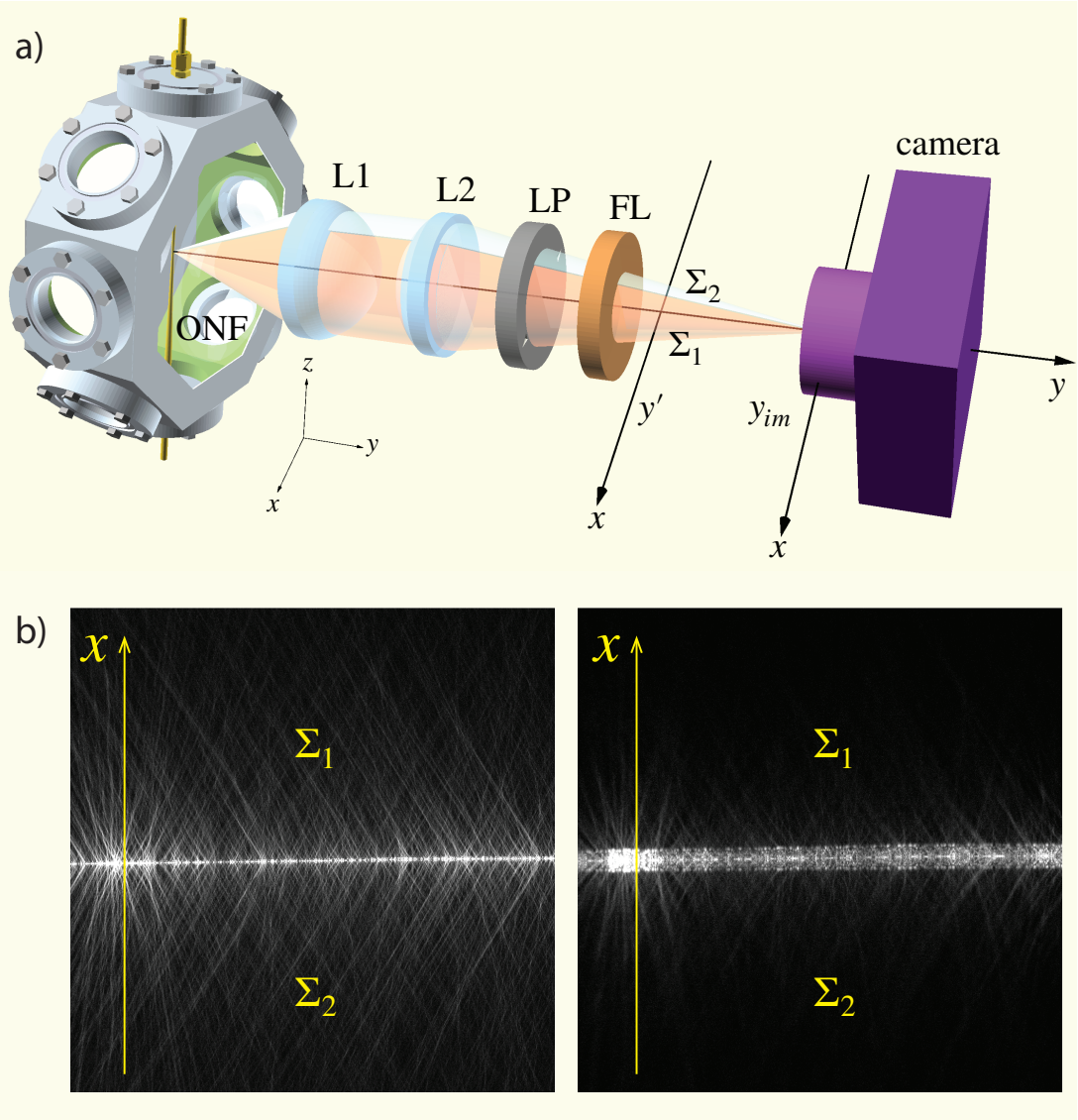

Figure 3.11: Identification of ONF-guided HE_{11} mode polarization. (a) Sketch of the imaging system for polarization identification. L1: Plano-convex lens ($f = 75$ mm), L2: Plano-convex lens ($f = 125$ mm), LP: Linear polarizer, FL: Dichroic filter (780 nm narrow bandpass filter). (b) A sharp (at $y = y_{im}$) and a blurred (at $y = y'$) image of the ONF. Σ_1, Σ_2 are the sum of the brightness for $x > 0$ and $x < 0$ respectively. Σ_1 and Σ_2 cannot be distinguished in the sharp image, but are distinguishable in the blurred image.

Chapter 4

Quadrupole Excitation Mediated via an Optical Nanofiber[1]

In Chapter 3, we have discussed the preparation of our ONF-MOT experimental setup. The crucial point is that an ONF (diameter ∼400 nm, single-mode for 780 nm) was mounted in UHV, such that a cold ^{87}Rb atom cloud surrounded the ONF and the guided light field could interact with the atoms via the evanescent field. The ONF-MOT system is ideal to study atomic transitions that are hard to access in free-space experiments.

Following recent theoretical results from our group on an ONF-mediated enhancement of the $5S_{1/2} \rightarrow 4D_{5/2}$ quadrupole transition for a ^{87}Rb atom in the evanescent field of an ONF [123], we proceeded to do the experiment. This chapter reports on the experimental observation of the 516.6 nm (vacuum wavelength) electric quadrupole excitation in a cloud of laser-cooled ^{87}Rb atoms mediated by an ONF using a continuous-wave (CW) guided field. However, we considered the $5S_{1/2} \rightarrow 4D_{3/2}$ quadrupole excitation in ^{87}Rb instead, due to technical issues related to photon detection for the subsequent decay channels (as discussed in Section 4.3).

The chapter starts with an introduction outlining the relevance of this work in atomic and molecular physics. This is followed by a brief review of the theoretical result showing the enhancement of the quadrupole transition in an alkali-metal atom interacting with the guided mode of an ONF [123] and some useful notations are introduced. Finally, the results of our experiment demonstrating the $5S_{1/2} \rightarrow 4D_{3/2}$ quadrupole transition in ^{87}Rb are presented.

[1]This chapter is adapted from the work published as T. Ray, R.K. Gupta, V. Gokhroo, J.L. Everett, T. Nieddu, K.S. Rajasree and S. Nic Chormaic, "Observation of the ^{87}Rb $5S_{1/2} \rightarrow 4D_{3/2}$ electric quadrupole transition at 516.6 nm mediated via an optical nanofibre", New J. Phys. **22** (2020) 062001 [122]. RKG contributed to the work by assembling the frequency reference setup, collecting and plotting the experimental data, and by participating in the writing of the research article.

4.1 Electric Quadrupole Transitions

The multipole expansion of the energy of a charge distribution in an external field can be written as [124],

$$E = q\Phi(0) - \mathbf{d}.\mathbf{E}(0) - \frac{1}{6}\sum_i \sum_j Q_{ij} \frac{\partial E_j}{\partial x_i}\Big|_0 + \cdots \tag{4.1}$$

where $\mathbf{d}$ is the dipole moment and Q_{ij} is the quadrupole moment tensor component of the charge distribution. The simplest and generally the strongest interaction between the EM field and matter is the electric dipole (E1) interaction – the first radiating term in a multipole expansion. The commonly used selection rules for atomic transitions are based on the electric dipole approximation and the effect of the higher order terms are frequently neglected, leading to what are known as dipole forbidden transitions. The strength of the optical transitions can be defined in terms of several different paramaeters, such as the Einstein A and B coefficients, the dipole moments, or the oscillator strengths (i.e. the f values) [125]. The electric dipole Rabi frequency is linearly proportional to the electric dipole moment and the electric field amplitude of the light (see Section 2.1). The corresponding E1 oscillator strengths are propotional to the square of the dipole moment and, hence, the square of the E1 Rabi frequency.

The next term in the multipole expansion is the electric quadrupole (E2). Quadrupole transitions play an important role in atomic and molecular spectroscopy [126–128] with relevance in photochemistry, atmospheric physics, and fundamental processes [129], to name just a few. The E2 Rabi frequency is linearly proportional to the quadrupole moment and the gradient of the light field. Similarly to the E1 case, the oscillator strength for an E2 transition is proportional to the square of the E2 Rabi frequency. This implies that the E2 oscillator strength depends on the gradient of the electric field. Due to this dependency, E2 transitions are less studied than their E1 counterparts as it can be challenging to create a large enough field gradient experimentally. Note that the E2 oscillator strength is also proportional to the square of the E2 Rabi frequency.

Several platforms for driving E2 transitions in alkali atoms have been proposed and/or demonstrated, with recent particular focus on the $S \rightarrow D$ transitions since they may be useful for high-precision measurements of parity non-conservation (PNC) [129] and could be used for an exchange of orbital angular momentum between light and the internal states of the atom [123, 130]. There are significant studies on the $6S_{1/2}$ to $5D_{5/2}$ transition in Cs at 685 nm using a variety of techniques including evanescent light fields from prism surfaces [128, 131], surface plasmons [132], and continuous wave (CW) free-space excitation [133], with proposals for using optical vortices [134], nano-edges [135], and plasmonics [132, 136].

Experiments in Rb have been more limited, with pulsed laser excitation of the $5S_{1/2}$ to the $4D$ levels at 516.6 nm [137, 138] and from the $5S_{1/2}$ to nD, where $n = 27 - 59$ Rydberg levels using a pulsed excitation at $\sim$ 297 nm wavelength [139] having been reported. Some works have also focussed on $n_1^2P \rightarrow n_2^2P$ electric quadrupole transitions in Rb by exploiting double resonances [140, 141]. However, for the reasons mentioned earlier, our focus is primarily on the $S \rightarrow D$ quadrupole transitions. The difficulty in exciting the $5S_{1/2} \rightarrow 4D$ transitions lies in the fact that the ratio of E1 to E2

transitions in the visible region is of the order of 10^7, so aside from the desirability of a strong electric field gradient, sufficient laser intensity at ~ 516.6 nm is needed to drive the transition, with the cross-section for absorbing one photon being 1.4×10^{-17} cm^2 [137]. The rapid radial exponential decay of the 516.6 nm evanescent field from the surface of the ONF provides a very steep electric field gradient in the region of highest field intensity even for very low excitation laser powers, leading to relatively efficient excitation of the E2 transition.

4.2 Enhancement of the Quadrupole Transition

Previously, Le Kien et al. [123] theoretically studied the E2 interaction of an alkali-metal atom with guided light in the fundamental and higher-order modes of an ONF. They showed that the E2 Rabi frequency and the E2 oscillator strength are enhanced due to the gradient of the field amplitude in fiber mode. The enhancement was expressed in terms of an enhancement factor, $\eta_{\rm osc}$, which is the ratio of the oscillator strength of a fiber-guided field to the oscillator strength for a free-space, plane wave of the same intensity. Using Cartesian coordinates (x_1, x_2, x_3), $\eta_{\rm osc}$ is given by [123]

$$\eta_{\rm osc} = \frac{2}{k_0^2 |\mathcal{E}|^2} \sum_q \left| \sum_{ij} u_{ij}^{(q)} \frac{\partial \mathcal{E}_j}{\partial x_i} \right|^2, \tag{4.2}$$

where the matrices $u_{ij}^{(q)}$ with $q = -2, -1, 0, 1, 2$ are given in Appendix B, $i, j = 1, 2, 3$, $\mathcal{E}$ is the electric field amplitude with $\mathcal{E}_j$ components, and k_0 is the wave number associated with the atomic transition frequency. The enhancement depends only on the atomic transition frequency and the fiber geometry, and not on any characteristics of the internal atomic states. It is determined by the ratio between the gradients and the amplitude of the field at the atomic resonance. In Figure 4.1(a), the enhancement factor for the $5S_{1/2}(F = 2) \rightarrow 4D_{3/2}(F' = 3)$ transition is plotted as a function of atom position in the xy-plane (where the fiber axis is along z and 1 μW of 516.6 nm light is guided in the fundamental $\rm HE_{11}$ mode quasi-linearly polarized along x). We find a maximum enhancement factor for the oscillator strength, $\eta_{\rm osc} = 4.92$, for an atom located on the fiber surface and positioned along the x-axis.

The enhancement factor, however, is not easily measured experimentally since it is a comparison between the ONF-mediated E2 interaction and that in free-space for a specific intensity at a single point; it does not account for the exponential decay of the evanescent field. An experimentally useful and accessible parameter is the E2 Rabi frequency. Consider an alkali atom with a ground state $|g\rangle = |nFm_F\rangle$ and an excited state $|e\rangle = |n'F'm_{F'}\rangle$, where n is the principal quantum number, F is the total angular momentum quantum number of the atom and m_F is the magnetic quantum number. Then the E2 Rabi frequency, using Cartesian coordinates (x_1, x_2, x_3) is given as [124]

$$\Omega_{FM_FF'M_{F'}} = \frac{1}{6\hbar} \sum_{ij} \langle n'F'M_{F'}|\mathcal{Q}_{ij}|nFM_F\rangle \frac{\partial \mathcal{E}_j}{\partial x_i}, \tag{4.3}$$

where the $\mathcal{Q}_{ij}$ are the quadrupole tensor components representing the strength of the

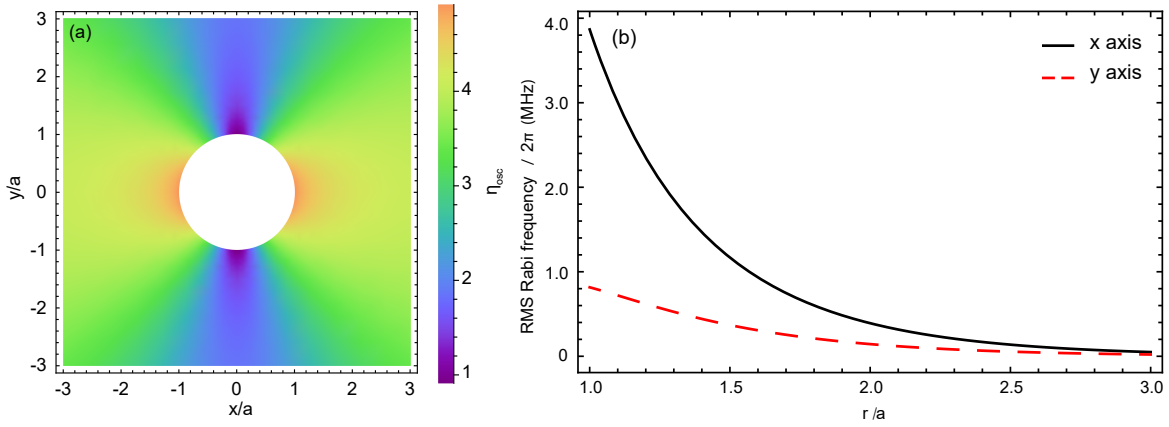

Figure 4.1: Theoretical values of (a) quadrupole oscillator strength enhancement factor η_{osc} and (b) the RMS quadrupole Rabi frequency for atoms positioned along the x-axis (solid line) or y-axis (dashed line), calculated for the $5S_{1/2}(F = 2) \rightarrow 4D_{3/2}(F' = 3)$ transition in ^{87}Rb for 1 μW of 516.6 nm light propagating in the HE_{11} mode of a 400 nm diameter ONF, with quasi-linear polarisation along the x-axis. Plotted by Dr. J.L. Everett.

quadrupole transition. The $\mathcal{Q}_{ij}$ are defined by [124]

$$\mathcal{Q}_{ij} = e(3x_i x_j - R^2\delta_{ij}). \tag{4.4}$$

Here, e is the electron charge, x_i is the i^{th} coordinate of the valence electron of the atom and $R = \sqrt{x_1^2 + x_2^2 + x_3^2}$ is the distance from the valence electron to the center-of-mass of the atom.

It is possible to define the root-mean-square (RMS) E2 Rabi frequency, $\bar{\Omega}_{FF'}$, determined from Equation 4.3 by summing over all the possible m_F, $m_{F'}$ values [142]

$$\bar{\Omega}^2_{FF'} = \sum_{M_F M_{F'}} |\Omega_{FM_F F'M_{F'}}|^2. \tag{4.5}$$

Figure 4.1(b) shows a plot of the RMS E2 Rabi frequency as a function of radial distance from the ONF surface for atoms interacting with the evanescent field of the HE_{11} mode. The RMS Rabi frequency is enhanced when atoms are positioned along the direction of polarization of the quasi-linear HE_{11} mode, i.e., the x-axis (as shown in black), where we have considered the fiber axis along z. While the E2 RMS Rabi frequency reduces rapidly with radial distance from the fiber, the E2 oscillator strength varies slowly and can be significant even at appreciable distances from the fiber surface. The E2 oscillator strength $f_{FF'}$ can be calculated from the RMS E2 Rabi frequency using the relation [142]

$$\bar{\Omega}^2_{FF'} = \frac{e^2|\mathcal{E}|^2}{2\hbar m_e \omega_0}(2F + 1)\, f_{FF'}, \tag{4.6}$$

where m_e is the mass of an electron, $\mathcal{E}$ is the electric field amplitude and ω_0 is the

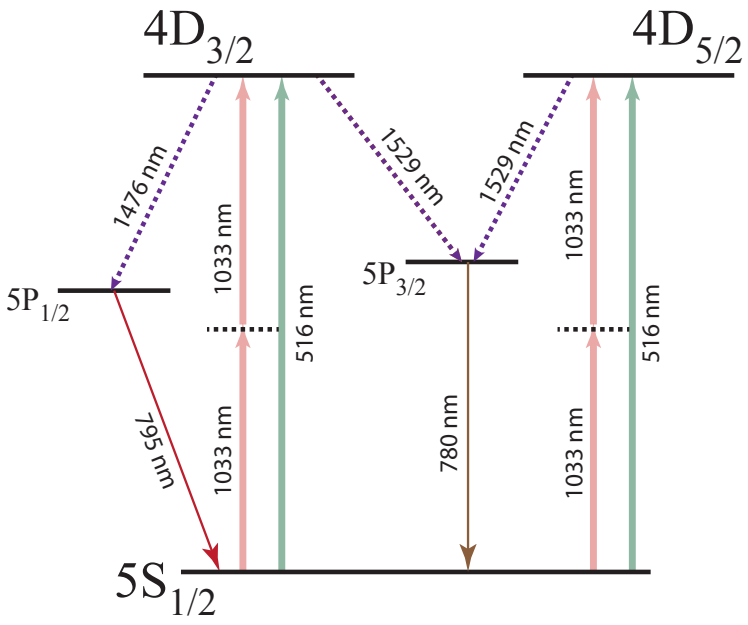

Figure 4.2: Energy level diagram of the 516.6 nm electric quadrupole excitation in ^{87}Rb and subsequent decay channels. A two-photon transition at 1033 nm is used as a frequency reference. The dashed black lines represents a virtual energy level.

atomic transition frequency from the ground state $|g\rangle$ to the excited state $|e\rangle$.

4.3 Observation of the $5S_{1/2}\rightarrow 4D_{3/2}$ Quadrupole Transition

The relevant energy level diagram for the 516.6 nm electric quadrupole transition in ^{87}Rb is shown in Figure 4.2. Atoms excited to the $4D_{5/2}$ state can decay back to the ground state via the $5P_{3/2}$ intermediate state and those excited to the $4D_{3/2}$ state can decay back via two channels, either the $5P_{3/2}$ or the $5P_{1/2}$ intermediate state. The decay through the $5P_{3/2}$ state is accompanied with a cascaded emission of two photons at 1529 nm and 780 nm [143, 144], while that through the $5P_{1/2}$ state is accompanied with a cascaded emission at 1476 nm and 795 nm. Detection of either of the emitted photon pairs would allow us to infer the E2 excitation. We detected 795 nm due to the availability of single photon detectors (SPD) at NIR wavelengths and its spectral separability from the 780 nm photons scattered during the atom cooling process. The first step in the decay path at 1476 nm was undetected, as we did not have an efficient detector in far-IR at the time. We drove the $5S_{1/2} \rightarrow 4D_{3/2}$ E1 forbidden, E2 allowed optical transition in our cold atomic ensemble of ^{87}Rb, via the evanescent field of an ONF. The emitted photons coupled into the ONF and could be detected at the output pigtail. A schematic of the experimental setup is illustrated in Figure 4.3.

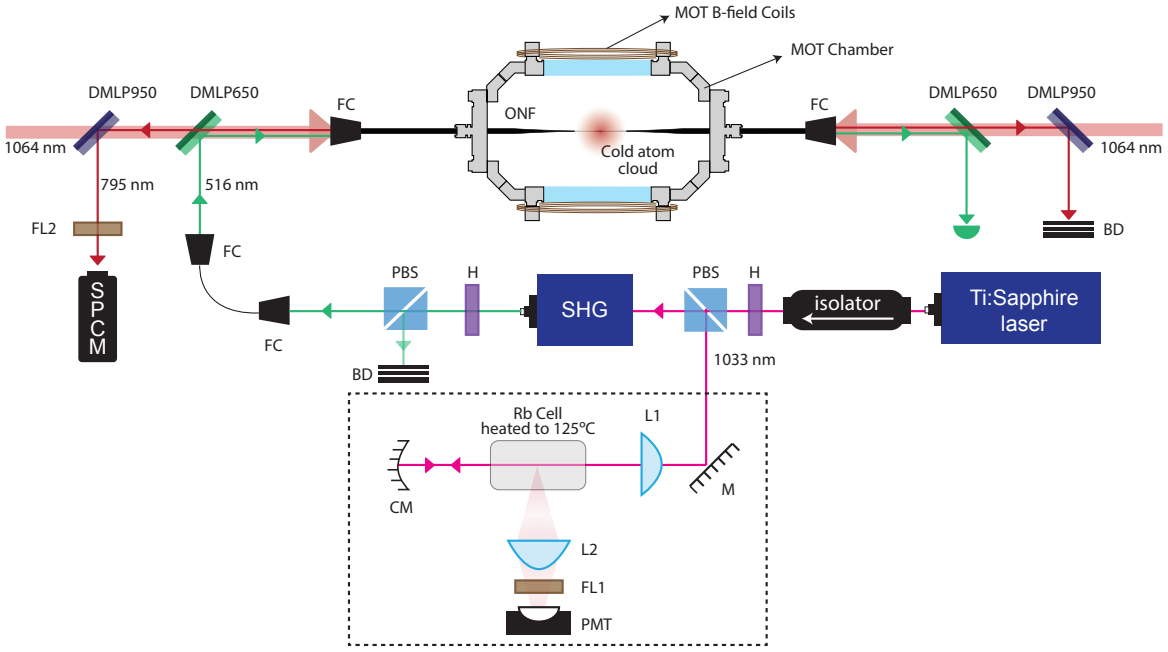

Figure 4.3: Schematic of the experimental setup. BD: Beam dump, CM: Concave mirror, D: Photodiode for visible wavelengths, DMLP650: Longpass dichroic mirror at 650 nm, DMLP950: Longpass dichroic mirror at 950 nm, FC: Fiber coupler, FL1: 800 nm shortpass filter, FL2: 795 nm narrow bandpass filter, H: Half-wave plate, L1,L2: Plano-convex lenses, M: Mirror, PBS: Polarizing beam splitter, SHG: Second harmonic generator, SPCM: Single photon counting module.

4.3.1 Frequency reference using two-photon spectroscopy

A frequency reference for the quadrupole transition was obtained using free-space, two-photon spectroscopy in a Rb vapor cell (with Rb gas at natural abundance) heated to 125°C [145]. We used a 1033.3 nm output from a Ti:Sapphire laser (M Squared SolsTis) to drive the corresponding two-photon transition (see Figure 4.2). The laser was frequency locked to a scanning reference cavity yielding a spectral linewidth of 50 kHz, and could be scanned by scanning the length of the cavity. Two-photon transitions are an attractive tool enabling Doppler-free spectra without the need of laser cooling. Two-photon transitions are discussed in Chapter 5.

The spectroscopy setup is shown in Figure 4.3. The 1033.3 nm direct output from the Ti:Sapphire was focused into a heated Rb vapor cell using a plano-convex lens (L1, $f = 150$ mm) and was then retro-reflected by a concave mirror (CM, $f = -75$ mm) placed at a distance 150 mm away from L1. A combination of a HWP and a PBS was used to control the power of the 1033.3 nm pump beam. The emitted 780 nm and 795 nm fluorescence was collected using a plano-convex lense (L2, $f = 50$ mm) and detected by a PMT (Hamamatsu R636-10) in conjugation with an optical short-pass filter (FL, Thorlabs FES0800). The quantum efficiencies of the PMT at 780 nm and 795 nm are 0.09 and 0.08, respectively. The obtained signal was amplified with a low-noise pre-amplifier (SR560, Stanford Research Systems) with a gain of 10^5. The laser was scanned around 1033.3 nm such that atoms are excited to the $4D_{3/2}F'$ level.

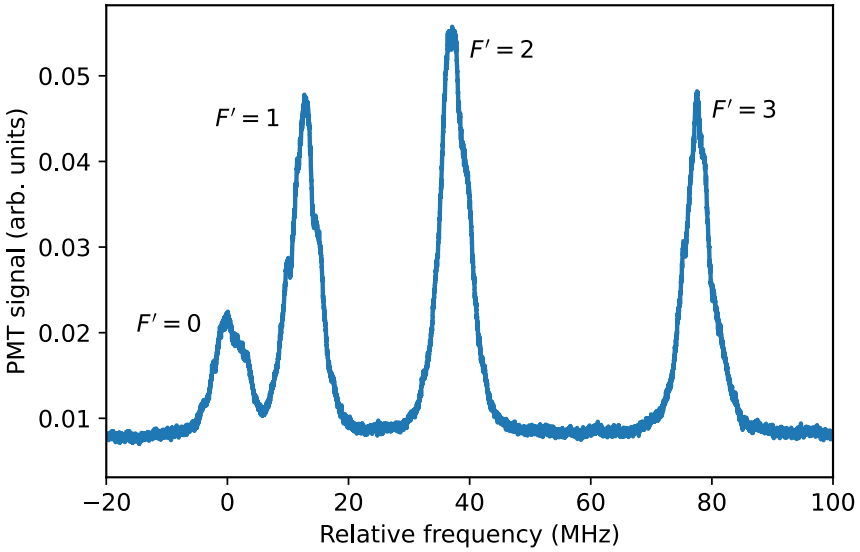

Figure 4.4: Vapor cell spectroscopy for the $5S_{1/2}(F = 2)$ to the excited states $4D_{3/2}(F')$ using free-space two-photon excitation at 1033.3 nm. The frequency is relative to the $F = 2 \rightarrow F' = 0$ transition peak and the frequency scale is used as half the atomic transition frequencies, calibrated for 1033 nm light frequency.

Figure 4.4 shows the two-photon spectroscopy signal for the $5S_{1/2}(F = 2) \rightarrow 4D_{3/2}(F')$ transitions. The four observed peaks correspond to the allowed transitions for the two-photon excitation at 1033.3 nm ($\Delta F = 0, \pm 1, \pm 2$) [146].

4.3.2 Quadrupole excitation in the cold atom-ONF system

To study the quadrupole transition, we cooled and trapped ^{87}Rb in the MOT and arranged it so that the ONF passed through the center of the cold atom cloud. A good overlap of the atom cloud with the ONF was ensured by observing the fluorescence coupled into the ONF. The Gaussian FWHM size of the atom cloud was measured to be ∼0.5 mm and the cloud temperature was measured to be about ∼120 µK, using the method described in Section 3.1.4. A 1064 nm beam was coupled into both ends of the ONF throughout the experiment (see Section 3.2).

The 516.6 nm light used to drive the transition was derived from the Ti:Sapphire laser used for the frequency reference through a frequency-doubling module (ECD-X second harmonic generator). The output from the second harmonic generator (SHG) was mode cleaned using a single-mode fiber and was coupled to one pigtail of the ONF using a dichroic mirror (Thorlabs, FEL0600), see Figure 4.3. Shortpass filters (Thorlabs FES0650) were placed after the SHG to remove any residual 1033.3 nm light, which could lead to two-photon excitation of the transition of interest. We controlled the 516.6 nm power through the ONF using a half-wave plate combined with a polarizing beam splitter (PBS) and neutral density filters (NDF). Only 10% of the 516.6 nm light input was detected at the output and we assumed it to be the same as its power at the

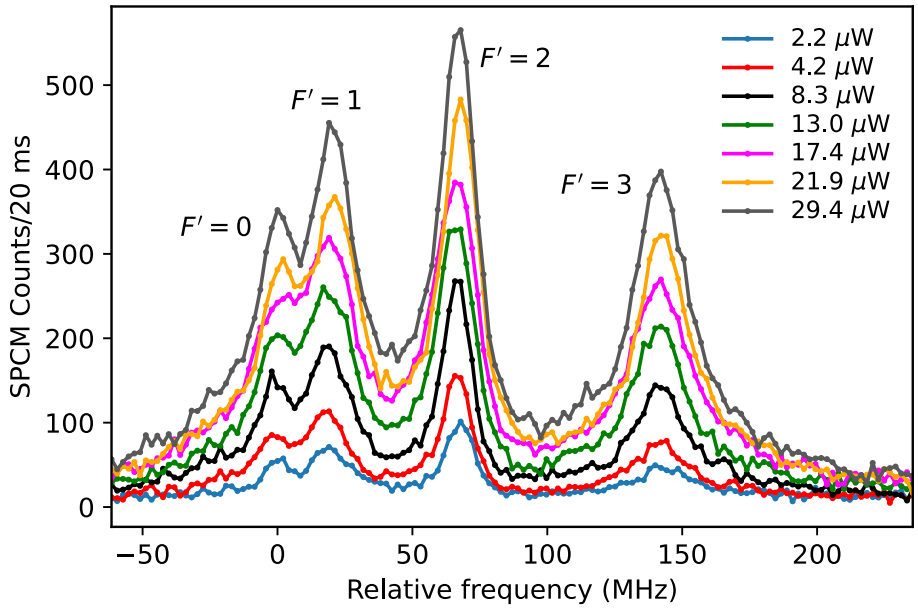

Figure 4.5: Spectroscopy signal for the $5S_{1/2}(F = 2) \rightarrow 4D_{3/2}(F')$ quadrupole transition in ^{87}Rb. The photon counts for emitted 795 nm emitted photons measured at the SPCM as a function of 516.6 nm pump frequency, for different powers in the ONF. The frequency is relative to the $F = 2 \rightarrow F' = 0$ transition peak.

ONF waist.

The experiment was performed by scanning the Ti:Sapphire laser frequency across the $5S_{1/2}(F = 2) \rightarrow 4D_{3/2}(F')$ transitions (see Figure 4.2) and recording the 795 nm decay photons generated from the ONF-mediated E2 transition on an SPCM conjugated with a 795 nm narrow bandpass filter. Simultaneously, we recorded the 1033.3 nm, two-photon spectroscopy signal from the vapor cell using a PMT. Each experiment cycle was 10 s long, with 20 ms bin time both for the SPCM and the PMT. Each data point was an average of 50 cycles. We could also detect the transmission of the 516.6 nm light through the ONF using a photodiode (PD) if desired.

4.3.3 Results

We studied the dependence of the 795 nm emission on the 516.6 nm power propagating through the nanofiber, see Figure 4.5. The four observed peaks correspond to the electric quadrupole transitions, $\Delta F \leq 2$, which are comparable to the observed two-photon dipole spectroscopy signal at 1033.3 nm in Figure 4.4. Expected features, such as peak broadening and peak shifts due to the presence of the ONF, are visible in the spectra, with wide asymmetric tails which we attribute to the van der Waals interaction between the ONF and the atoms [43]. Due to the roughly exponential decay profile of the evanescent field, atoms experienced a varying 516.6 nm intensity as they were excited to the $4D_{3/2}$ state. We ignored this and assumed that the 795 nm emission into the fibre was produced by stationary atoms in a constant field with an effective quadrupole Rabi frequency Ω_{eff}. This frequency included the oscillator

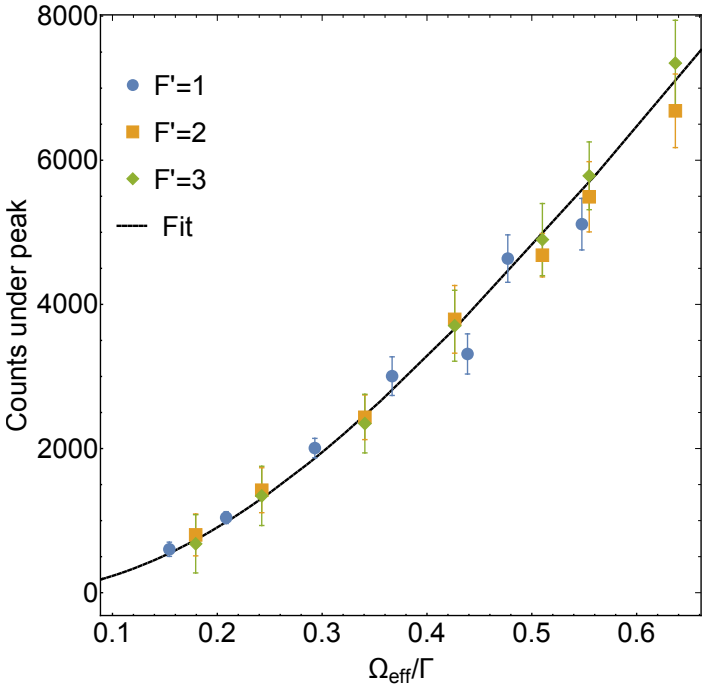

Figure 4.6: The photon counts under the quadrupole transition peaks in Figure 4.5 plotted against the 516.6 nm power propagating in the ONF, scaled to the fitted value of the estimated effective E2 Rabi frequency Ω_{eff}.

strength $f_{FF'}$ for each $F \rightarrow F'$ transition, so each F' level experienced a different Ω_{eff} for a specific propagating power in the ONF. We also ignored the pumping of atoms into particular M_F states by the cooling beams, as we expect this to be random and for the polarisation dependence to essentially average out over the length of the ONF. This allowed us to equate the RMS quadrupole Rabi frequency with the experimentally measured quadrupole Rabi frequency.

From Figure 4.5, we extracted Ω_{eff} for each power by modelling each F' transition as a broadened Lorentzian. We integrated the photon counts for each transition, with bounds set manually. The $F' = 0$ transition was discarded due to the large overlap that it had with $F' = 1$. Calculating the area under the peak, allowed us to disregard the exact source of the broadening. The integrated photon count was then related to the effective Rabi frequency by $A \propto \Omega_{\text{eff}}^2/\sqrt{\Gamma^2 + 2\Omega_{eff}^2}$, where $\Gamma/2\pi$ is the decay rate of the $4D_{3/2}$ state indirectly toward the ground state. In Figure 4.6 we fit the data to find $\Omega_{\text{eff}} = (0.12 \pm 0.02)\Gamma$ for 1 μW of propagating power, with the data plotted directly against the fitted value. Ignoring intermediate state lifetimes and the effect of the ONF on E1 transition rates, the dipole decay from the $4D_{3/2}$ state gives $\Gamma/2\pi = 2.12$ MHz, resulting in $\Omega_{\text{eff}}/2\pi = 250 \pm 50$ kHz for a power of 1 μW in the fibre. For comparison, the theoretically estimated value for the Rabi frequency (see Figure 4.1(b)), averaged over the azimuthal angle, is about 250 kHz for 1 μW of propagating optical power, 200 nm from the ONF surface. Since there is good qualitative agreement between the value predicted by theory and that measured experimentally by our alternate method, we can conclude that the 516.6 nm power at the waist should correspond roughly to

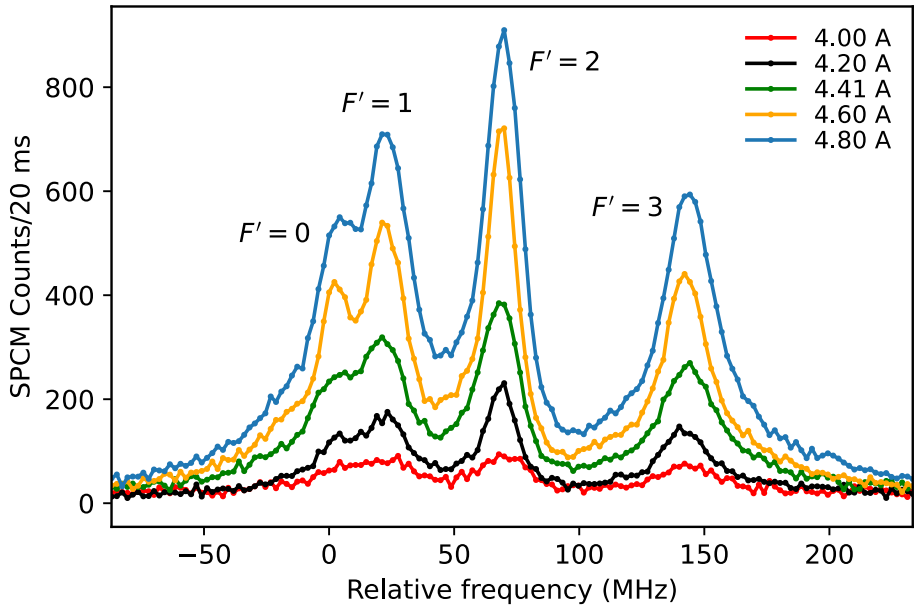

Figure 4.7: Spectroscopy signal for the $5S_{1/2}(F = 2) \rightarrow 4D_{3/2}(F')$ quadrupole transition in ^{87}Rb. The photon counts for emitted 795 nm photons measured at the SPCM as a function of 516.6 nm pump frequency, for different Rb getter currents. The frequency is relative to the $F = 2 \rightarrow F' = 0$ transition peak.

that measured at the output.

Subsequently, we studied the dependence of the 795 nm emission on the getter current to the Rb source. Results are shown in Figure 4.7. By assuming a Gaussian profile of the atom cloud, we estimated that a getter current of 4.0 A (4.8 A) corresponded to a density of $\sim 6 \times 10^9$ (8×10^9) cm^{-3}. Note, however, that the cloud shape changed dramatically during these measurements and as such it is more accurate to consider the number of atoms in the evanescent field increasing with getter current.

As a verification that the transition was E2 driven and not due to any 1033.3 nm leakage that may be driving a two-photon E1 transition, we used an AOM (DE-2503-3026, IntraAction Corp., central frequency: 250 MHz) set to a frequency of $\omega_{\mathrm{RF}} \sim 245$ MHz, to shift the SHG output light. Here, light from the SHG at 516.6 nm and any residual light at 1033.3 nm passed through the AOM and the positive first-order was sent through the ONF, in addition to the zeroth-order. The frequency of the light with respect to the SHG output was shifted by ω_{RF}. If the atoms were excited via the E2 transition at 516.6 nm, the spectroscopy signal peaks should shift by ω_{RF}, whereas if excitation was via the two-photon transition by residual light at 1033.3 nm, the peaks should shift by $2 \times \omega_{\mathrm{RF}}$. Observations showed, see Figure 4.8, that the signal was shifted by ω_{RF}; thence, the excitation was indeed via the E2 transition.

[2]The data was taken by Dr. V. Gokhroo.

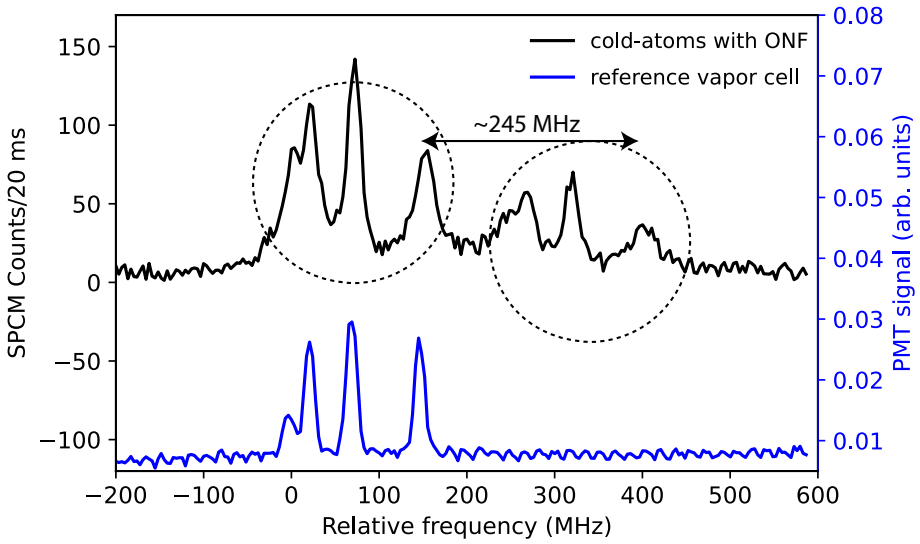

Figure 4.8: Spectroscopy signal[2] for the $5S_{1/2}(F = 2) \rightarrow 4D_{3/2}(F')$ quadrupole transition in ^{87}Rb. Quadrupole excitation in cold atoms when the SHG output is first passed through an AOM before being coupled to the ONF. The presence of the 1st order signal due to the AOM frequency shift, in the absense of a 2nd order signal, verifies the E2 transition. The frequency is relative to the $F = 2 \rightarrow F' = 0$ transition peak.

4.4 Conclusion

We demonstrated an ONF-mediated electric quadrupole transition, $5S_{1/2} \rightarrow 4D_{3/2}$, in ^{87}Rb at 516.6 nm [147], by recording fluorescence emissions at 795 nm. An important feature is that only a few μW of power were needed to drive the E2 transition. Even though the 1476 nm photon from the first step in the decay path was undetected in this work, it may be possible to indirectly determine the lifetime of the 4D level from the fluorescence distribution of the 795 nm [148] since the lifetime of the $5P_{1/2}$ is well-documented [149, 150].

The $5S_{1/2} \rightarrow 4D_{X/2}$ transition in ^{87}Rb could be used to study parity-violating nuclear forces beyond the standard model with the accuracy in Rb expected to be higher than that for Cs [129, 151] or could be exploited for the transfer of orbital angular momentum of light to the internal degrees of freedom of an atom. A similar technique to the work presented here could be used to study the $4D_{5/2}$ transition; this decays to the $5S_{1/2}$ state along a single path via the $5P_{3/2}$ state with the simultaneous emission of 1529 nm and 780 nm correlated photons. This work extends the use of ONFs in atomic systems and could find applications in fiber-based atomic clocks [152], lifetime measurements of atomic states, and in devising trapping schemes for neutral atoms.

Chapter 5

Polarization Dependence of a Single-Frequency Two-Photon Transition[1]

Previously it was described how the high intensity at low optical power levels and the exponential gradient features of the ONF can be exploited to achieve an efficient quadrupole excitation in a laser-cooled cloud of ^{87}Rb, see Chapter 4. The high intensity ($\sim 10^8$ mW/cm^2 on the surface for 1 mW of propagating optical power) of the guided mode in the ONF also facilitates two-photon interactions [50, 55] which, like electric quadrupole (E2) interactions, gives access to states with the same parity, such as electric dipole (E1) forbidden transitions [154]. ONF-mediated two-photon transitions at low power levels may be useful for fiber-based-optical switching [56, 155, 156], fiber-based compact atomic clocks [157] or fiber-integrated quantum logic gates based on the Zeno effect [158]. This chapter describes our study of the effect of the excitation field polarization on single-frequency two-photon transitions in ^{87}Rb atoms.

Here, we start by discussing some of the properties of a two-photon transition, in particular $S \rightarrow S$ transitions. This is followed by a discussion of the theoretical model of the two-photon transition in an atom as a function of polarization of the excitation light field, going beyond the limiting cases of purely linear or circular polarization. Finally, the results of our experiment, verifying the polarization dependence of the $5S_{1/2} \rightarrow 6S_{1/2}$ two-photon transition at 993 nm in ^{87}Rb atoms (see Figure 5.1) for two different excitation cases are presented: (i) warm atoms in a vapor cell with paraxial Gaussian beam illumination and (ii) laser-cooled atoms in the evanescent field of a single-mode ONF, where the light is strongly nonparaxial. For case (i), the two-photon transition rate scales proportionally with the squared degree of linear polarization, being zero for circularly polarized light. In contrast, for case (ii) the two-photon transition rate is not completely extinguished by varying the polarization.

[1]This chapter is adapted from the work published as K.S. Rajasree, R.K. Gupta, V. Gokhroo, F. Le Kien, T. Nieddu, T. Ray, S. Nic Chormaic and G. Tkachenko, "Spin selection in single-frequency two-photon excitation of alkali-metal atoms", Phys. Rev. Res. **2** (2020) 033341 [153]. RKG contributed by calculating the two-photon transition rate with the help of Dr. F. Le Kien, setting up the polarization compensation, performing the experiments with the vapor cell, and by participating in the writing of the research article.

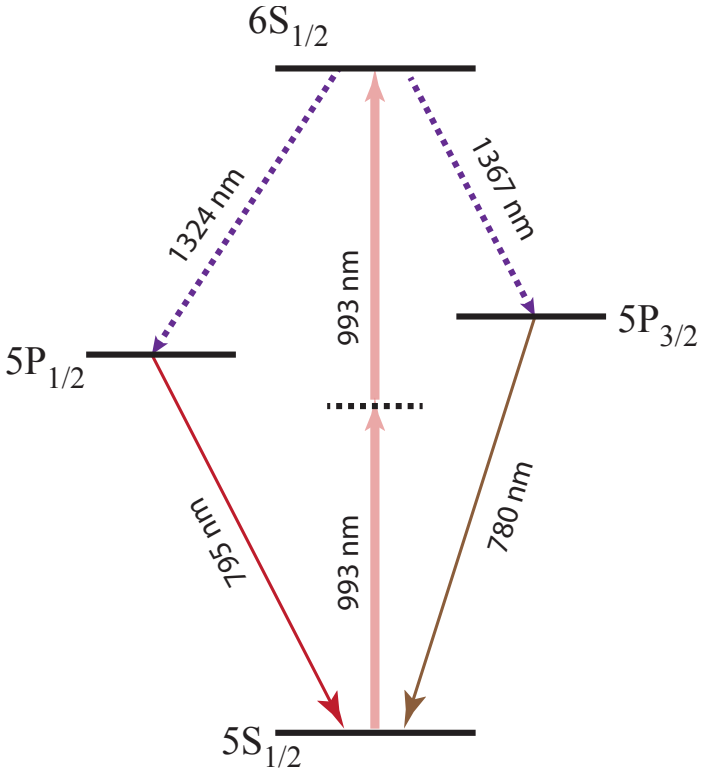

Figure 5.1: Energy level diagram relevant to the 993 nm two-photon transition in ^{87}Rb and subsequent decay channels. The horizontal dashed black line represents a virtual energy level.

5.1 S→S Two-Photon Transition

Two photon transitions in atoms can only occur between electron orbitals of the same parity. This leads to a selection rule for the allowed change of the orbital angular momentum of the electron: $\Delta L = 0, \pm 2$. In addition, the hyperfine levels involved in the transition obey a selection rule for the total angular momentum quantum number: $\Delta F = 0, \pm 1, \pm 2$ [146]. Here, we focus on an $S \rightarrow S$ transition where the intermediate level is detuned from the single-photon resonance frequency (see Figure 5.1). In this case, $\Delta F = 0$ and $\Delta m_F = 0$ (with m_F being the magnetic quantum number) [159], which means that the total spin of the atom must be conserved. If we assume that the spin of light is well-defined, conservation of angular momentum in the excitation process requires that the two photons must have mutually canceling spin projections along the quantization axis. This principle has been verified experimentally using sodium [160, 161] and rubidium [145, 162] vapor illuminated by counter-propagating Gaussian beams. Doppler-free transition peaks were observed when the beams had equal linear polarizations or opposite circular polarizations in the laboratory frame, but the peaks disappeared for circular polarizations of the same handedness.

When the excitation light is elliptically polarized, two-photon transitions are not completely absent, but occur at a rate that depends on the shape of the polarization

ellipse, as demonstrated experimentally [162]. It is important to note that in the aforementioned spectroscopy experiments, the atoms interacted with a paraxial, free-space light field only. In our case, we studied the atoms interacting with the evanescent field of an ONF, the polarization dependency for this case has not been studied before.

Two-photon transition frequencies for $S \rightarrow S$ transitions are insensitive to magnetic fields below the Paschen-Back regime[2] [163], while two-photon transitions to metastable states have extremely narrow linewidths (of the order of few kHz) compared to those for single-photon processes [164, 165]. These features make them a powerful tool for precision measurements [166, 167]. In the next section a model for this type of transitions is introduced in order to facilitate an understanding of the underlying physics relevant to the experimentally demonstrated polarization dependence of the two-photon transition.

5.2 Theoretical Model[3]

We consider an atomic transition from a ground state $|g\rangle$ to an excited state $|e\rangle$ (with corresponding angular frequency difference, $\omega_{eg} = \omega_e - \omega_g$), excited by the simultaneous absorption of photons from two light fields characterized by frequencies ω_1, ω_2, amplitudes $\mathcal{E}_1$, $\mathcal{E}_1$ and unit polarization vectors $\boldsymbol{\epsilon}_1$, $\boldsymbol{\epsilon}_2$ respectively. The rate of such a two-photon transition is given by [103]

$$P_{ge} = C\left|\frac{1}{\hbar}\sum_i \left(\frac{\langle e|\boldsymbol{\epsilon}_1\cdot\mathbf{d}|i\rangle\langle i|\boldsymbol{\epsilon}_2\cdot\mathbf{d}|g\rangle}{\omega_{ig}-\omega_2+i\Gamma_i/2} + \frac{\langle e|\boldsymbol{\epsilon}_2\cdot\mathbf{d}|i\rangle\langle i|\boldsymbol{\epsilon}_1\cdot\mathbf{d}|g\rangle}{\omega_{ig}-\omega_1+i\Gamma_i/2}\right)\right|^2, \tag{5.1}$$

with

$$C = \frac{1}{16\hbar^2}\frac{\Gamma}{(\omega_1+\omega_2-\omega_{eg})^2+(\Gamma/2)^2}|\mathcal{E}_1|^2|\mathcal{E}_2|^2, \tag{5.2}$$

where $\mathbf{d}$ is the atomic dipole operator, $|i\rangle$ is an intermediate state, $\omega_{ig} = \omega_i - \omega_g$ is the angular frequency difference between the states $|i\rangle$ and $|g\rangle$, $\Gamma = \Gamma_e + \Gamma_g$ is the sum of the decay rates of the upper and lower states, and Γ_e, Γ_g, and Γ_i are the natural linewidths of the states $|e\rangle$, $|g\rangle$, and $|i\rangle$, respectively. We find

$$P_{ge} = C|V_{eg}|^2, \tag{5.3}$$

where

$$V_{eg} = \sum_{K=0,1,2} V_{eg}^{(K)} \tag{5.4}$$

is the matrix element of the two-photon transition operator V_{eg} [100, 101], with the scalar ($K = 0$), vector ($K = 1$), and tensor ($K = 2$) parts given as (see Section 2.2 for

[2] The presence of a strong magnetic field causes decoupling of the total electronic momentum J and the nuclear spin momentum I.

[3] The model was developed in collaboration with Dr. F. Le Kien, Quantum Systems Unit, OIST.

the notation)

$$V_{eg}^{(K)} = (-1)^{K+I+J_e-m_g}\sqrt{(2F_e+1)(2F_g+1)}\begin{Bmatrix} F_e & K & F_g \\ J_g & I & J_e \end{Bmatrix}\alpha_J^{(K)} \times \sum_q \{\boldsymbol{\epsilon}_1 \otimes \boldsymbol{\epsilon}_2\}_{Kq}\begin{pmatrix} F_e & K & F_g \\ m_e & q & -m_g \end{pmatrix}. \tag{5.5}$$

where $q = 0, \pm 1$ describes the polarization in a spherical basis (see Section 2.2) and $\alpha_J^{(K)}$ are the reduced scalar ($K = 0$), vector ($K = 1$), and tensor ($K = 2$) two-photon susceptibility coefficients in the basis of the electronic angular momentum quantum number, J, and are given as

$$\alpha_J^{(K)} = (-1)^{K+J_e+J_g}\sqrt{2K+1}\sum_{n_iJ_i}\begin{Bmatrix} 1 & K & 1 \\ J_e & J_i & J_g \end{Bmatrix}\langle n_eJ_e\|\mathbf{d}\|n_iJ_i\rangle\langle n_iJ_i\|\mathbf{d}\|n_gJ_g\rangle \times \left[\frac{1}{\hbar(\omega_{n_iJ_i}-\omega_g-\omega_2+i\Gamma_i/2)} + \frac{(-1)^K}{\hbar(\omega_{n_iJ_i}-\omega_g-\omega_1+i\Gamma_i/2)}\right]. \tag{5.6}$$

The explicit expressions for the compound tensor components $\{\boldsymbol{A}\otimes\boldsymbol{B}\}_{Kq}$ which appear in Equation 5.5 are given in Appendix C. It is clear from Equation 5.6 that, in the particular case of equal photon frequencies with $\omega_1 = \omega_2$, we have $\alpha_J^{(1)} = 0$. In this case, the vector part $V_{eg}^{(1)}$ of the two-photon transition operator V_{eg} vanishes.

The general selection rule for the electronic angular momentum quantum number J is that the two-photon transition is allowed only if $|\Delta J| \leq 2$ [159, 168, 169]. Using Equation 5.6, the following rules can be stated:

- $\omega_1 = \omega_2$: the transitions $J_g = 0 \to J_e = 1$ and $J_g = 1 \to J_e = 0$ are forbidden [159].
- $J_e \neq J_g$: the Wigner 6-j symbol in Equation 5.6 for $K = 0$ is zero. This means that the coefficient $\alpha_J^{(0)}$ and the corresponding matrix element $V_{eg}^{(0)}$ vanish for $J_e \neq J_g$.
- $J_e = J_g = 0$ or $1/2$: the Wigner 6-j symbol in Equation 5.6 for $K = 2$ is zero. This means that the coefficient $\alpha_J^{(2)}$ and the corresponding matrix element $V_{eg}^{(2)}$ vanish for $J_e = J_g = 0$ or $1/2$.

The aforementioned selection rules for the electronic angular momentum, J, are equally true for the total angular momentum, F. However, depending on J, we may find additional selection rules for F. For instance, when $J_e = J_g = 0$ or $1/2$ and the photons have equal frequencies, we have the selection rules $F_e = F_g$ and $m_e = m_g$ [159].

The average transition rate for the transition between the hyperfine levels, F_g and F_e, is given by

$$P_{F_gF_e} = \frac{1}{2F_g+1}\sum_{m_gm_e} P_{ge}. \tag{5.7}$$

In the absence of a magnetic field, the level energies $\hbar\omega_g$ and $\hbar\omega_e$ do not depend on m_g and m_e, respectively. In this case, we find

$$P_{F_gF_e} = C(2F_e+1)\sum_K \begin{Bmatrix} F_e & K & F_g \\ J_g & I & J_e \end{Bmatrix}^2 \times \frac{|\alpha_J^{(K)}|^2}{2K+1}\sum_q |\{\boldsymbol{\epsilon}_1 \otimes \boldsymbol{\epsilon}_2\}_{Kq}|^2. \quad (5.8)$$

If $J_e = J_g = 0$ or $1/2$ and $\omega_1 = \omega_2$, the two-photon transition operator is scalar. In this case, the transition may occur only for $F_e = F_g$ and, hence, we find

$$P_{F_gF_e} = \frac{C}{3(2J_g+1)}|\alpha_J^{(0)}|^2|(\boldsymbol{\epsilon}_1 \cdot \boldsymbol{\epsilon}_2)|^2. \quad (5.9)$$

It is interesting to note that $P_{F_gF_e}$ does not depend on F_g. The line intensity, $I_{F_gF_e}$, is the product of the transition rate, $P_{F_gF_e}$, and the number of atoms in the initial state, $|n_gJ_gF_g\rangle$. If the hyperfine sublevels of the ground state are populated according to their degeneracy, the line intensity is $I_{F_gF_e} = P_{F_gF_e}N_0(2F_g+1)/[(2J_g+1)(2I+1)]$, where N_0 is the total number of atoms in the ground state. It is clear that $I_{F_gF_e}$ is proportional to $2F_g+1$ [159].

According to Equation 5.9, the dependence of the two-photon transition rate, $P_{F_gF_e}$, on the polarization of the excitation light field is determined by the factor $|(\boldsymbol{\epsilon}_1 \cdot \boldsymbol{\epsilon}_2)|^2$. The maximal value of this factor is one, achieved for two fields with identical linear polarizations or opposite circular polarizations with respect to the quantization axis, z (that is, opposite photon spin projections onto z). The minimal value of $|(\boldsymbol{\epsilon}_1 \cdot \boldsymbol{\epsilon}_2)|^2$ is zero and is achieved for two fields with orthogonal linear polarizations or identical circular polarizations with respect to z (identical photon spin projections onto z).

Equation 5.9 can be simplified further for the two-photon transition with $J_e = J_g = 1/2$, under excitation by two fields with identical frequencies $\omega_1 = \omega_2 - \omega_{eg}/2$, amplitudes $\mathcal{E}_1 = \mathcal{E}_2 = \mathcal{E}/\sqrt{2}$ and polarizations $\boldsymbol{\epsilon}_1 = \boldsymbol{\epsilon}_2 = \boldsymbol{\epsilon}$. The fields are either co-propagating (which we refer to as a one-beam configuration) or counter-propagating (a two-beam configuration). For such a single frequency, two-photon excitation, the transition rate is

$$P_{ge} = \frac{1}{96\hbar^2\Gamma}|\alpha_J^{(0)}|^2\mathcal{E}^4|(\boldsymbol{\epsilon}_1 \cdot \boldsymbol{\epsilon}_2)|^2. \quad (5.10)$$

5.2.1 Transition rate calculation for excitation by an ONF mode

Consider the excitation of a two-photon transition $J_g = 1/2 \rightarrow J_e = 1/2$ in a gas of atoms in the evanescent field of an ONF, in particular by an elliptically polarized fundamental HE_{11} mode propagating along $+z$ with the ONF axis aligned parallel to the z. The electric field of this mode is given by

$$\boldsymbol{\mathcal{E}} = (\sqrt{1+\sigma_h}\boldsymbol{\mathcal{E}}_{+1} + \sqrt{1-\sigma_h}\boldsymbol{\mathcal{E}}_{-1})/\sqrt{2}, \quad (5.11)$$

where $\sigma_h \in [-1, 1]$ is the helicity parameter[4] [170, 171] and

$$\boldsymbol{\mathcal{E}}_p = (e_r\hat{r} + pe_\varphi\hat{\varphi} + e_z\hat{z})e^{i(p\varphi+\beta z)}, \tag{5.12}$$

where $p = \pm 1$ is the polarization index for a quasicircularly polarized HE_{11} mode [172], β is the propagation constant, e_r, e_φ, and e_z are the reduced cylindrical components of the mode function which are independent of φ and z [114]. Equations 5.11 and 5.12 give

$$\begin{aligned}\mathcal{E}^2|(\boldsymbol{\epsilon}_1 \cdot \boldsymbol{\epsilon}_2)| = \boldsymbol{\mathcal{E}} \cdot \boldsymbol{\mathcal{E}} \;=\; & \left(\cos 2\varphi + i\sigma_h \sin 2\varphi + \sqrt{1-\sigma_h^2}\right)\left(e_r^2 + e_z^2\right) e^{2i\beta z} \\ & + \left(\cos 2\varphi + i\sigma_h \sin 2\varphi - \sqrt{1-\sigma_h^2}\right) e_\varphi^2 e^{2i\beta z}.\end{aligned} \tag{5.13}$$

The mode function components have the properties $e_r^2 = -|e_r|^2$, $e_\varphi^2 = |e_\varphi|^2$, and $e_z^2 = |e_z|^2$ [113, 114]. The average two-photon transition rate in an atom cloud for excitation by a HE_{11} mode can then be calculated from Equations 5.10 and 5.13, and by statistically averaging Equation 5.13 over the volume of the cloud interacting with the evanescent field. This gives

$$\bar{P}_{ge} \propto \bar{\xi} = A - \sigma_h^2 B, \tag{5.14}$$

where

$$\begin{aligned} A =& \langle (|e_r|^2 + |e_\varphi|^2 - |e_z|^2)^2 \rangle_r \\ & + 0.5 \left\langle (|e_r|^2 - |e_\varphi|^2 - |e_z|^2)^2 \right\rangle_r , \\ B =& \langle (|e_r|^2 + |e_\varphi|^2 - |e_z|^2)^2{}_r \rangle \\ & - 0.5 \left\langle (|e_r|^2 - |e_\varphi|^2 - |e_z|^2)^2 \right\rangle_r , \end{aligned} \tag{5.15}$$

with $\langle \cdots \rangle_r$ denoting statistical averaging over the radial distance, r, from the ONF surface. For this we have neglected the interaction of and collision between the atoms and have assumed that the atoms have a uniform stochastic distribution of position in the cloud. The proportionality equation (Equation 5.14) predicts that the transition rate is maximum for linearly polarized ($\sigma_h = 0$) and minimum (but, in general, nonzero) for quasi-circularly polarized ($\sigma_h = \pm 1$) excitation field modes. Equation 5.14 is true for a general field mode. For a paraxial Gaussian field, $e_z = 0$ and $|e_r| = |e_\varphi|$ thereby reducing the average single-frequency two-photon transition rate to

$$\bar{P}_{ge} \propto 1 - \sigma_h^2. \tag{5.16}$$

[4] The degree of circular polarization.

5.3 Single-Frequency Two-Photon $5S_{1/2}$→$6S_{1/2}$ Transition at 993 nm in ^{87}Rb

In order to verify the above theoretical result experimentally, we chose the $5S_{1/2}(F = 2) \rightarrow 6S_{1/2}(F' = 2)$ transition in ^{87}Rb, accessible via a two-photon excitation at 993 nm. The relevant energy level diagram is shown in Figure 5.1. The 993 nm light used to drive the transition was derived from a Ti:Sapphire laser (M Squared SolsTis), where the frequency was stabilised using a reference cavity and monitored using a wavelength meter (HighFinesse, WS-6). The 993 nm output from the Ti:Sapphire laser was split into two: one was sent to a warm vapor cell containing a mixture of ^{87}Rb and ^{85}Rb in their natural abundances and the other was coupled to the ONF (see Figure 5.2). Atoms excited to the $6S_{1/2}$ state can decay back to the $5S_{1/2}$ through two channels either through the $5P_{3/2}$ intermediate state emitting 1367 nm and 780 nm photons or through the $5P_{1/2}$ intermediate state emitting 1324 nm and 795 nm photons (see Figure 5.1).

5.3.1 Experiment: Warm atoms excited by a Gaussian beam

A schematic of the experiment is given in Figure 5.2. This experiment uses only the dashed part of the whole experimental setup. A 150 mW 993 nm laser beam was weakly focused into the warm vapor cell, maintained at 130°C, by a plano-convex lens (L1, f=150 mm) and was retro-reflected by a concave mirror (CM, f=−75 mm) placed at a distance 150 mm from L1. We had a one-beam configuration when the retro-reflected beam was blocked, otherwise it was a two-beam configuration. The 780 nm and 795 nm fluorescence emitted around the focal point of L1 was detected by a PMT through a relay telescope assembly made from plano-convex lenses (L2,L3, f=50 mm) in conjugation with a shortpass filter (Thorlabs FESH0800). The fluorescence intensity is a measure of the two-photon transition rate. A typical spectroscopy signal obtained by scanning the 993 nm frequency over the range of 3 GHz for horizontol polarization of the 993 nm input to the ONF is shown in Figure 5.3. The Doppler-broadened spectrum (top panel) was obtained for the one-beam configuration, whereas the spectrum showed a Doppler-free hyperfine spectrum (bottom panel) for the two-beam configuration.

Next, we reduced our frequency scan range to only scan around the $F = 2 \rightarrow F' = 2$ transition in ^{87}Rb. We introduced a QWP (Q1) before L1 and scanned the helicity parameter σ_h over the whole $[-1, 1]$ range by varying θ, the angle between x and the slow axis of the waveplate. As a result, the initial horizontal polarization state was transformed into $\mathbf{s}_{\text{in}} = (1, \cos^2 2\theta, \sin 2\theta \cos 2\theta, -\sin 2\theta)$, where $\mathbf{s}_{\text{in}}$ is the reduced Stokes vector[5] defined from the point of view of the receiver. Figure 5.4 shows the measured polarization of the beam shown on the Poincaré sphere, as Q1 was rotated. The helicity parameter was given by $\sigma_h = \sin 2\theta$. For this case, the two-photon transition rate was expected to scale as $\cos^2 2\theta$ (see Equation 5.16), as confirmed by the measured polarization dependence of the fluorescence signal (see Figure 5.5). The fluorescence signal in the one-beam configuration was simply the mean voltage output of the PMT.

[5]For a reduced Stokes vector $\mathbf{s} = (1, S_1, S_2, S_3)$, S_i for $i = 1, 2, 3$ are the reduced Stokes parameters quantifying the horizontol, diagonal, and circular components of the polarization, respectively.

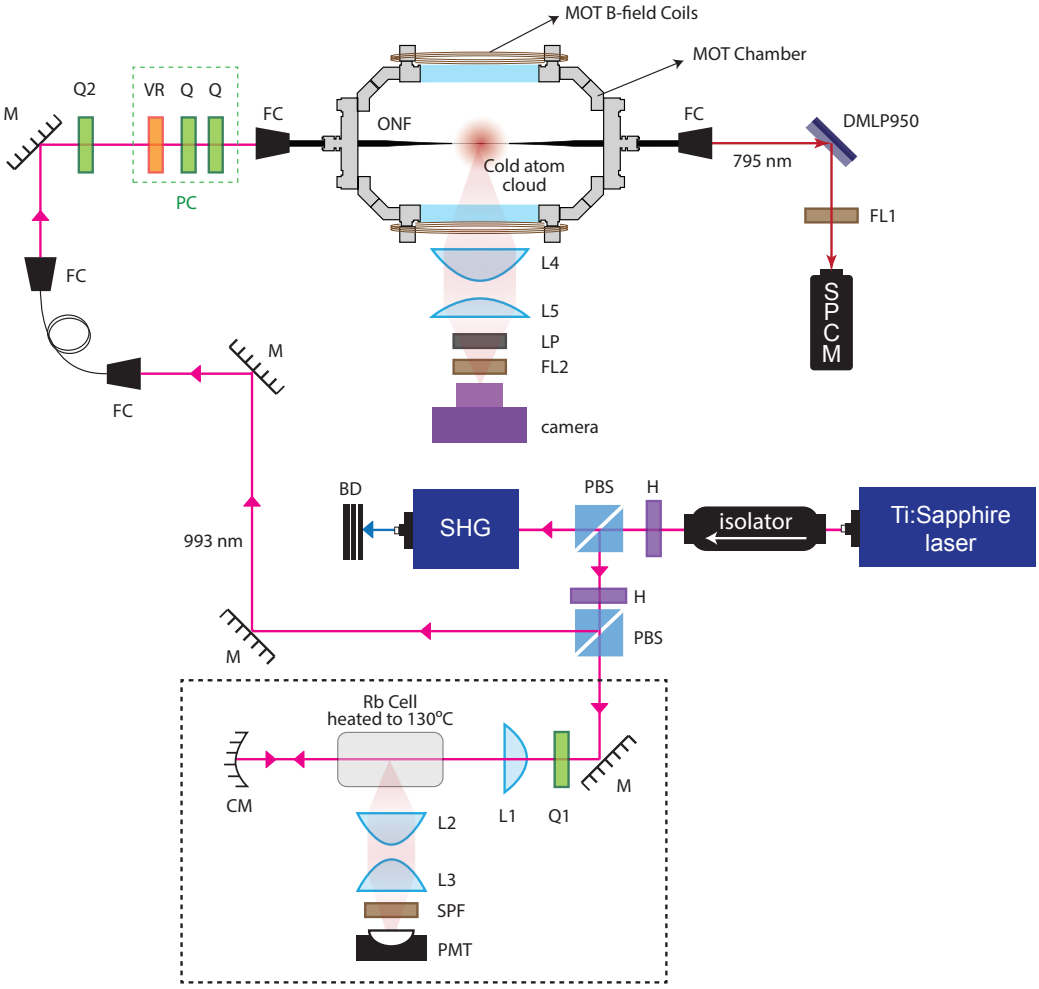

Figure 5.2: Schematic of the experimental setup. BD: Beam dump, CM: Concave mirror, FC: Fiber coupler, FL1: Narrow bandpass filter at 795 nm, FL2: Narrow bandpass filter at 990 nm, H: Half-wave plate, L1,L2,L3,L4,L5: Plano-convex lenses, LP: Linear polarizer, M: Mirror, PBS: Polarizing beam splitter, PC: Polarization compensator, Q1,Q2,Q: Quarter-wave plates for 993 nm light, SHG: Second harmonic generator, SPCM: Single photon counting module, SPF: Shortpass filter at 800 nm, VR: Variable retarder.

In the two-beam configuration, the maxima of the transition spectral profile fitted to a Lorentzian curve was averaged over ten independent measurements for each helicity input.

5.3.2 Experiment: Laser-cooled atoms excited by an ONF mode

A schematic of the experimental setup is shown in Figure 5.2. One arm of the 993 nm light output from the Ti:Sapphire was coupled into the ONF. Recall that the ONF diameter was ∼400 nm at the waist, thereby supporting only the fundamental HE_{11} mode for 780 nm, 795 nm and 993 nm light. The transmission of the coupled 993 nm

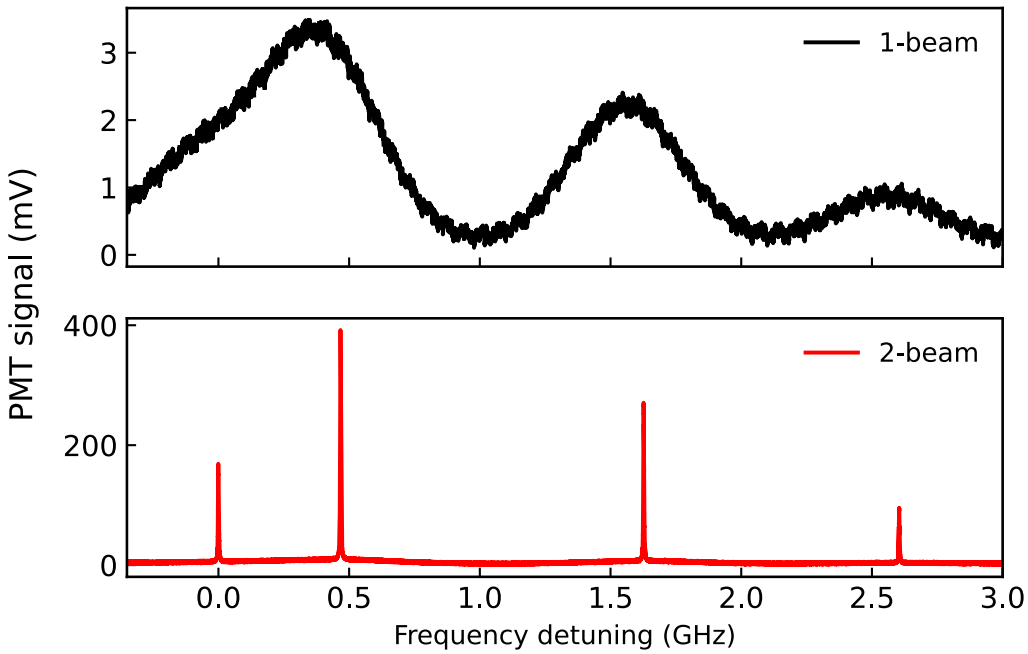

Figure 5.3: Typical Doppler-broadened (top) and Doppler-free (bottom) spectroscopy signals (background subtracted) of the $5S_{1/2} \rightarrow 6S_{1/2}$ two-photon transition in a warm vapor cell containing a mixture of ^{85}Rb and ^{87}Rb in their natural abundances, in one-beam and two-beam configurations respectively.

light through the ONF assembly was about 30% including the coupling losses, since the ONF was optimized for 780 nm propagation (see Section 3.2). In a similar fashion to the quadrupole experiment described in Chapter 4, we only detected fluorescence emitted at 795 nm because of its spectral separability from the 780 nm photons scattered during the atom cooling process.

The optical power of the 993 nm light coupled to the ONF was maintained at 0.6 mW as measured at the output end of the fiber. This high power of 993 nm through the ONF kept it hot and avoided atoms sticking on the surface. The 993 nm light was sent through the ONF for two hours prior to measurements in order to heat the ONF and reach a stable temperature. This is important as the temperature-induced birefringence causes fluctuations in the polarization of the guided mode. After two hours of heating, the polarization was stable to within 1° on the Poincaré sphere, as confimed by a free-space polarimeter (Thorlabs PAX1000IR) placed at the output end of the fiber.

Due to stress-induced birefringence in the tapered fiber, the preset input polarization state of the 993 nm ONF-guided light was transformed into an unknown state at the ONF waist. To study the polarization dependence on the transition rate, it was crucial to gain control over the polarization (helicity) at the waist. For this, we implemented[6] a polarization compensation (developed by Dr. G. Tkachenko [97] and described in Section 3.2.2) at the ONF input fiber coupler to match the polarization

[6]Dr. G. Tkachenko, Dr. K.S. Rajasree and RKG contributed equally to set this up.

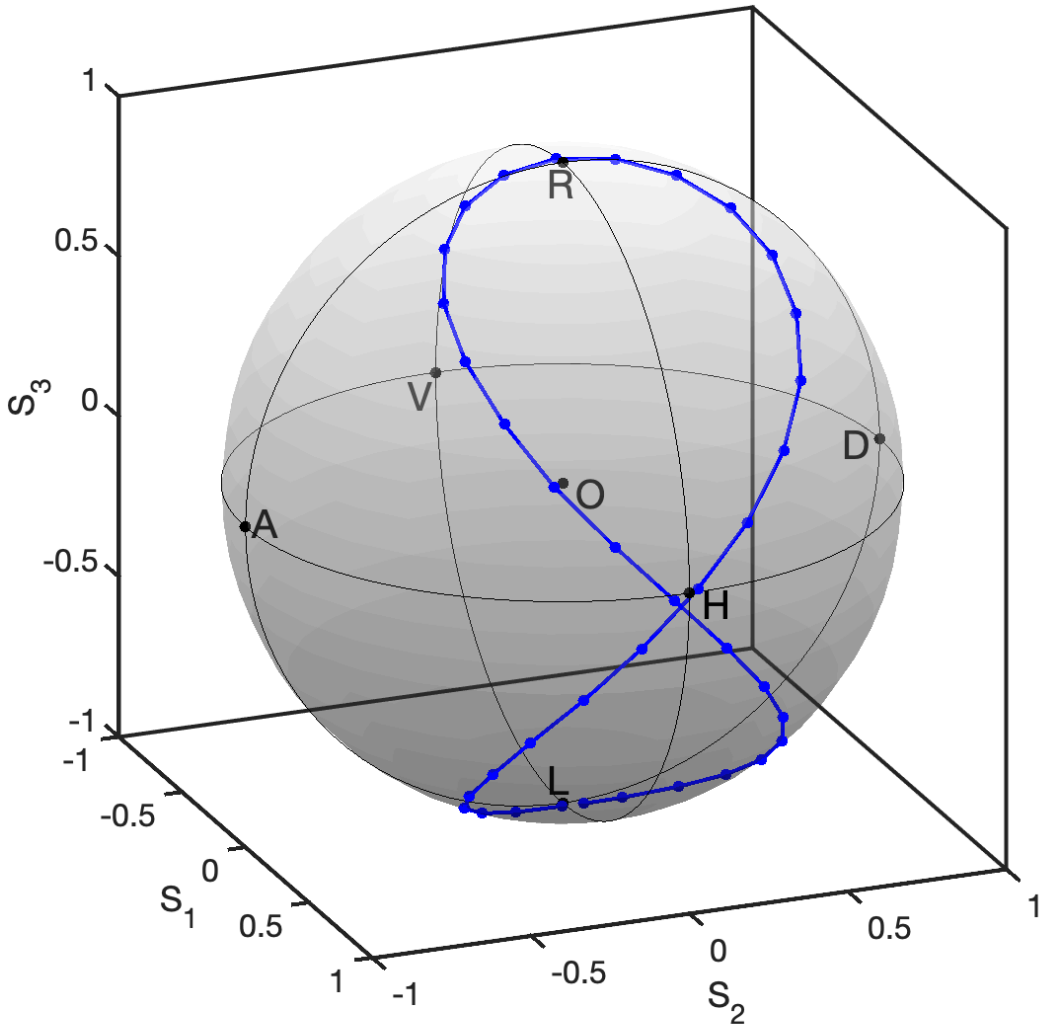

Figure 5.4: Measured polarization of the input 993 nm beam represented on the Poincaré sphere, in terms of the reduced Stokes parameters, as the QWP Q1 (Figure 5.2) is rotated from $\theta = 0$ to $\theta = -180°$.

state of 993 nm light at the ONF input to that at the ONF waist. A crucial component of the compensation is the identification of the polarization from Rayleigh imaging. The error in state identification was expected to be less than 10° on the Poincaré sphere [97]. When $|\sigma_h|$ approaches unity, this error corresponds to a confidence range of about 1.5% for $|\sigma_h|$ and 3% for σ_h^2. Once polarization compensation was achieved, a QWP Q2 was placed before the compensator to vary the helicity of the 993 nm at the ONF waist.

A cold cloud of ^{87}Rb atoms well-overlapped with the ONF was produced in a MOT. An average atom cloud density of 10^9 cm^{-3} and a temperature of 120 μK was estimated from fluorescence imaging by the method described in Section 3.1.4. In a typical experimental sequence[7], the helicity of the 993 nm was set by rotating Q2, the atom cloud was loaded to saturation and then the excitation laser was scanned ±40 MHz across the $5S_{1/2}(F = 2) \rightarrow 6S_{1/2}(F' = 2)$ transition in ^{87}Rb, while the

[7]The experiment with cold atoms was performed by Dr. K.S Rajasree.

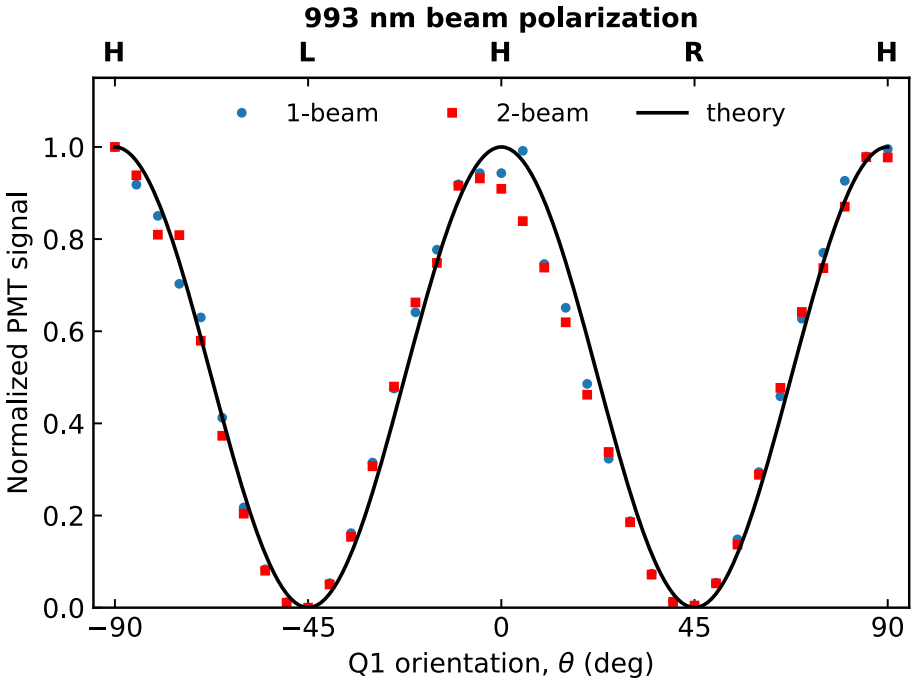

Figure 5.5: Polarization dependence of the fluorescence signal for the 993 nm two-photon transition in the vapor cell. Blue circles and red squares show the experimental data for one-beam and two-beam configurations. The principal polarization states of the 993 nm light are indicated: horizontal x-polarized (**H**), left-hand circular (**L**), and right-hand circular (**R**).

795 nm fluorescence coupled to the ONF was recorded by an SPCM through a narrow bandpass filter at 795 nm. The data was averaged over 40 experimental cycles for each Q2 orientation.

Figure 5.6 shows typical transition peaks for fluorescence at 795 nm in the two limiting cases, linearly polarized ($\sigma_h = 0$, $\bar{\xi}_0 = A$) and quasi-circularly polarized ($\sigma_h = \pm 1$, $\bar{\xi}_\pm = A - B$). Here, we have used the notation $\bar{\xi}$ introduced in Equation 5.14. Each set of data is fitted to a Lorentzian curve and its peak height is the measure of the two-photon transition rate. The peak height is plotted against Q2 orientation in Figure 5.7, where the solid curve is the calculated $\bar{\xi}/\bar{\xi}_0$. We attribute the discrepancy between the experimental data and the theoretical curve, specifically the shallower and narrower dips in the measurement, to several experimental factors beyond our control: the polarization compensation only works for the transverse field components, atoms are not necessarily evenly distributed around the ONF (as suggested by the atom cloud picture shown in the inset of Figure 5.2), individual atoms may see local inhomogeneities of the excitation field near the ONF waist, or residual magnetic field and cooling beams may be present in the excitation region, thereby influencing the two-photon process.

The lateral shift of the rising slopes seen in both periods of the θ dependence in Figure 5.7 is likely to be an experimental artefact such as imperfection of the waveplate, enhanced by coupling of light into the fiber. Other effects not taken into account are

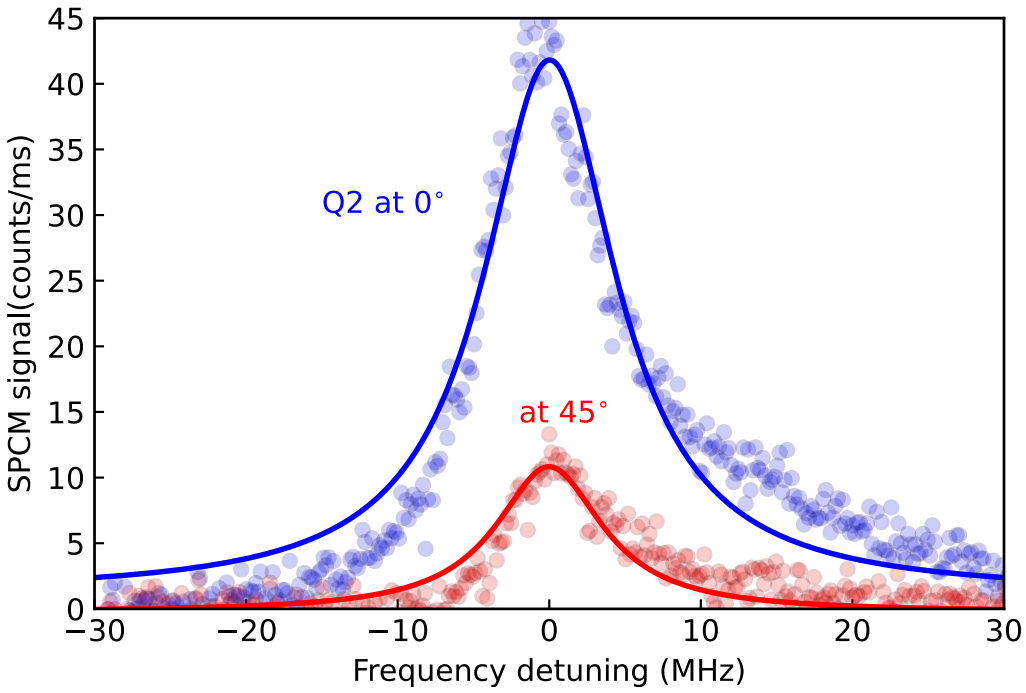

Figure 5.6: Measured 795 nm fluorescence from the cold atoms. Typical transition peaks for linearly polarized (Q2 at $\theta = 0°$ and $\sigma_h = 0$) and circularly polarized ($\theta = 45°$ and $\sigma_h = 1$) 993 nm light coupled into the ONF. The solid lines represent Lorentzian curve fitting.

possible polarization-dependent saturation [49] of the transition in the atomic cloud, a polarization-induced inhomogeneity in the intensity profile [173] and the related change in the local atomic density due to the dipole force, and position-dependent Stark shifts in the atomic energy levels [99]. We also note that the relation $\sigma_h = \sin(2\theta)$ may not be exactly fulfilled for ONF-mediated excitation. For instance, the generation of orbital angular momentum in the evanescent field, which is more significant for quasi-circular polarization [40, 171], effectively changes the helicity and its relation to the polarization of light sent into the fiber. This invites further studies on two-photon processes under nonparaxial fields, inclusive of the orbital degree of freedom.

5.4 Conclusion

We observed the dependence of an $S \to S$ single-frequency two-photon transition on the polarization of the excitation field, both within and beyond the paraxial limit. Owing to accurate polarization control of light at the ONF waist, we were able to study the transition rate in a cold atomic cloud mediated by the evanescent field of the ONF-guided mode, as a function of its helicity. In contrast to the paraxial case in a vapor cell, the two-photon transition in the evanescent field could not be extinguished by simply varying the polarization of the coupled light; we observe a minimum rate of about 25% of the maximum. The theoretical minimum is calculated to be around

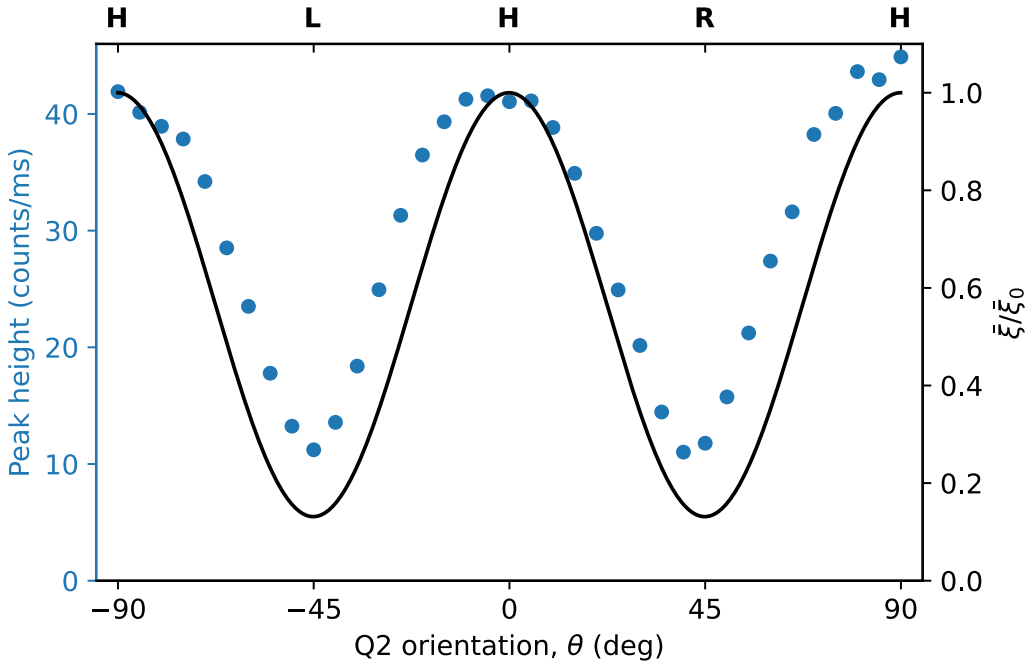

Figure 5.7: Polarization dependence of the 795 nm fluorescence from the cold atoms excited by a nanofiber mode. The solid line shows theoretical calculation.

13% of the maximum. These findings are expected to have impact in atom-based hybrid quantum technologies where full control on quantum state selection is vital and could open new ways of selecting transition pathways for frequency references and atomic clocks, novel fiber-based atom trapping schemes [28], transfer of spin or orbital angular momentum between light and atoms [130, 174], chiral nanophotonics [175], and fundamental precision tests in parity nonconservation [176, 177].

Chapter 6

Machine Learner Optimization of Nanofiber-Based Dipole Traps[1]

In Chapters 4 and 5, we discussed experiments related to cold atom cloud interacting with the evanescent field of a nanofiber. However, these experiments with the atom cloud suffer from two limiting factors. First, the atom density is reduced close to the ONF surface due to thermal heating, thus limiting the optical depth. Second, the atoms have a very short transit time ($\sim$1 μs for an average atom temperature of 100 μK) in the small evanescent field region, thus limiting the interaction time. A fiber-based evanescent field dipole trap can be used to hold cold atoms with longer trapping lifetimes exceeding tens of milliseconds while facilitating direct interrogation of the atoms and integration of the experimental platform into a fiber network. In this chapter, we describe an implementation of a two-color evanescent field trap for ^{87}Rb atoms in our ONF-MOT system and its optimization (in terms of the number of atoms trapped and optical depth) using a machine learning (ML) scheme.

In Chapter 1 we first discussed fiber-based dipole traps. In an uncompensated trap that is deep enough to trap laser-cooled Rb atoms from a MOT; a tens of MHz light shift broadens the absorption profile of a probe beam near-resonant to the cooling transition ($5S_{1/2} \rightarrow 5P_{3/2}$ for ^{87}Rb) and creates asymmetries in the observed spectra [96]. This makes it difficult to determine the number and temperature of trapped Rb atoms as the saturation absorption method [28] cannot be used, and dispersive methods [179] are much less effective. Real-time and manual optimization of the trap loading parameters is very time intensive, if not near impossible, in contrast to Cs [179]. Furthermore, optimization of the optical depth (OD) depends on both the number and temperature of the trapped atoms, rendering OD determination in real-time also very challenging [180].

With Rb atoms being one of the most widely used atomic species in cold atom-based quantum technologies, finding techniques to optimize their loading into ONF-based dipole traps is crucial. The aforementioned difficulty in measuring the number

[1]This chapter is adapted from the manuscript R. K. Gupta, J. L. Everett, A. D. Tranter, R. Henke, V. Gokhroo, P. K. Lam and S. Nic Chormaic, "Machine learner optimization of optical nanofiber-based dipole traps for cold ^{87}Rb atoms", arXiv preprint arXiv:2110.03931 (2021). RKG contributed to all aspects of the work including setting up and performing the experiment, adapting the python-based deep learning code [178] written by A. D. Tranter, developing the theoretical model in collaboration with J. L. Everett, and writing the manuscript.

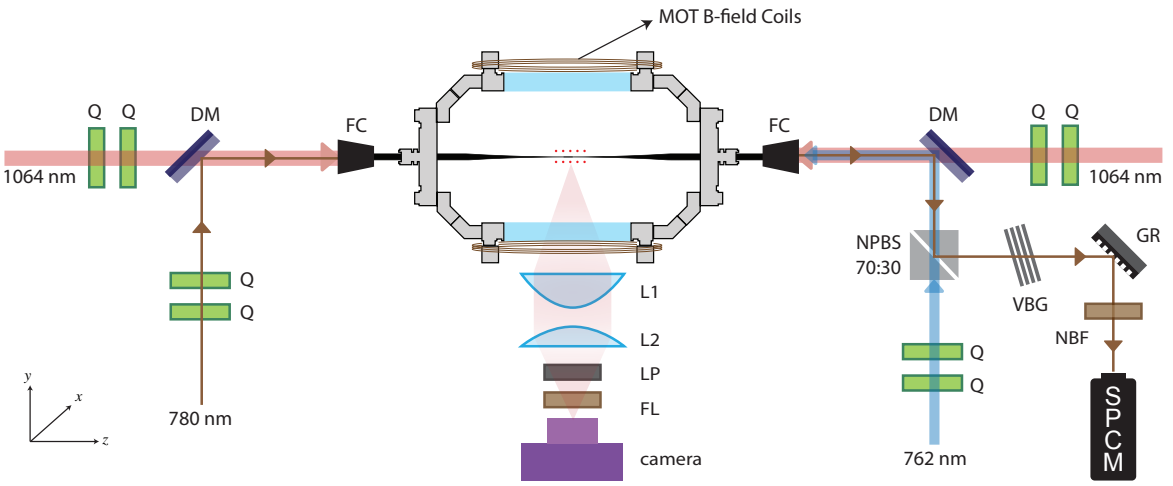

Figure 6.1: Schematic of the experimental setup for fiber-based dipole trapping of ^{87}Rb atoms. DM: DMLP950 Longpass dichroic mirror at 950 nm, FC: Fiber coupler, FL: Narrow bandpass optical filter, GR: Ruled grating, L1,L2: Plano-convex lenses, LP: Linear polarizer, NBF: Narrow bandpass filter at 780 nm, NPBS: Non-polarizing beam splitter, Q: Quarter-wave plates, VBG: Volume Bragg grating.

of trapped atoms in real-time renders optimization of the trapping sequence during an experiment essentially impossible if one tries to do this manually. Here, we present an application of a ML optimization protocol, based on deep learning, to the experimental control sequence for cooling atoms in a MOT and subsequently loading them into a fiber-based dipole trap.

6.1 Implementation of an Uncompensated Fiber Trap for ^{87}Rb

Our ONF-based two color optical dipole trap array was created using a combination of red- and blue-detuned beams relative to the cooling transition $5S_{1/2} \rightarrow 5P_{3/2}$ in ^{87}Rb. A schematic of the experimental setup is shown in Figure 6.1. We sent 1064 nm (red-detuned) light through an ONF in a counter-propagating configuration with 1.8 mW in one direction and 2.1 mW in the opposite direction. The difference in the powers is due to different losses in each of the taper regions. Additionally, 1.23 mW of 762 nm (blue-detuned) light was sent through the ONF along one direction. The resulting potential from a counter-propagating red-detuned and a traveling blue-detuned field configuration is of the form

$$U(r,\phi,z) = \frac{1}{4}\left[4\alpha(\omega_{red})|\mathcal{E}_{\text{red}}(r,\phi,z)|^2\cos^2(\beta_{\text{red}}z) + \alpha(\omega_{\text{blue}})|\mathcal{E}_{\text{blue}}(r,\phi,z)|^2\right], \quad (6.1)$$

where $\alpha(\omega_{\text{red}})$ and $\alpha(\omega_{\text{blue}})$ are the polarizabilities (see Section 2.2.2) of the ground state for the red- and the blue-detuned frequencies respectively, $\mathcal{E}_{\text{red}}$ and $\mathcal{E}_{\text{blue}}$ are the electric fields of the red- and the blue-detuned HE_{11} mode propagating in the ONF, and β_{red} is the propagation constant of the red-detuned HE_{11} mode. The relevant

field expression of a HE_{11} mode is given in Appendix A. The $\cos^2(\beta_{\text{red}} z)$ term gives a standing wave pattern, which creates the lattice array along the fiber axis. Note that the polarizabilities, in general, depend on the polarizations of the fields. The ground state potential and the shift of the optical transition energies of the cooling transition of ^{87}Rb atoms near the nanofiber are shown in Figure 6.2 for two configurations of the trapping fields: (i) a parallel-configuration, when the red- and blue-detuned trapping fields are quasi-linearly polarized parallel to each other, and (ii) a cross-configuration, when the fields are quasi-linearly polarized orthogonal to each other. While the cross-configuration results in stronger confinement, it requires higher power for the blue-detuned field. To generate Figure 6.2, we used double the power of blue (762 nm) light for the cross-configuration than for the parallel-configuration. Figure 6.3 shows the differential shift of the cooling transition for different $m_{F'}$ levels.

All the fiber-guided beams were quasi-linearly polarized along the x-axis using the method described in Section 3.2.2. The polarization compensator was simplified by removing variable retarders and only keeping a pair of QWPs for each beam. In the case when full polarization control is not required, mapping a linear input polarization to a quasi-linearly polarized HE_{11} mode in the fiber can be achieved by using only a pair of QWPs. For parallel-polarized red- and blue-detuned beams, we would expect the vector light shifts to be large, but this configuration reduced the amount of power needed in the blue-detuned beam [179]. The trapping fields were turned on for (at least) 2 hours to heat up the fiber before setting up the polarizations. The trapping fields were kept on at constant powers throughout the experiment in order to prevent thermal stresses from causing movement of the ONF, except during the *molasses-phase* when the 1064 nm laser power was slightly ramped away from and back to the set constant value. Note that we manually adjusted the polarization of each beam slightly to maximize the probe beam absorption (in other words, the number of atoms within the evanescent field region) prior to conducting any experiments.

Absorption measurement: Experimental sequence A weak probe beam (∼5 pW) near-resonant with the cooling transition $5S_{1/2}(F = 2) \rightarrow 5P_{3/2}(F' = 3)$ at 780 nm and also quasi-linearly polarized along the x-axis was sent through the ONF counter-propagating to the 762 nm light and was used to measure the absorption profiles using an in-fiber technique analogous to free-space absorption spectroscopy. In a typical experimental sequence (2 s duty-cycle, illustrated in Figure 6.4), which was computer-controlled via LabVIEW, the ^{87}Rb atoms were first laser-cooled in a MOT to saturation which we call the *MOT-phase* (∼1.6 s long). This was followed by a *sweep-phase* (∼200 ms), during which the cooling laser frequency was ramped down to a set value, determined manually. Following this, there was a *molasses-phase* during which the trapping magnetic fields were quickly switched off, the cooling laser frequency was ramped further away from the cooling transition, and the cooling and repump beam powers were ramped down. For finer control, the *molasses-phase* was divided in to two independent subperiods of variable durations and variable slopes of the ramps. The durations and the slopes were determined via the optimization process. The temperature of the atom cloud at the end of the *molasses-phase* was estimated, via the imaging method described in Section 3.1.4, to be ∼40 μK. The atoms were loaded into the fiber dipole trap array mainly during this *molasses-phase*. Once the dipole trap

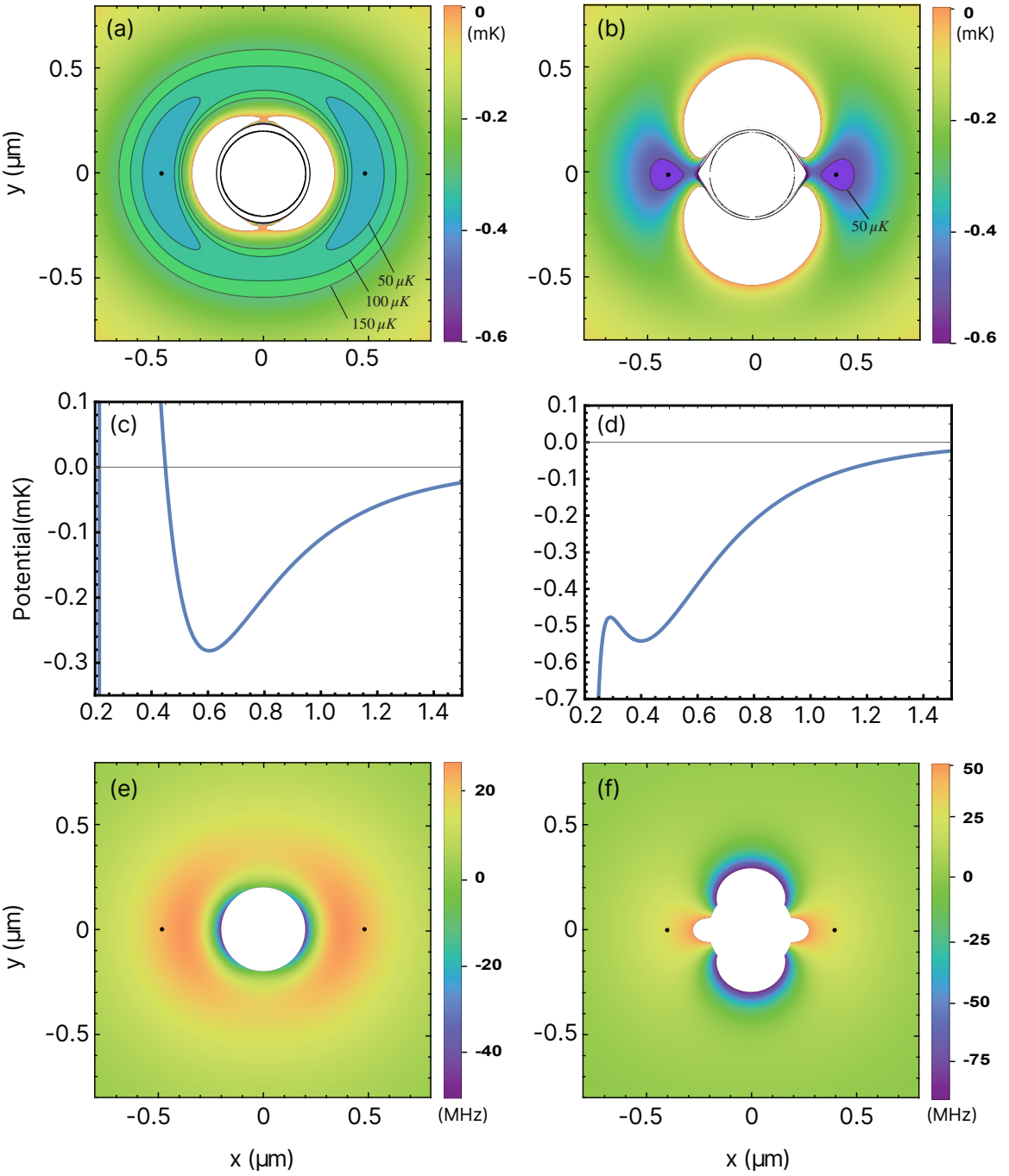

Figure 6.2: Comparison of parallel- (a,c,e) and cross-configuration (b,d,f) fiber traps with red- and blue-detuned trapping fields quasi-linearly polarized parallel and orthogonal to each other, respectively. (a,b) trapping potential in the $x-y$ plane with contours 50, 100 and 150 μK above the minima positions; (c,d) potential along x-axis; (e,f) shift of the $5S_{1/2}(F=2, m_F=0) \rightarrow 5P_{3/2}(F'=3, m_{F'}=0)$ transition frequency due to the trapping fields.

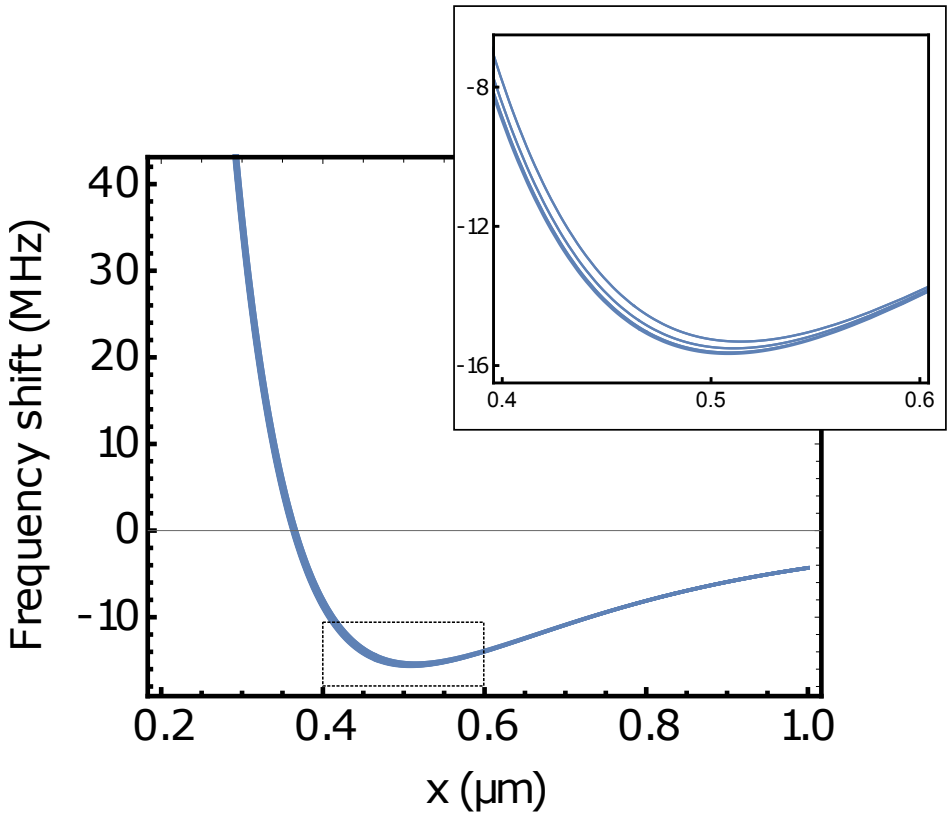

Figure 6.3: Calculated frequency shift of the probe beam transition relative to the cooling transition $5S_{1/2}(F = 2) \rightarrow 5P_{3/2}(F' = 3)$ for trapping in the parallel configuration. Differential shift within the hyperfine manifold of the $5P_{3/2}$ sublevels can be observed in the zoomed plot.

loading was achieved, the cooling and the repump beams were switched off, thereby extinguishing the laser-cooling process and initiating the *measurement-window*. During the *measurement-window*, the probe beam was switched on (after certain delays) for absorption measurements. A typical measurement signal for a probe switched on at zero delay is shown in Figure 6.5. Recording the probe transmission for several delays allowed us to estimate the lifetime of the trap. Each absorption data point was averaged over 25 experimental cycles. The absorption spectrum was obtained by repeating the experiment for different frequencies of the probe laser, scanned around the cooling transition. Figure 6.6 shows an absorption spectrum obtained from fiber-trapped atoms.

Timed analog and TTL[2] voltages were used to control AOM frequencies and amplitudes (thereby controlling the laser frequencies and powers), and to open/close coil circuits to switch the MOT's magnetic field on and off. A GPIB[3] controller set the programmable current supplies for the coils. The probe transmission through the ONF was measured using an SPCM. A volume Bragg-grating (VBG, BG-762-10 F3, OptiGrate) and ruled grating (GR, GR25-1208, Thorlabs) were placed before the SPCM to

[2]Transistor-transistor logic
[3]General purpose interface bus

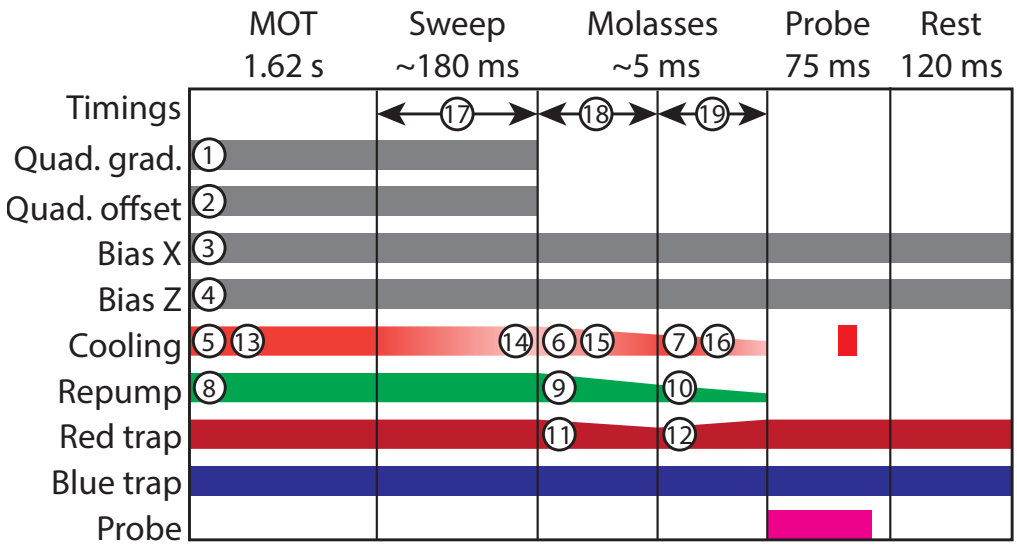

Figure 6.4: Experimental timing diagram and the set of numbered experimental parameters used for trap optimization. The experimental parameters could be set in-loop with the ML generated values during the machine optimization. 1-4: control currents in the MOT magnetic field coils; 5-12: intensities of the 780 nm cooling and repump beams, and the 1064 nm red-detuned trapping beams at different times; 13-16: cooling laser detunings at different times; 17: duration of the cooling laser detuning sweep, i.e., the *sweep-phase*, 18-19: durations of the two sub-periods of the *molasses-phase*.

filter the trapping fields (see Figure 6.1).

Manual optimization Manual optimization of the dipole trap loading took us several months of constant fine-tuning of the experimental parameters. During this process, we adjusted essentially the same set of experimental parameters (see Figure 6.4) and followed the same timing sequence as was later used for the ML optimization, described in the next section. However, manually, we could also adjust the cooling and repump beam alignments and the polarizations of the trapping beams. A typical manual optimization consisted of first maximizing the geometric overlap of the cold atom cloud with the ONF during the optical molasses phase by adjusting the magnetic field amplitude and the position of the zero magnetic field, then slightly realigning the cooling and repump beams. Finally, absorption of the probe through the ONF by the dipole-trapped atoms was maximized by adjusting the 1064 nm and 762 nm trapping beam powers and their relative polarizations.

6.2 Machine Learner Optimization of a Fiber Trap

As mentioned in Section 1.3, the difficulty in measuring the number of trapped atoms in real-time makes the optimization of a trap essentially impossible if one tries to do this manually. Additionally, a complete quantitative description of atom dynamics for the optimal loading of evanescent field dipole traps from a MOT does not exist. The

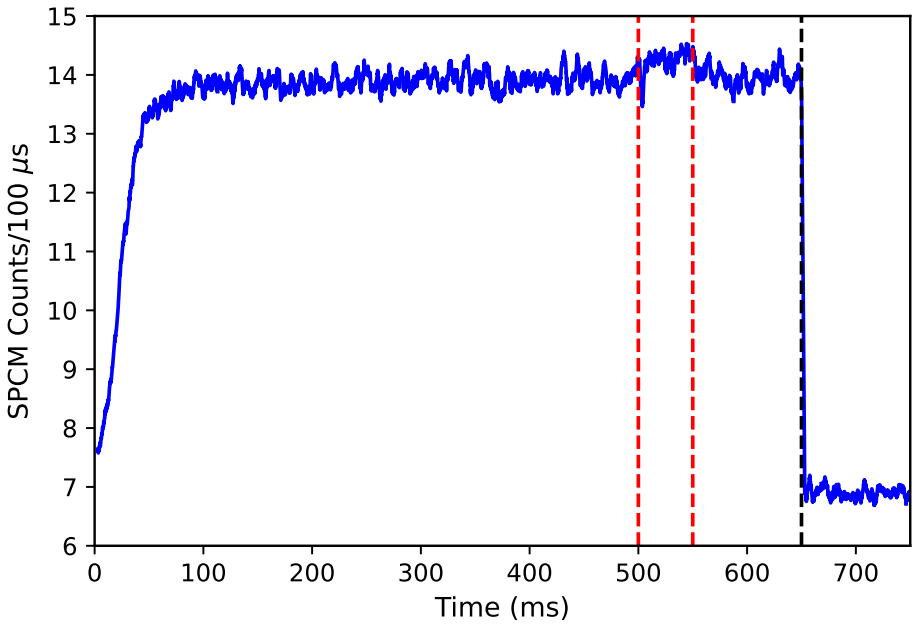

Figure 6.5: Typical SPCM count during the *measurement-window*. Probe transmission was measured for up to 500 ms. A resonant cooling beam was then briefly switched on for 100 ms to kick-out any remaining trapped atoms. The slight increase in photon counts between the vertical red lines was due to the resonant cooling beam coupling to the nanofiber. The photon counts during the 550-650 ms window correspond to the total probe transmission without any absorption. The probe was then switched off at 650 ms, after which the recorded photon counts correspond to the background counts.

complex dynamics involve many-body interactions, light polarization and intensity gradients, and complex scattering processes [181, 182] making it highly intractable when extended to 3 dimensions. As such most applications with trapped atoms revolve around the use of deep traps ($\sim$1 mK).

One can adapt a tractable approach to optimizing a physical system by using *online optimization*, which does not require access to the system's quantitative description. Such an approach has previously been used to optimize the loading of atoms into a Bose-Einstein condensate using a Gaussian process learner [183, 184], for example. This technique allows a learner (or agent) to directly interact with the physical system in an in-loop setting, providing it with new parameters to implement while receiving feedback on its response. For larger parameter spaces, it is better to leverage methods which are computationally more expensive so as to minimize the time spent measuring the physical system. One possibility is the use of deep learning methods, which have been successfully demonstrated for high dimensional problems such as image classification [185] and regression [186]. Here, we employed a deep learning-based optimization protocol developed by Tranter et al. [178], in which a predictive agent, in this case a stochastic artificial neural network (SANN), explored a parameter space by predicting new optima based on the results of its previous predictions.

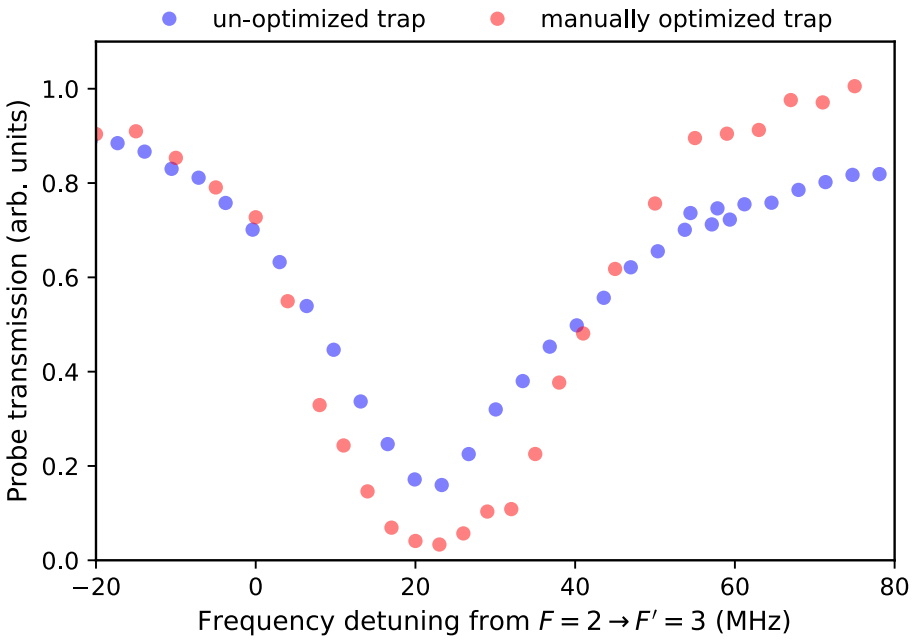

Figure 6.6: Absorption spectrum of fiber-trapped atoms when probed immediately after the *molasses-phase*. All the trapping fields were quasi-linearly polarized along the x-axis as set by the polarization compensation method described in Section 3.2.2. The absorption spectrum obtained was not optimum (shown in blue). The absorption spectrum for a manually optimized trap (red) after polarizations of the trapping fields were adjusted.

6.2.1 Deep learning and stochastic artificial neural networks

Deep learning is extremely good at extracting structures in high dimensional data sets [187]. This realization, coupled with efficient methods for training and evaluation makes it an ideal candidate for representation of a cost landscape[4], as is done in surrogate methods[5]. Deep learning, in essence, refers to the representation of a mapping from input to output data using multiple layers (see Appendix D for more details). This is done by constructing an artificial neural network (ANN), composed of multiple layers of simple and connected nonlinear elements that can be used to approximate functions [188].

One of the main problems with optimization is determining the ratio between exploration and exploitation. This is handled by the use of multiple ANNs and their stochastic nature. Multiple ANNs, when trained on a sparsely sampled data set, often predict different global minima. Each predicted minimum can be tested in succession, facilitating exploration. A discovery of a steep minimum will bias all the ANNs toward exploring that region thereby effecting exploitation.

[4]Cost is a measure of distance of the approximated model function from the target function. Cost landscape refers to the function mapping cost in the parameter space.

[5]In engineering, when an outcome of interest cannot be easily measured or computed, an approximate model is used instead. Methods of constructing approximate models, in the absence of objective functions, are collectively known as surrogate methods.

Stochastic artificial neural networks (SANN) SANN is an ensemble of identical artificial neural networks acting as surrogate models that constitute the mapping from parameter space to a physical cost, which represents the experimental output to be optimized. Stochasticity arises from the independent random initialization of the ANNs in the ensemble which generates multiple unique representations of the experimental response landscape. This provides multiple regions of the parameter space to be explored and allows further optimization or dismissal of those regions as the neural network model is refined. This provides a balance in the exploration versus exploitation trade-off. In our case, the SANN is composed of five ANNs with an identical structure characterized by an input layer of dimension n, followed by five densely connected layers. Each dense layer has 64 neurons per layer with Gaussian error linear unit (GELU) activation[6] [189]. L2 regularization[7] [190] is applied to moderate overfitting behavior. The networks are trained by minimizing the mean squared error using the Adam optimizer[8] [191].

Initial sampling and in-loop optimization An initial sampling policy is used to build a training set to learn an initial representation of the cost landscape. After this initial training, the SANN prediction loop is instantiated. Each network in the SANN generates a set of test parameters by performing a minimization search of the surrogate landscape using parallel L-BFGS[9] instances [192]. Each prediction is tested experimentally, with the resulting cost being added to the training data. With SANN operating in-loop, the search for global minima is more efficient by biasing the search with experimental values. The networks within the SANN are trained and minimized asynchronously to reduce the time taken to generate predictions. This feedback loop continues until some stopping criterion is met. For nonconvex optimization problems the idea of convergence is ill defined without prior knowledge of the problem.

6.2.2 Experimental implementation

The conceptual diagram of the application of the deep learning algorithm to the experimental setup is outlined in Figure 6.7. The machine learner optimization process employs the same experimental sequence used for absorption measurements as described in Section 1.3 and follows an iterative adjustment of $n = 19$ parameters (see Figure 6.4), corresponding to timings, magnetic field amplitudes, optical field powers, and detunings. During an overall 2 s long experimental cycle, the MOT was operated with constant optical and magnetic fields set by the ML during the *MOT-phase* ($\sim$1.6 s). The SANN controlled the cooling beam detuning (12-20 MHz) and intensity (4-8 mW/cm^2), repump intensity (0.1-0.3 mW/cm^2), the magnetic quadrupole field gradient (13-15 G/cm), the zero magnetic field position along the x-axis ($\pm$5 mm), and the magnetic field generated by the compensation coils (upt to 1 G). Numbers in paran-

[6] GELU$(x) = x\Phi(x)$, where $\Phi(x)$ is the cumulative distribution function of a standard normal distribution.

[7] Undesirabe training outcomes are penalized in proportion to the sum of the squares of the weight magnitudes.

[8] Adam is a gradient-based optimization algorithm which requires only first-order gradients with little memory requirement.

[9] Limited-memory Broyden-Fletcher-Goldfarb-Shanno algorithm

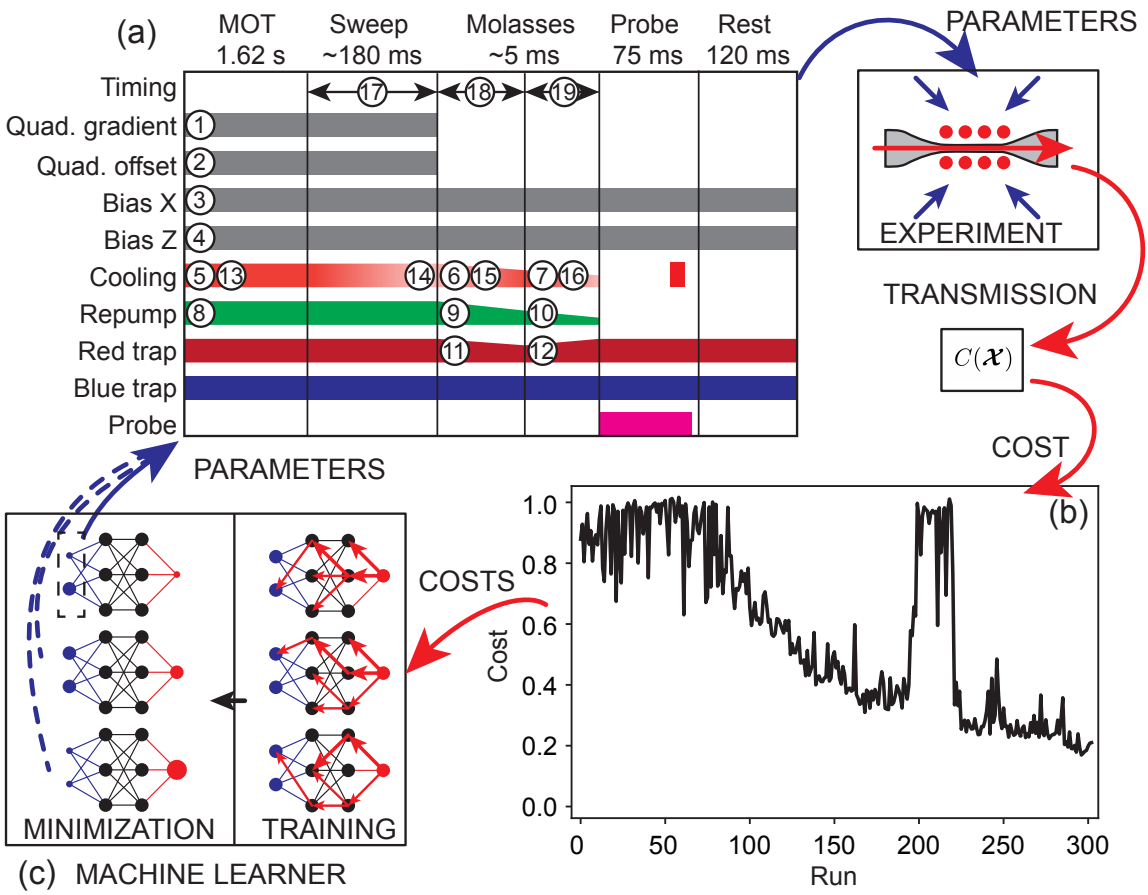

Figure 6.7: Conceptual diagram for online machine learner optimization based on deep learning, showing iterative training of the SANN and the experimental sequence. (a) A set of experimental parameters are generated by the SANN, and the experiment is run with these parameters. (b) A cost value is calculated by averaging the probe transmission, and appended to the cost-parameter data. (c) The data set is used to train the SANN to map the parameter sets to the corresponding costs. The experiment is run iteratively with new parameter sets found by running a minimization algorithm on each ANN in turn.

theses indicate the range of values the SANN was allowed to use when exploring the parameter space. Next, in *Sweep-phase*, the cooling laser frequency was swept (to 12-36 MHz) for the duration t_{sweep} (10-2400 ms) before the magnetic field anti-Helmholtz coils were switched off. The cooling beam frequency/intensity and the repump beam intensity were ramped during the two-step *Molasses-phase*, with the parameters and the durations being set by the ML. The 1064 nm trapping field power was also ramped during this time window, but was otherwise kept constant during the experiment.

We aimed to maximize the number of atoms (N_{trapped}) trapped in the fiber dipole-trap and as such measuring N_{trapped} as a physical cost would be a correct technique. However, for reasons discussed earlier, a direct measurement of N_{trapped} after each experimental cycle would have been too time-consuming and would have significantly impacted the usefulness of the ML optimization process itself. For this method to work

we do not require an exact measure of N_{trapped}, but simply a fast measure of some quantity that is related to it. Transmission of an off-resonant probe beam through the ONF provides us with a straightforward measurement, and is inversely proportional to the number of trapped atoms. Our cost function was set as the average transmission of the probe beam through the ONF, $C(\boldsymbol{\mathcal{X}}) = T_{\text{probe}}$ (where $\boldsymbol{\mathcal{X}}$ represents a point in the parameter space), and hence the aim of the optimization was to minimize this value. Correspondingly, this increased the probe's absorption, which increased with the number of trapped atoms. Predictions from the SANN were used for online optimization, according to the method of [178] with some modifications.

A dummy cycle was run each time the parameters were changed to equilibriate the capture of atoms in the MOT. The transmission of the probe was integrated over the 10 ms window, normalized, and averaged over the following 3 cycles. The experiment was run $2n + 1$ times (where n is the number of parameters being adjusted) using random sets of parameters within the allowed space and measuring the cost each time. This parameter-cost data was used to train the ANNs. The first ANN was then used to predict a set of optimal parameters and the experiment was run with these parameters, generating a new parameter-cost pair to add to the data. The entire data set was used to train the next ANN, which was then used to predict a new set of optimal parameters. This process was continually iterated and, if the ML detected convergence (predicted optima continually lying within a small parameter range), local cost minima outside this region were explored to improve the model around any other possible global minima in the parameter space.

On completion of a preset number (usually 300) of iterations by the ML, the experimental parameters that yielded the largest measured absorption signal (due to the minimized cost) were tested in a second series of experiments to determine the number of trapped atoms and their average temperature. An absorption spectrum of the trapped atoms over the entire absorption window of the $5S_{1/2}(F = 2) \rightarrow 5P_{3/2}(F' = 3)$ transition is shown in Figure 6.8. By recording the absorption spectra with the probe switched on at different delay times after the *molasses-phase* (see Figure 6.9), we estimated the lifetime of the trap to be ~26.5 ms.

6.3 Modeling the Trapped Atom Spectra

We model the absorption of the fiber-guided probe by the dipole trapped atoms in terms of an average optical depth, $OD(\omega)$, of the trapped atoms according to the following equation, which is modified from [96]:

$$OD(\omega) = N \cdot \sum_{m_F} \int_{\substack{\text{Trap} \\ \text{Volume}}} OD_1(m_F, \boldsymbol{\mathcal{E}}_{\text{probe}}) \times \mathcal{L}(\omega - \delta(m_F, \boldsymbol{\mathcal{E}}_{\text{probe}})) \, \rho(U_{\text{dip}} + U_{\text{vdW}}, m_F, T_{\text{avg}}) \, d\mathbf{r}. \quad (6.2)$$

The optical depth then relates to the transmission, $T(\omega)$, via the relation

$$T(\omega) = \exp\{-OD(\omega)\}. \quad (6.3)$$

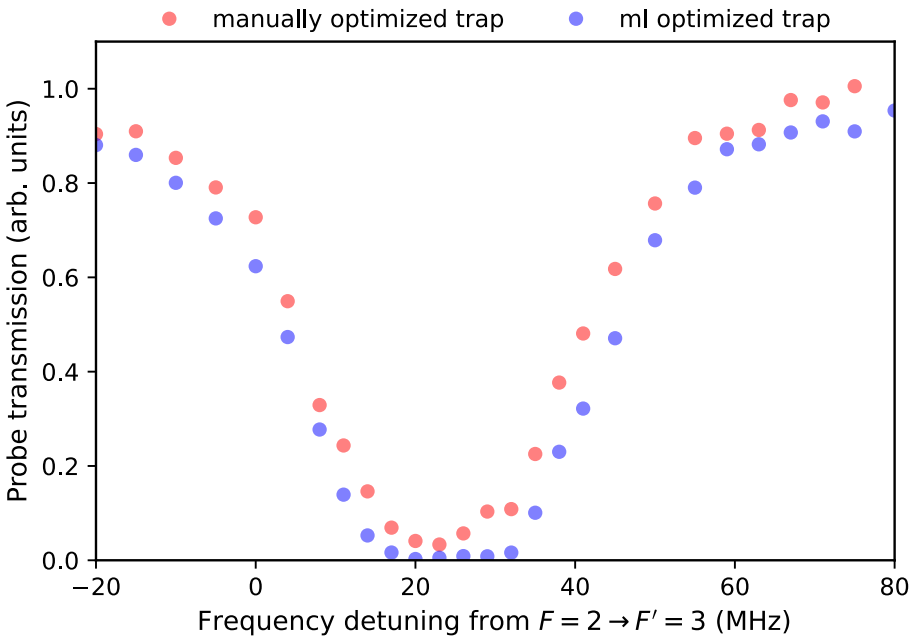

Figure 6.8: Absorption spectrum (blue) of atoms trapped in an ML-optimized fiber trap when probed immediately after the *molasses-phase*. For comparison, an absorption spectrum (blue) from manually-optimized trap is shown.

The atoms were assumed to have a thermal ensemble density, ρ, with an average temperature, T_{avg}, due to an approximate van der Waals potential, U_{vdW}, and an optical dipole potential, U_{dip}, induced by trapping fields. $OD_1\left(m_F, \boldsymbol{\mathcal{E}}_{\text{probe}}\right)$ is the optical depth per atom for each transition. We assumed only Lorentz broadening due to the natural linewidth, $\mathcal{L}$, and a local optical transition shift, $\delta\left(m_F, \boldsymbol{\mathcal{E}}_{\text{probe}}\right)$, due to the light shifts of the ground and the excited state of the cooling transition (as the probe was tuned to the cooling transition). Integrating over the trap volume produces the observed broadening.

OD_1 was calculated for the local probe intensity and polarization, with transition strengths given by the Clebsch-Gordon coefficients and the transition cross-section. The atoms were assumed to have an m_F population distribution due to optical pumping by the probe field. The m_F distribution was determined by the steady-state population transfer due to the probe polarization at the trapping potential minimum, with CG coefficients for the various transitions to the $5P_{3/2}(F' = 3, m_{F'})$ levels and instantaneous spontaneous decay back to the $5S_{1/2}(F = 2)$ (ignoring stimulated emission and other excitation processes).

We calculated the absorption of the probe beam by the trapped atoms for a range of frequencies to compare it with the experimental data. Because the experimental trap intensities and polarizations were only approximately known, a range of these parameters was tested and trends were found to assist with matching to the experimental data. The integral in Equation 6.2 was carried out only over one lobe of the trap to avoid having to use different m_F occupations for the other lobe, where the polarization is different but the absorption symmetry is the same due to the reversal of the

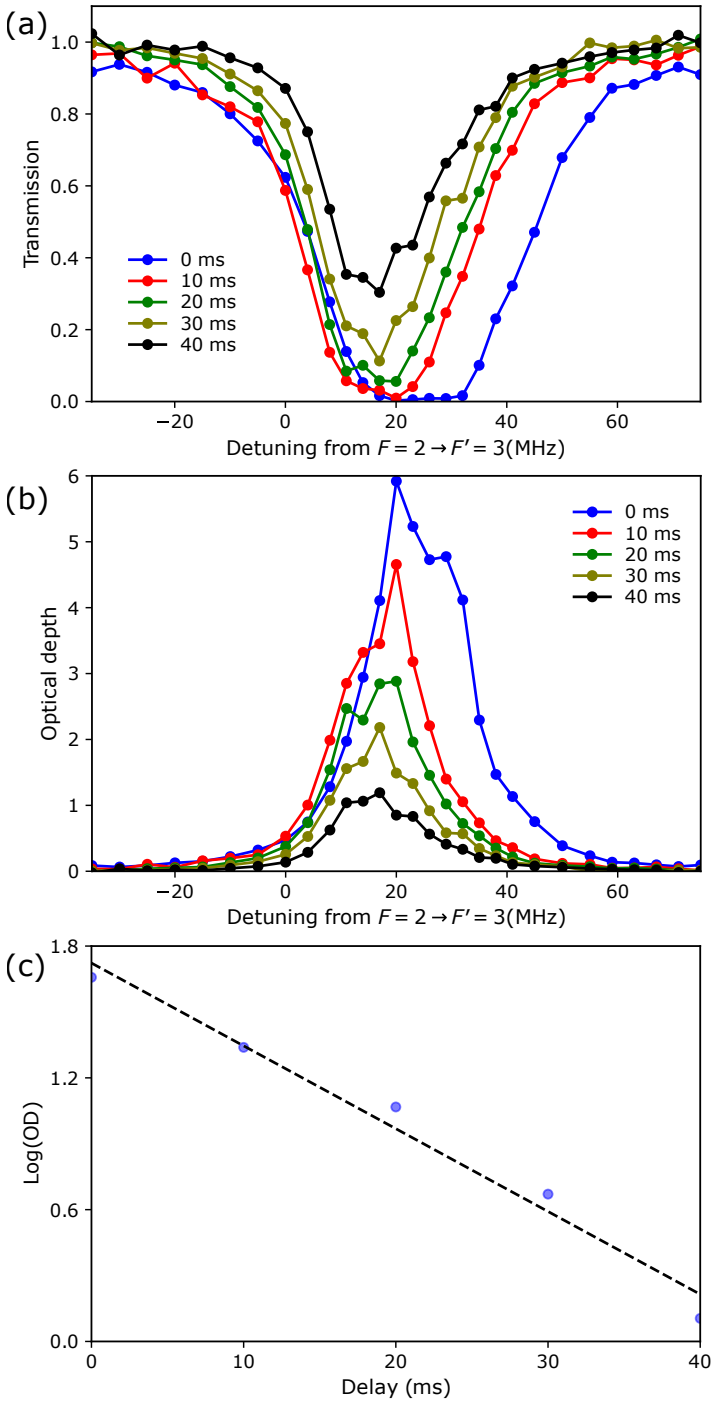

Figure 6.9: Absorption spectrum of atoms trapped in an ML-optimized fiber trap when probed at different delay times after the *Molasses-phase*. (a) Probe transmission as a function of probe detuning; (b) Optical depth as a function of probe detuning; (c) Peak of the logarithm of the OD for each delay. Note: The peak is obtained after fitting the OD in (b) with a skewed Gaussian function.

m_F occupation. The integral was performed with a Monte Carlo sampling method in Mathematica, which is significantly faster than a grid recursion method, for a small

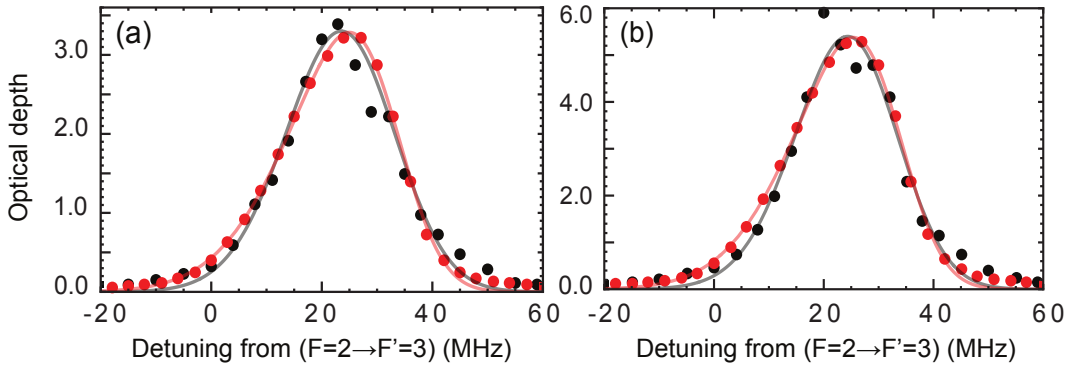

Figure 6.10: Optical depth versus probe detuning for (a) manually optimized and (b) ML optimized traps. The experimental (black points) and modeled (red points) optical depth is fitted with a skewed Gaussian function. The solid lines are the fitted functions to the data points.

sacrifice in precision.

In the experiment, the quantization axis was not well-defined and we assumed an initial unpolarized state of trapped atoms. The model was calculated for a variety of quantization axes. The inclusion of the optical pumping by the probe greatly reduced the effect on the modeled OD due to the choice of quantization axis. A quantization axis in the x- (optical polarization axis) or y-axis gave a fit that predicts roughly the same atom number.

Effects neglected in the model include the change in the linewidth of the atoms due to the presence of the fiber, rescattering into the fiber, motion of the atoms during absorption, detuning of the probe with respect to individual m_F levels within the optical pumping scheme.

Trends for fitting Absorption spectra of the dipole trapped atoms were modeled for a range of different powers and polarizations of the trapping fields, atom temperatures, and fiber diameters. The spectrum that most closely matched the experimental result was selected. The match was quantified fitting the modeled and experimental spectra with a skewed Gaussian function and then choosing the modeled spectrum whose fitted asymmetry, central frequency, and broadening parameters most closely matched the experimental spectrum fitting. The Gaussian fit width increases with temperature, the central frequency increases with overall trap power, and the asymmetry increases as the trap minima move closer to the fiber. These trends make us confident in matching of the modeled spectra to the experimental data, clearly indicating an increase in the optical depth for the ML-optimized system. Figure 6.10 shows the fitted functions for the manual and ML optimized trap spectra.

The skewed Gaussian fits the model data more closely than the experimental data. In the experimental data, the absorption at around 50 MHz detuning is possibly due to atoms that are trapped in tight orbits around the fiber by a combination of van der Waals forces and repulsive blue-detuned light. The maximum positive light shifts close to the fiber surface are around 50 MHz and the absorption from just a few atoms this close to the nanofiber is enough to explain that part of the spectrum.

6.4 Results and Discussion

In Figure 6.11(a) we plot the probe beam transmission as a function of detuning for both the manually optimized (red) and ML-optimized (blue) fiber traps. The theoretical model was fitted using 300 trapped atoms for the manually optimized trap and 450 atoms for the ML-optimized trap. The atoms loaded into the ML-optimized trap were also at a slightly lower temperature of 140 μK compared to 150 μK for the manual trap. The increase in atom number and decrease in temperature in the ML-optimized trap are likely due to improved cooling and increased atomic density in the vicinity of the ONF. Notably, the ML chose non-intuitive experimental parameters in achieving the optimization. For example, the inset to Figure 6.11(a) shows the final position of the atom cloud in relation to the ONF; the ML was inclined to position the cloud to one side of the fiber, in stark contrast to our manual optimization where we centered the cloud on the ONF. While the achieved diferences may appear unremarkable, a 50% increase in the number of trapped atoms has been observed. Figure 6.11(b) plots the same data as optical depth of the probe absorption, showing more clearly the fitting of the model at intermediate detunings. The powers of the dipole trap light fields used to fit the spectra were based on the fitting of the modelled spectra to the transmission data, and are significantly different to experimentally measured dipole trap transmissions at the output of the nanofiber. Losses at the waist due to fiber degradation after being used for about five year (see Figure 6.12), particularly for the 1064 nm light, mean the actual powers at the waist were likely higher than those measured. For example, the measured 1064 nm output power was 2.1 mW and 1.8 mW at either end of the ONF, whereas the modeled absorption spectrum fit a power of 3.25 mW in each direction. For 762 nm light, the measured output power was 1.23 mW whereas 1.3 mW was fitted by the model.

Figure 6.11(c) shows the trapping potential in the $x-y$ plane for the modeled trap. The quasi-linear polarization of the trapping fields in the model was adjusted to fit the experimental spectrum. Contour lines emphasize that this resulted in an asymmetric trap. This configuration was previously shown to increase the OD per atom by moving the trapping sites closeer to the ONF [96]. Figure 6.11(d) shows the corresponding light shifts of a probe transition $m_F = 0 \rightarrow m_{F'} = 0$, with the potential minima marked by dots.

Figure 6.13 shows the dependence of the learned cost on a selection of the experimental parameters, centered on the best observed value. This data is not entirely accurate as the slices represent mostly unsampled areas of parameter space. However, these plots are somewhat useful as they indicate which of the parameters played an important role and which had little role in the ML optimization, and can therefore be neglected. They indicate if the parameter range is needed to be changed to explore a different landscape. For example, the repump laser intensity (i), the cooling laser detuning (iv) and the gradient magnetic field along the z-axis (v) have the strongest effect over their allowed ranges, showing the sensitivity of the cost to these parameters. The numbers in parantheses correspond to the labels in Figure 6.13. Due to this sensitivity, we set the magnetic quadrupole parameters as a gradient and position offset to allow the ML to quickly explore this space (in contrast to setting parameters for individual currents through the two quadrupole coils). Learned parameters were

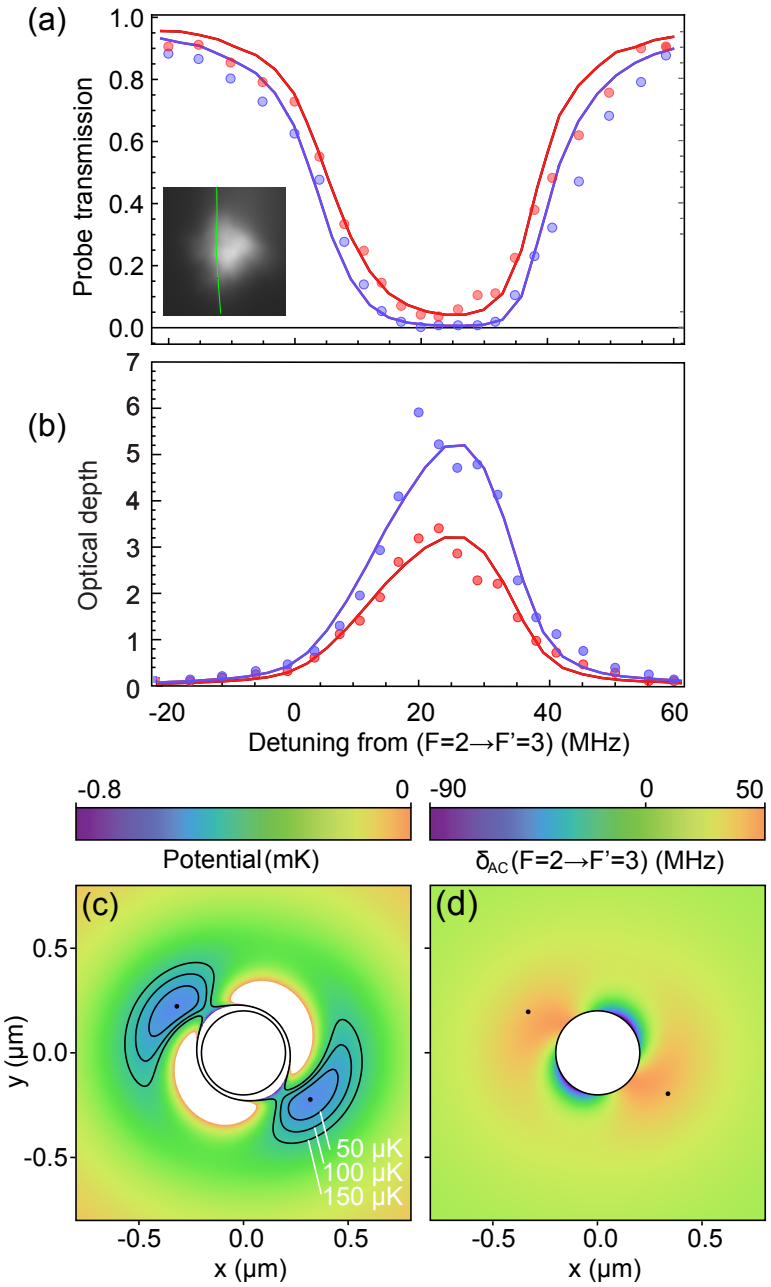

Figure 6.11: (a) Probe transmission spectra after manual optimization (red dots) and ML optimization (blue dots) of loading atoms into the fiber dipole trap. The solid curvers are the theory fits for manual optimization (red: 300 atoms at 150 μK) and ML optimization (blue: 450 atoms at 140 μK). Inset: Image of atom cloud at the end of ML-optmized loading, with the ONF highlighted in green. (b) Same data plotted as absorption spectra. (c) Trapping potential in the $x-y$ plane used to produce the theory fits in (a) and (b), with contours of 50, 100 and 150 μK above the minima positions. (d) Modeled frequency shift of the probe transition due to the trapping light fields. Black dots mark the trapping potential minima in (c) and (d).

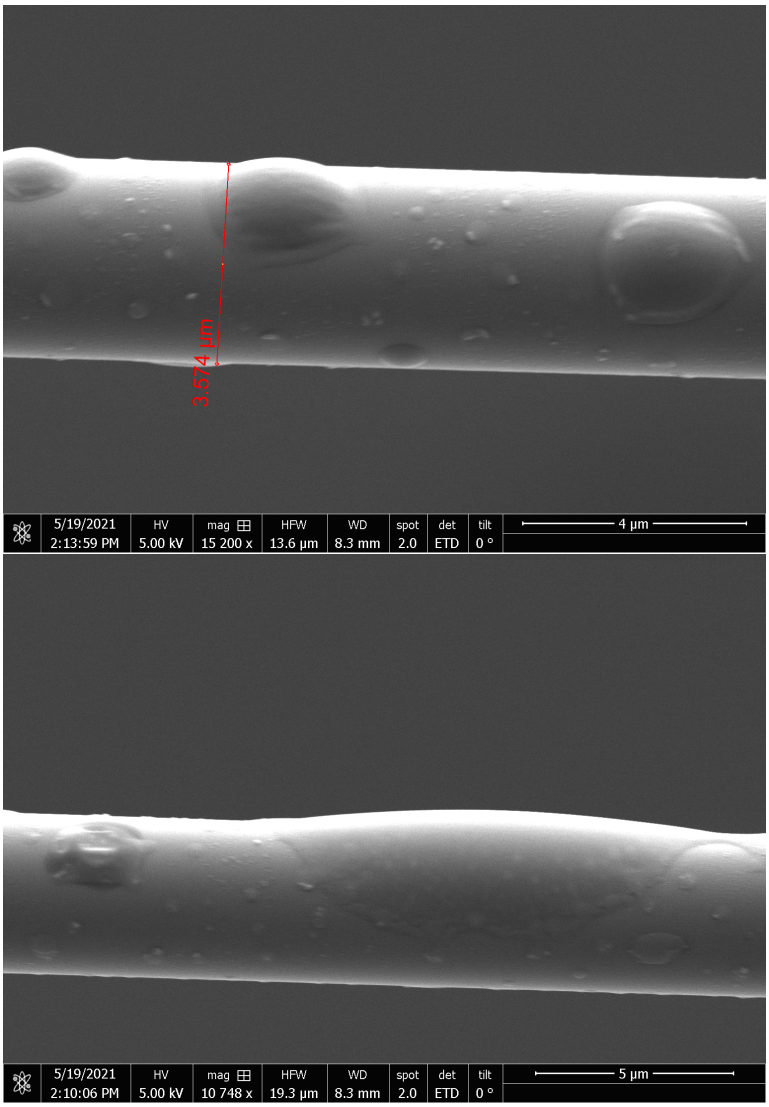

Figure 6.12: Scanning electron microscope (SEM) images of the taper region of the optical nanofiber that was used in our experiments. The images were taken by Dr. D. Brown after the ONF was removed from the vacuum chamber after being in use for about 5 years. The large bumps are possibly dust particles and the small speckles are, we assume, due to RbO_2 deposition on the surface.

stable over time, and reusing the parameters from a single optimization produced a reasonably constant number of trapped atoms over a period of about one month, with no more than $\pm 10\%$ change observed.

Given the sensitivity of the ML to the magnetic fields, we hypothesize that optimal positioning of the MOT as well as the position of zero magnetic field for polarization-gradient cooling are the largest improvements given by the ML. By increasing the number of parameters available to the ML beyond 19, we would expect further improvements. In particular, experimental improvements including a time-varying magnetic field to compress the atomic cloud and thereby increase density before loading, and the ability to change the dipole trapping powers more during loading without causing

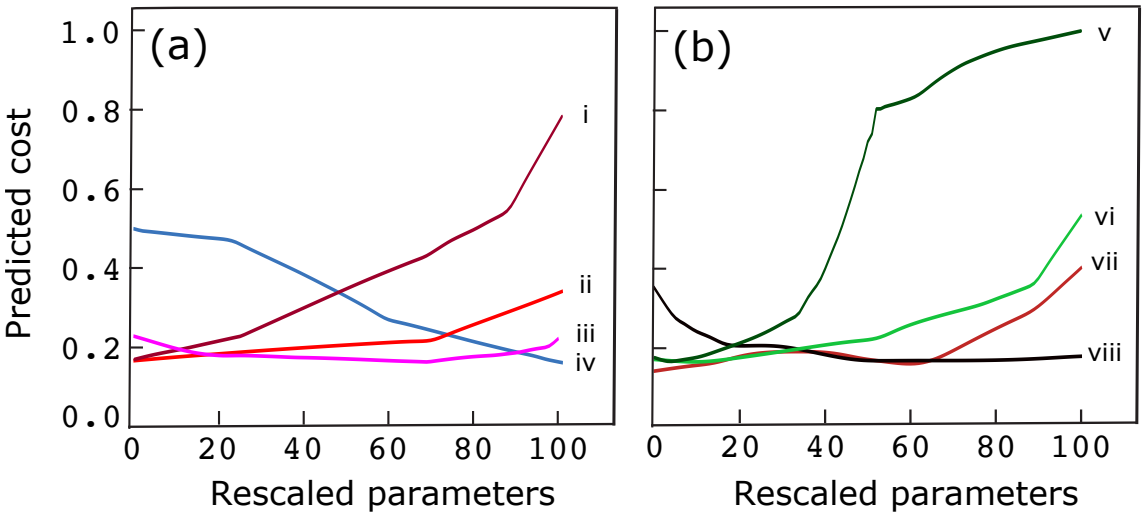

Figure 6.13: Cost predictions from one of the ANNs after 300 training steps. The cost prediction is the output of the neural network while varying individual (a) optical and (b) magnetic field parameters, keeping the remaining parameters constant at the predicted optimum. The optical parameters are those used during the *Molasses-phase*. The corresponding parameters are: (i) repump laser intensity, (ii) cooling laser intensity, (iii) 1064 nm laser intensity, (iv) cooling laser detuning; magnetic field strength of the compensation coils along the (v) y-axis, and (vi) x-axis, (vii) quadrupole field gradient, (viii) magnetic field offset along y-axis. Parameters are scaled to range from 0 to 100.

movement of the fiber, should allow more atoms to be loaded.

A direct measurement of atom number, by measuring the total absorbed power of a strong probe saturating the trapped atoms, was not possible. The force due to the light shift by the strong probe beam pushed atoms from the dipole trap array before a reliable measurement could be taken. A heterodyne measurement setup should make this type of measurement possible, due to more sensitive detection of coherent light. This would also allow a more direct measurement of trap properties using the method in [193]. We tried but failed to set up this type of detection.

6.5 Conclusion

We used a machine learner optimizer to increase the number of ^{87}Rb atoms trapped in nanofiber-based evanescent field dipole traps from 300 (for manual optimization) to 450 in a proof-of-principle experiment. We derived a microscopic theoretical model that fit the experimental probe transmission spectra and enabled us to determine the number and average temperature of trapped atoms. When ML optimized, we increased the number of trapped atoms by 50% and optical depth by 66%. We expect this to be further improved by (i) increasing the number of parameters controlled by the machine learner and (ii) using a new ONF in the experimental setup. Additional investigations of the capabilities of this setup are planned, including optimizing the loading of atoms for a

collective atom-light interactions such as four-wave mixing, and increasing the number of nearest-neighbor interactions in a 1D lattice of Rydberg atoms. The techniques developed here can be extended to any atomic species where it is desirable to increase the atom number.

Chapter 7

Degenerate Four-Wave Mixing with Paraxial Beams in Rubidium Vapor

Until this point, we have focussed our studies on interactions of cold ^{87}Rb atoms with the evanescent field of a nanofiber. We studied the dependence of a two-photon transition rate in rubidium (hot vapor) on the polarization of a 993 nm free-space pump beam (described in Chapter 5), but it was also in the context of comparison with the transition rate in case of nanofiber-guided pump light. Here, we focus our attention onto a degenerate four-wave mixing (FWM) interaction with free-space beams in a rubidium vapor cell. Our goal was to study the transfer of orbital angular momentum (OAM) between fields involved in a degenerate FWM process, where the two-step excitation with 780 nm and 776 nm light was replaced by a single-frequency, two-photon excitation with 778 nm in the widely studied diamond energy structure in Rb (see Figure 7.1) [194–202]. While this is an incomplete work, we discuss the motivation and report the current status of the experiment, the limitations encountered, and the improvements that could be made.

7.1 Four-Wave Mixing

Four-wave mixing is a nonlinear interaction between light and matter, associated with the third-order susceptibility $\chi^{(3)}$, that permits the transfer of energy and momentum between four optical modes via interaction with a medium. The susceptibility tensors, $\chi^{(n)}$, relate to the polarizability of the medium; as such the response of a dielectric material to the applied optical fields is written as [203]

$$\mathbf{P} = \epsilon_0 \left(\chi^{(1)}\mathbf{E} + \chi^{(1)}\mathbf{EE} + \chi^{(1)}\mathbf{EEE} + \cdots \right), \tag{7.1}$$

where $\mathbf{E}$ is the electric field and $\mathbf{P}$ is the polarization of the material. Typically, nonlinear susceptibilties ($\chi^{(n)}$, $n > 1$) are negligibly small for neutral atoms [203] and a high intensity pump laser is required to induce a strong nonlinear polarization. The $\chi^{(2)}$ term vanishes in neutral atoms due to inversion symmetry and the lowest nonlinear response of an atomic medium comes from the $\chi^{(3)}$ term.

Phase matching Efficient FWM requires the four optical fields to remain in phase

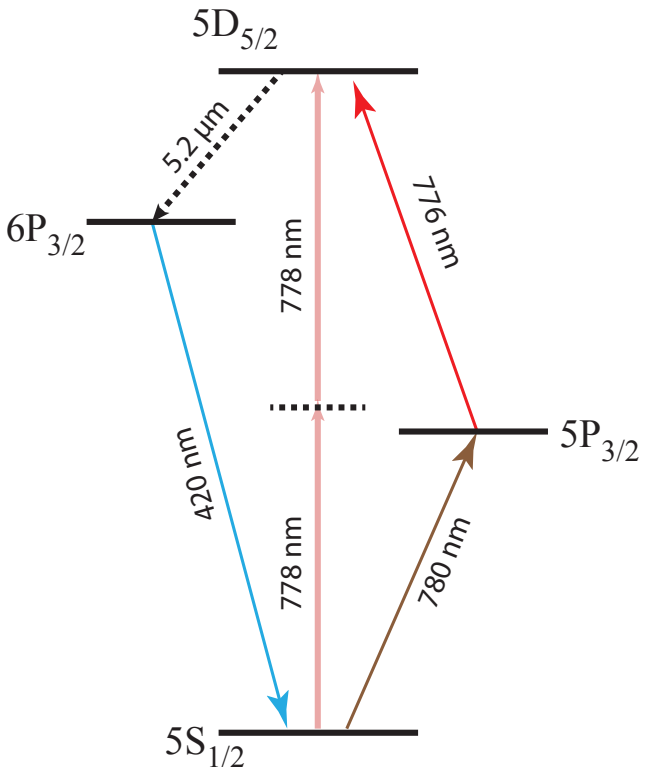

Figure 7.1: Energy level diagram relevant to diamond four-wave mixing in rubidium. The dashed line represents a virtual energy level.

throughout the mixing process in order to avoid any destructive interference. This amounts to the requirement of energy and momentum conservation across a single FWM cycle [204]. Under energy and momentum conservation, two excitation optical fields result in the generation of two additional coherent fields, via FWM interactions. The conservation of energy requirement is naturally met in the case of the diamond energy structure in Rb (see Figure 7.1) as

$$2 \cdot \omega_{778} = \omega_{780} + \omega_{776} = \omega_{5.2} + \omega_{420}, \tag{7.2}$$

where ω represents the angular frequencies of the field given in subscript. Momentum conservation leads to the following criterion

$$2 \cdot \mathbf{k}_{778} = \mathbf{k}_{780} + \mathbf{k}_{776} = \mathbf{k}_{5.2} + \mathbf{k}_{420}, \tag{7.3}$$

where $\mathbf{k}$ represents the wave-vectors associated with the fields given in the subscript. A spatially extended atomic ensemble provides translational symmetry, which thereby leads to momentum conservation. The constraints imposed by phase-matching are responsible for the highly directional nature of optical fields produced by FWM. This has proven useful for efficient frequency conversion [194, 205, 206] and in the generation of correlations [73, 207–210] and entanglement [74, 211] in quantum optics.

Conservation of orbital angular momentum The phase matching condition

leads to OAM conservation in the FWM process, resulting in the transfer of transverse phase structure between the pump and generated fields [197, 199]. Deviations from perfect phase matching conditions lead to the large spatial bandwidth of the OAM shared between the generated fields [202]. For the diamond configuration considered here (see Figure 7.1), the probability amplitude to generate a specific combination of blue (420 nm) and infrared (5.2 μm) modes is given by the overlap with the pump profiles. The transfer of OAM is a signature of such a nonlinear interaction and has been exploited as a tool to distinguish nonlinear processes in an atomic medium [212].

7.1.1 Motivation

One of our interests has been in studying collective light-atom interactions, including FWM in an ensemble of atoms coupled to an optical nanofiber mode. This is a subject for future study for which a crucial stepping stone was the implementation and optimization of the ONF-based trap presented in Chapter 6. It is desirable to utilize FWM in an ONF system as it has the obvious advantage of being directly compatible with the standard optical fiber network - the dominant optical transmission platform. FWM utilizing the inherent $\chi^{(3)}$ nonlinearity of optical fibers has been studied [213] and exploited to generate correlated photon pairs [214–217].

The diamond energy level structure in Rb (see Figure 7.1) has been widely studied by now. The atoms are pumped to the $5D_{5/2}$ excited level with 780 nm and 776 nm pump fields. The cascaded decay through the $6P_{3/2}$ level generates 5.2 μm infrared light and coherent blue light (CBL) at 420 nm via the parametric FWM process due to the strong atomic coherences in the energy level structure. Replacing the two-step excitation by a single-frequency two-photon excitation with 778 nm, we can, in principle, achieve two competing diamond degenerate FWM interactions with one producing fields at 776 nm and 780 nm in case of cascaded decay through the $5P_{3/2}$ level and another producing fields at 5.2 μm and 420 nm in case of decay through the $6P_{3/2}$ level. This scheme is appealing, particularly the decay through $5P_{3/2}$, as all the wavelengths involved (776 nm, 778 nm and 780 nm) are very close to 780 nm for which the ONF (∼400 nm diameter) was optimized for studies with Rb. Additionally, all these fields propagate with a similar HE_{11} mode profile in the ONF, facilitating better phase-matching. The other diamond structure producing 5.2 μm and 420 nm fields is also interesting as 5.2 μm cannot propagate through the ONF while 420 nm will have several guided modes available, namely, HE_{11}, HE_{21} (even and odd), TE_{01} and TM_{01}. This elicits further studies on this transition in the context of optical nanofibers. The higher order modes in nanofibers can carry OAM and the possibility to transfer high-density information encoded on OAM [218] to a cold atomic ensemble [219] coupled to an ONF is particularly interesting.

Inspired by these interests, we started to investigate degenerate FWM with a 778 nm single-frequency pump. In particular, we focused on studying the angular momentum distribution of the coherent blue light generated by an OAM-carrying pump. A recent study [202] showed the OAM distribution between the infrared (5.2 μm) light and the CBL depends on the pump modes and the overlap between them. Any mismatch in overlapping of pump modes should also manifest in the OAM distribution. The use of a single pump (in our case at 778 nm) simplifies the mode-matching condition,

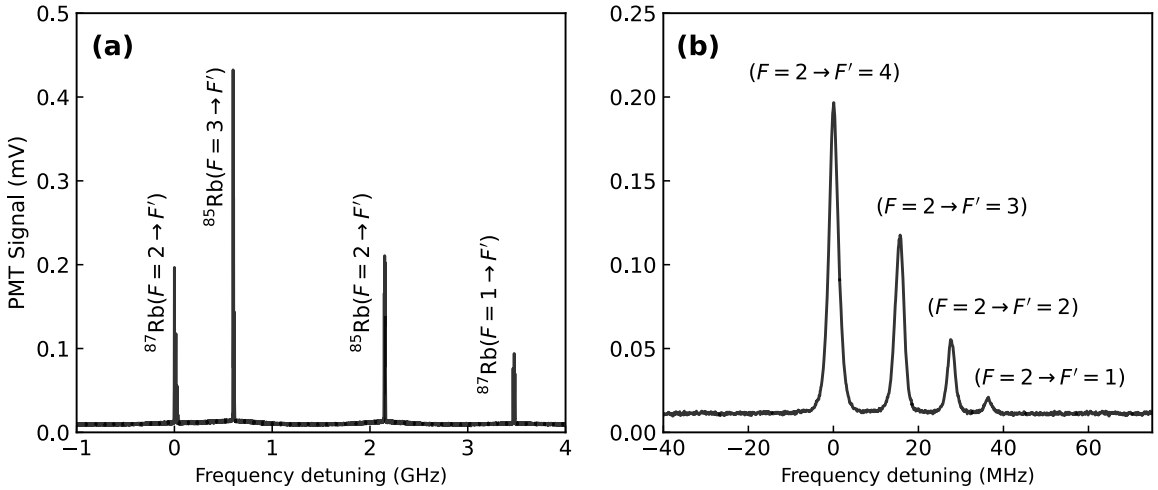

Figure 7.2: Two-photon spectroscopy signal for the $5S_{1/2} \rightarrow 5D_{5/2}$ two-photon transition in Rb at 778 nm. (a) The 778 nm pump laser is scanned across the ^{87}Rb and ^{85}Rb transitions. (b) Hyperfine peaks of $F = 2 \rightarrow F'$ transitions in ^{87}Rb. The detuning is relative to the ^{87}Rb ($F = 2 \rightarrow F' = 4$) transition.

allowing us to remove any possibility of pump mode mismatch. To study the OAM transfer in the FWM process we used Laguerre-Gaussian (LG) pump modes, which are characterized by their azimuthal (l, integer) and radial (p, non-negative integer) indices, with each mode carrying $l\hbar$ of OAM per photon [220].

7.2 Experiment

Figure 7.3 shows a schematic of the experimental setup. A 778 nm beam output from a fiber-coupled TA (BoosTA, Toptica) was split with one part (10%) going to a reference spectroscopy setup and the other (90%) going to the FWM experimental setup.

A reference two-photon spectroscopy signal (see Figure 7.2) was obtained from a Rb vapor cell (VC1, 75 mm in length and 25 mm in diameter, with natural abundances of the Rb isotopes) maintained at 60°C using a Thorlabs heater assembly (GCH25-75) with a temperature controller (TC300, Thorlabs). The 420 nm fluorescence was filtered with an interference filter centered at 420 nm and detected by a PMT through a telescope arrangement of two plano-convex lenses ($f_1 = 50$ and $f_2 = 100$ mm).

The 90% part of 778 nm beam output was collimated to produce a clean Gaussian beam through a 7.5 mm triplet collimator and then diffracted from a LabVIEW-controlled spatial light modulator (SLM, Exulus HD, Thorlabs) to generate LG beams with different l indices. The LG beam was focused into a second heated Rb vapor cell (VC2, 75 mm in length and 25 mm in diameter) through a 125 mm lens. The waist diameter at the focus was calculated to be ∼16.5 µm using a simple lens equation [221]. The Rb cell was heated by wrapping the cell with aluminium foil and a resistive heating tape whose temperature was controlled by AWP 1000 controller.

The CBL emission at 420 nm was filtered using a combination of dichroic mirrors (long pass at 650 nm) and interference filters (shortpass filter at 500 nm and bandpass

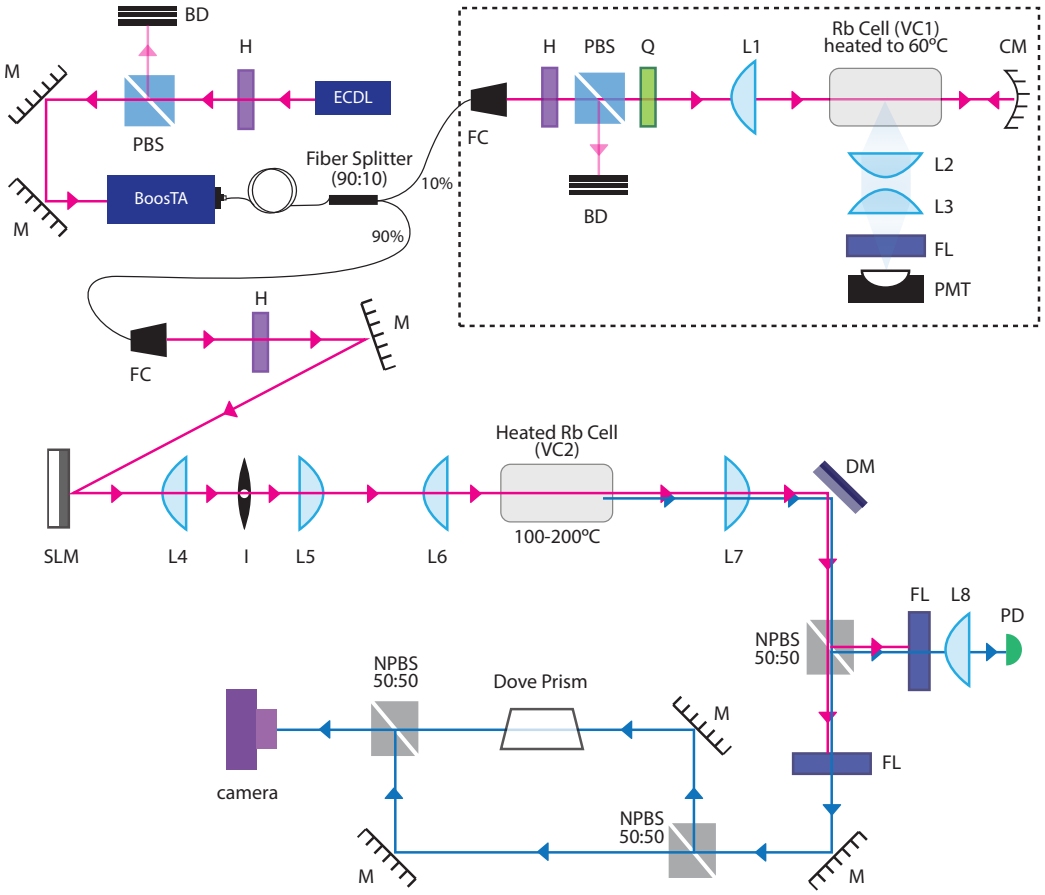

Figure 7.3: Schematic of the experimental setup. BD: Beam dump, CM: Concave mirror, ECDL: Extended cavity diode laser, FC: Fiber coupler, FL: A shortpass filter at 500 nm with a bandpass filter at 420 nm, H: Half-wave plate, I: Iris, L1-L7: Plano-convex lenses, M: Mirror, NPBS: Non-polarizing beam-splitter, PBS: Polarizing beam-splitter, PD: Photodetector, PMT: Photo-multiplier tube, Q: Quarter-wave plate, SLM: Spatial light modulator.

filters at 420 nm). The CBL power was measured with a photodetector (DET25K/M 150-500 nm, Thorlabs) and imaged with an EMCCD (iXon Ultra 897, Andor). Since the pump light was very intense, it was imaged with another camera (DCC1645C, Thorlabs).

7.2.1 CBL generation with a Gaussian pump beam

The 778 nm transition two-photon transition is about 1000 times weaker than the two-step $5S_{1/2} \rightarrow 5D_{5/2}$ transition using 780 nm and 776 nm [222], thus requiring higher intensities of the 778 nm pump light and higher atom density for efficient CBL generation. We observed CBL generation as a function of pump power and temperatures (see Figure 7.4) for a Gaussian beam input. This is equivalent to pump intensity and atomic density, respectively. For this we bypassed the SLM setup to use the maximum available power 470 mW of 778 nm from the TA output. No signal was observed for a

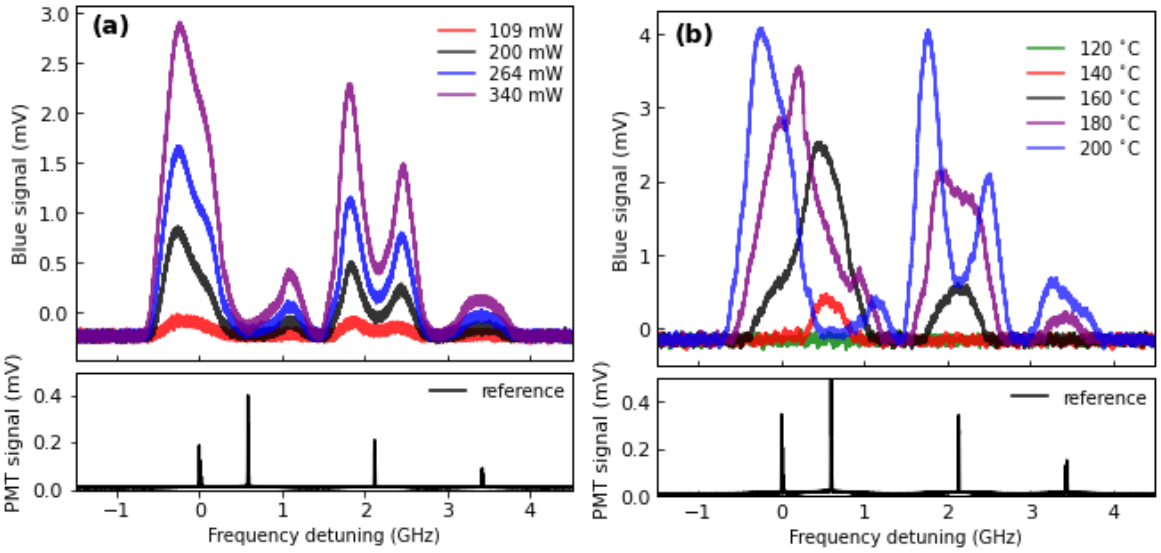

Figure 7.4: CBL signal from a heated Rb cell with ^{87}Rb and ^{85}Rb in natual abundances. (a) For different 778 nm pump beam power when the cell was maintained at 200°C. (b) For different cell temperatures with 778 nm pump power of 450 mW. Bottom panel shows the scale of the frequency-reference spectrum obtained from the reference cell.

pump power less than 100 mW when the Rb cell was maintained as hot as 200°C. Note that the location of the interaction region within the vapor cell was also crucial for the observation of the signal. The signal was observed only when the effective interaction region, i.e., the pump beam focus, was close to the exit window of the vapor cell. The optimum signal was obtained by translating the vapor cell along beam propagation axis and finding a suitable point of focus. This is perhaps due to the re-absorption of the generated blue light by the Rb atoms.

It is clear from Figure 7.4 that the CBL generation efficiency was typically higher at a certain detuning from the transition and that the detuning at which maximum efficiency was observed shifted for different temperatures. In addition, we notice that the spectra are well overlapped for the two isotopes. For a simpler system, we replaced the Rb vapor cell (VC2) with a ^{87}Rb enriched vapor cell. Figure 7.5(a) shows the measured CBL generation as a function of vapor cell temperature. While we saw peaks centered around the reference transition peaks for lower temperatures (100°C), we observed peak splitting for higher temperatures, with the peak separations increasing as a function of temperature. See, for example, the red (120°C) curve. In terms of efficiency, we measured higher peak CBL power for 370 mW pump power as compared to that with the mixed vapor cell. We observed consistent peak splittings and peak separations for different input pump powers (see Figure 7.5(b)). The signal was also increased due to improved detection of the CBL by focusing it on to the detector. We observed CBL for a pump power as low as 40 mW.

Note the vapor cells were not suitable for operation at temperatures higher than 120°C. Higher temperatures caused the adsorption of Rb by the glass cell wall.

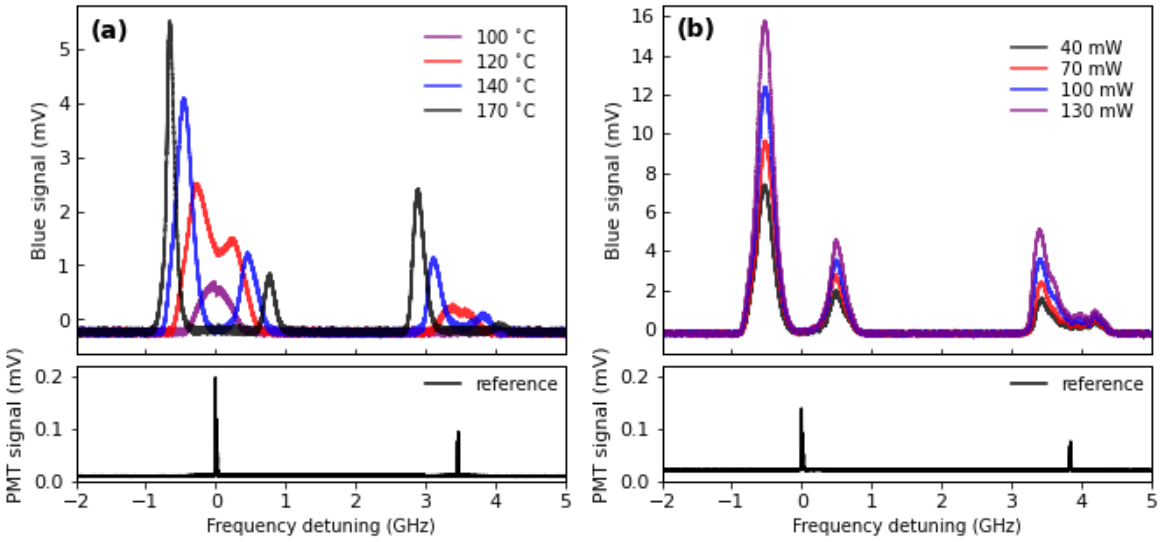

Figure 7.5: CBL signal from a heated ^{87}Rb enriched vapor cell. (a) For different cell temperatures with 778 nm pump power of 370 mW. (b) For different 778 nm pump beam power when the cell was maintained at 140°C. Bottom panel shows the scale of the frequency-reference spectrum obtained from the reference cell. Reference peaks corresponding to only ^{87}Rb are shown.

7.2.2 Generation and identification of LG modes

We used a phase-only SLM with a fork-hologram pattern [223] to impart a desired phase (controlled with a LabVIEW program) onto the collimated pump Gaussian beam, thereby generating LG modes. While this is straightforward and a widely used method, where the first diffracted order is the useful phase-imprinted beam, it was challenging to find a balance between the quality and power of the beam. Both factors were very important in our case: the quality of the beam determined the purity of the generated modes which is crucial for the study of OAM transfer and high pump beam power was required for the transition we considered. We could obtain up to 180 mW in the first diffracted order (which translates to a diffraction efficiency of ∼38% for 470 mW input); however, we could not obtain good beam shape quality (as shown in the left panel of Figure 7.6). To improve the beam quality we added an intensity mask (approximating the intensity profile of a desired LG mode) to the LabVIEW generated SLM hologram. The right panel in Figure 7.6 shows the intensity profiles of the first two ($l = 0, 1$) LG modes. However, the maximum power we could get was ∼90 mW for $l = 1$ and decreased monotonically for higher l order LG modes.

The quality of generated LG beams could be improved further by introducing a lens before the SLM to slightly focus the input beam. This worked perhaps due to the inherent curvature of the SLM surface. The maximum first-order efficiency that could be obtained was about ∼32%, which translates to 150 mW in LG beams with the maximum available power of 470 mW in the input beam. Also, the obtained power was consistent for higher l modes. Images of beams generated with and without the lens at the SLM input are shown in Figure 7.7. To determine l, the beams were passed through a Mach-Zehnder interferometer containing a Dove prism in one of the arms. The Dove

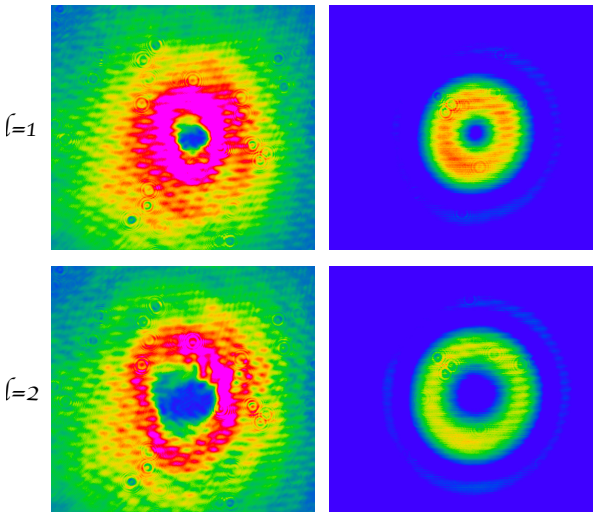

Figure 7.6: Images of non-optimal $l = 1$ and $l = 2$ LG modes. Left: Beams generated with a simple fork-hologram on the SLM. Right: Beams generated with additional intensity mask on the fork-hologram.

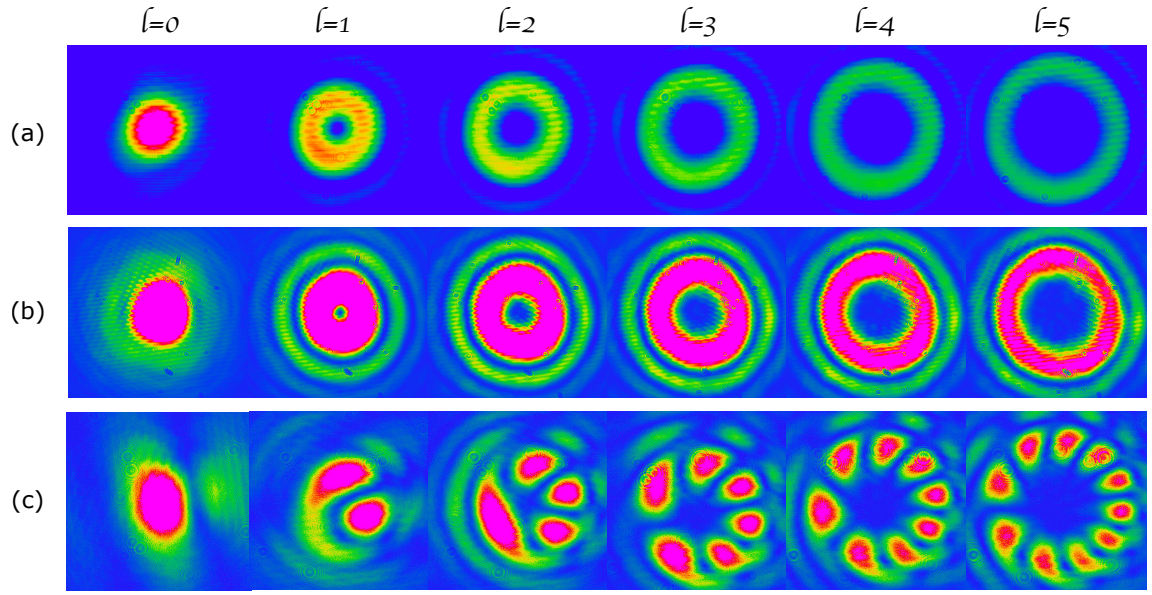

Figure 7.7: Images of different l-order LG beams. (a) Beams generated with a collimated Gaussian input onto SLM. (b) Beams generated with slightly focused Gaussian input onto SLM. (c) Interference pattern obtained when the LG beams are imaged through a Mach-Zehnder interometer with Dove prism in one of the arms.

prism flipped the phase effectively converting a $+l$ mode to a $-l$ mode. The resulting superposition of $\pm l$ modes exhibits $2l$ lobes in the interference pattern, as shown in Figure 7.7(c). This offers identification of the modes either by visual inspection (for simple cases) or by analyzing the Fourier components of the image [202, 224].

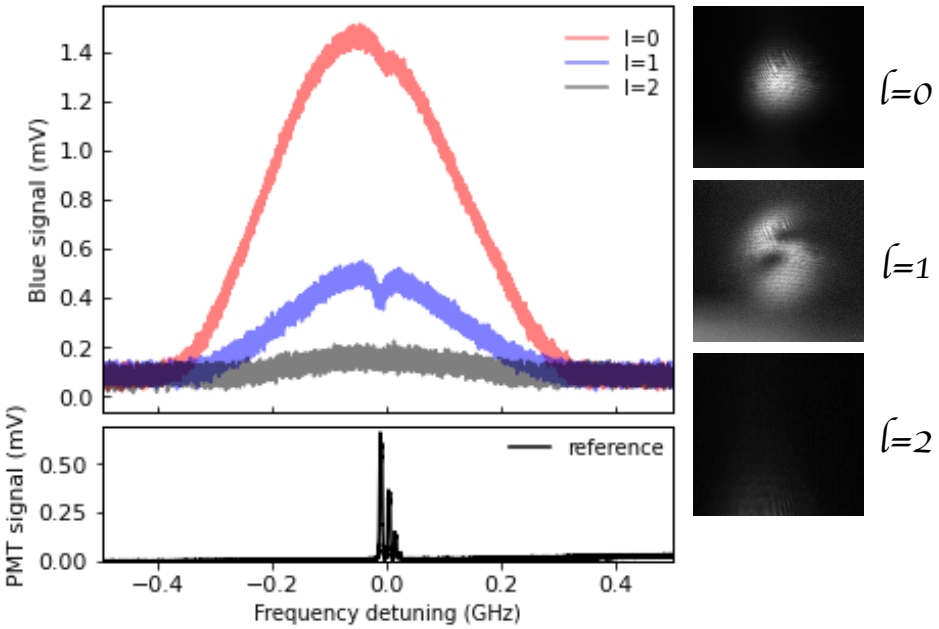

Figure 7.8: Measured CBL signal for an LG pump input beam with different l indices. The images on the right panel show transverse intensity profiles of the CBL output corresponding to different LG pumps. The bottom panel shows a reference two-photon transition spectrum.

7.2.3 CBL generation with LG pump beams

The generated 150 mW LG beams were focused into the ^{87}Rb enriched vapor cell maintained at 130°C[1] and the CBL output was measured for different l orders of the pump (see Figure 7.8). The CBL output decreased as the order of l increased, with no signal observed beyond $l = 2$. Beam shape imaging revealed an unexpected superposition mode for the $l = 1$ LG pump.

7.3 Conclusion

We observed some interesting effects in the 778 nm degenerate FWM process, in particular the peak splitting observed in the coherent blue light emission for higher temperatures of the vapor cell (shown in Figure 7.5) and the intensity profile of the CBL beam (shown in Figure 7.8). For studying the OAM distribution in this diamond FWM process, the main limitations were the maximum available pump power and the maximum working temperature for the vapor cell. We have already obtained vapor cells, from the University of Stuttgart, Germany, which could potentially sustain temperatures up to 200°C. With this, we expect to see signal for higher l order inputs. A higher pump power could also be obtained, if needed, either by using a Ti:Sapphire laser or with a new TA chip that could output up to 4 W of optical power.

[1]The experiment was performed before we realized 120°C was the upper limit of safe operating temperature for the cell.

As outlined in Section 7.1.1, it is worth investigating the 778 nm degenerate FWM process further for its relevance in fiber-based correlated photon pair sources and high-dimensional OAM-encoded quantum memories. The scheme could be used for storing optical phase information in cold atoms coupled to an ONF. Further, this opens a path toward OAM-enabled hyperentanglement. Additionally, this could provide a method to attain fiber-based novel wavelength lasers.

Conclusions and Outlook

The work presented in this thesis has largely been motivated by the usefulness of the optical nanofiber-atom system toward quantum technology developments, in particular for quantum information applications where a fiber-based system that naturally integrates in the optical fiber network (a backbone for any information sharing and distribution channel) is advantageous. We sought to extend the applications of the atom-nanofiber platform for light-atom interactions, in particular with cold ^{87}Rb atoms.

We demonstrated an electric quadrupole transition in a cold ^{87}Rb atom cloud interacting with 516.6 nm pump light facilitated by the intense gradient of the evanescent field of the nanofber. This established ONFs as an excellent and accessible platform to drive such quadrupole-allowed transitions. Direct access to electric quadrupole transitions might be benefical for fiber-based clocks. In the specific case of the $5S_{1/2} \rightarrow 4D_{3/2}$ transition in ^{87}Rb that we addressed, the allowed dipole cascaded decay may generate correlated photons at 1529 nm and 780 nm via the $5P_{3/2}$ state and at 1476 nm and 795 nm via the $5P_{1/2}$ state. This could open up a possibility to develop a fiber-integrated source of correlated photon-pairs relevant to telecommunications (as 1529 nm is a useful wavelength in the telecom C-band) and quantum information applications.

Typically in a MOT-ONF system, less than 10 atoms contribute to the signal. This could be improved by trapping atoms in a dipole array close to the ONF. For fiber-based traps, one of the crucial and non-trivial parameters is the polarization of the fiber-guided light in the evanescent field on which the trapping potential depends. As such the first important step to optimize fiber-based traps was to be able to determine and control the polarization of the fiber-guided mode at the ONF. For this we adopted a method of polarization control of the HE_{11} mode [97], based on imaging scattered light (from the nanofiber) with a single lens. Notably, the use of a single imaging lens to observe the angular distribution of Rayleigh scattered light emitted from the nanofiber is a very useful technique for applications in situations with limited optical access, like in our case.

With accurate polarization control, we were able to study the transition rate of a single-frequency two-photon excitation process in ^{87}Rb atoms as a function of helicity of the excitation field. We first developed a theoretical framework for the transition rate in an $S \rightarrow S$ transition, which dictates a quadratic dependence on the helicity of the excitation light field. While the transition rate is extinguished for paraxial excitation with circularly polarized light, the transition rate is always non-zero owing to the finite contribution of the longitudinal field in the ONF-guided field. The transition rate, however, is minimized for the ONF-guided excitation field with quasi-circular

polarization. These findings could potentially find applications in atom-based hybrid quantum technologies where full control of quantum state selection is vital and could open new ways of selecting transition pathways for frequency references and compact optical clocks [157], novel fiber-based trapping schemes [28] and transfer of spin or orbital angular momentum between light and atoms [130, 174]. State-selective excitations [119] and spin-orbit coupling [225] could be further explored in the context of the chiral nature of the evanescent field interactions.

Bringing our focus back to the implementation of a nanofiber trap, we implemented a 1D lattice trap for ^{87}Rb atoms near the nanofiber surface using a combination of a red-detuned counter-propagating light field and a blue-detuned traveling light field in the fiber-guided HE_{11} mode. The presence of the inherent elliptical polarization of the fiber modes coupled with the lack of a suitable magic-wavelength for ^{87}Rb for use in nanofiber-based traps, due to either being too close to resonant transitions causing heating or due to absorption by silica, makes it difficult to implement a deep trap at submicron distances from the fiber surface. Loading of atoms in such a shallow trap is not an easy problem to optimize manually. We used a machine learner optimizer that leverages deep learning methods to increase the number of trapped ^{87}Rb atoms by 50% in a proof-of-principle experiment. We developed a theoretical model of the absorption of a fiber-guided probe by atoms trapped in the evanescent field of the nanofiber that enabled us to determine the number and average temperature of the trapped atoms. We expect the number to be improved further by using a new ONF in the experimental setup and by increasing the number of experimental parameters given to the ML algorithm for optimization. In addition, we estimated the trap lifetime, an important parameter for many applications, to be around 26 ms which could as well be improved by an appropriate choice of cost function. Investigations of the capabilities of this setup are planned, including optimizing the loading of atoms for collective atom-light interactions which requires a large optical depths and appropriate phase-matching, and increasing the number of nearest-neighbor interactions in a 1D lattice of highly-excited Rydberg atoms. We envision that this will be feasible with the obtained number of atoms trapped in the 1D array.

Rydberg atoms with their large electric dipole moments and long lifetime have been the subject of intense research for their potential use in quantum information processing and fundamental light-matter interaction studies. Rydberg atoms are versatile systems for many-body physics studies owing to their strong dipole-dipole interactions [226], for example numerical study on thermal-effects on a Rydberg blockaded atomic array showing thermalization gives insights into many-body quantum thermodynamics [227]. Toward the integration of Rydberg atoms with an optical nanofiber system, our unit has already demonstrated the generation of cold Rydberg atoms close to a nanofiber surface [228]. In the vicinity of a surface, surface interactions plays a critical role. It is advantageous to control the distance of Rydberg atoms from the nanofiber surface to avoid ion deposition and our implementation of fiber trap serves as a stepping stone for this goal. Furthermore with a new, thinner ONF (diameter $\sim$350 nm) installed in the MOT chamber, allowing for higher relative intensities of the blue-detuned trapping field, we should be able to push the trapping sites further away reducing the surface effects and the ion deposition.

Aside from the endeavors to integrate the Rydberg atoms to the ONF, the possibil-

ity of developing correlated photon pairs at wavelengths relevant to telecommunications and atomic transitions in the nanofiber-atom system needs to be further investigated. A four-wave mixing process in an atomic medium is an efficient way to generate correlated photon pairs in well-defined modes. We have performed preliminary investigations in a FWM process involving two-photon excitations with 778 nm light that may have potentials for application in a nanofiber system. With the availability of a Rb vapor cell that can withstand temperatures up to 200°C, we would be able to achieve a regime of high atomic density required to study this transition further. The LG beam generation could also be improved by using Zernike polynomials and sophisticated algorithms like the Gerchberg-Saxton algorithm. Entanglement of orbital angular momentum states is worth exploring for its promising potential toward high-density quantum information applications. Toward the study of correlated photon pair generation, further investigations in ONF-mediated 993 nm two-photon transition in cold Rb atoms are also warranted. The ability to detect the infrared emissions (1324 nm and 1367 nm) with recently purchased infrared detectors should allow us to explore the coherence aspects of the transition.

In another direction, the strong atom-light coupling due to tightly confined mode volume of the guided mode could be substantially enhanced with the addition of a moderate finesse fiber in-line cavity, thereby improving single atom optical depth. Coupled with fiber-based trapping this could open routes toward cavity-enhanced fiber-connected quantum nodes. With this in mind, our unit has been studying and fabricating different nanofiber-cavity structures with focused ion-beam (FIB) milling [65, 229] as a new tool in the ONF-based toolbox for atom manipulation and control.

Bibliography

[1] J. P. Dowling and G. J. Milburn, *Quantum technology: the second quantum revolution*, Phil. Trans. R. Soc. Lond. A **361**, 1655–1674 (2003).

[2] H. J. Kimble, Y. Levin, A. B. Matsko, K. S. Thorne, and S. P. Vyatchanin, *Conversion of conventional gravitational-wave interferometers into quantum nondemolition interferometers by modifying their input and/or output optics*, Phys. Rev. D **65**, 022002 (2001).

[3] N. Gisin and R. Thew, *Quantum communication*, Nat. Photon. **1**, 165–171 (2007).

[4] T. D. Ladd, F. Jelezko, R. Laflamme, Y. Nakamura, C. Monroe, and J. L. O'Brien, *Quantum computers*, Nature **464**, 45–53 (2010).

[5] H. J. Kimble, *The quantum internet*, Nature **453**, 1023–1030 (2008).

[6] E. Knill, R. Laflamme, and G. J. Milburn, *A scheme for efficient quantum computation with linear optics*, Nature **409**, 46–52 (2001).

[7] P. S. Jessen, I. H. Deutsch, and R. Stock, *Quantum information processing with trapped neutral atoms*, Quantum Inf. Process. **3**, 91–103 (2004).

[8] J. I. Cirac and P. Zoller, *Quantum Computations with cold trapped ions*, Phys. Rev. Lett. **74**, 4091–4094 (1995).

[9] J. Wrachtrup and F. Jelezko, *Processing quantum information in diamond*, J. Phys.: Condens. Mat. **18**, S807–S824 (2006).

[10] A. Reiserer and G. Rempe, *Cavity-based quantum networks with single atoms and optical photons*, Rev. Mod. Phys. **87**, 1379–1418 (2015).

[11] J. Clarke and F. K. Wilhelm, *Superconducting quantum bits*, Nature **453**, 1031–1042 (2008).

[12] K.-A. Suominen. *Physical implementation of large-scale quantum computation.* In G. Rozenberg, T. Bäck, and J. N. Kok, editors, *Handbook of Natural Computing*, pages 1493–1520. Springer Berlin Heidelberg, (2012).

[13] H. J. Kimble, *Strong interactions of single atoms and photons in cavityQED*, Phys. Scripta **T76**, 127 (1998).

[14] J. McKeever, A. Boca, A. D. Boozer, J. R. Buck, and H. J. Kimble, *Experimental realization of a one-atom laser in the regime of strong coupling*, Nature **425**, 268–271 (2003).

[15] V. Gomer, B. Ueberholz, S. Knappe, F. Strauch, D. Frese, and D. Meschede, *Decoding the dynamics of a single trapped atom from photon correlations*, Appl. Phys. B: Lasers O. **67**, 689–697 (1998).

[16] T. Wilk, S. Webster, A. Kuhn, and G. Rempe, *Single-atom single-photon quantum interface*, Science **317**, 488–490 (2007).

[17] B. Julsgaard, J. Sherson, J. I. Cirac, J. Fiurášek, and E. S. Polzik, *Experimental demonstration of quantum memory for light*, Nature **432**, 482–486 (2004).

[18] C. W. Chou, S. V. Polyakov, A. Kuzmich, and H. J. Kimble, *Single-photon generation from stored excitation in an atomic ensemble*, Phys. Rev. Lett. **92**, 213601 (2004).

[19] M. Fleischhauer, A. Imamoglu, and J. P. Marangos, *Electromagnetically induced transparency: Optics in coherent media*, Rev. Mod. Phys. **77**, 633–673 (2005).

[20] D. F. Phillips, A. Fleischhauer, A. Mair, R. L. Walsworth, and M. D. Lukin, *Storage of light in atomic vapor*, Phys. Rev. Lett. **86**, 783–786 (2001).

[21] N. B. Phillips, A. V. Gorshkov, and I. Novikova, *Optimal light storage in atomic vapor*, Phys. Rev. A **78**, 023801 (2008).

[22] K. Cox, V. I. Yudin, A. V. Taichenachev, and E. E. Novikova, I.and Mikhailov, *Measurements of the magnetic field vector using multiple electromagnetically induced transparency resonances in Rb vapor*, Phys. Rev. A **83**, 015801 (2011).

[23] V. Bendkowsky, B. Butscher, J. Nipper, J. P. Shaffer, R. Löw, and T. Pfau, *Observation of ultralong-range Rydberg molecules*, Nature **458**, 1005–1008 (2009).

[24] M. D. Lukin, M. Fleischhauer, R. Cote, L. M. Duan, D. Jaksch, J. I. Cirac, and P. Zoller, *Dipole blockade and quantum information processing in mesoscopic atomic ensembles*, Phys. Rev. Lett. **87**, 037901 (2001).

[25] V. V. Klimov and M. Ducloy, *Spontaneous emission rate of an excited atom placed near a nanofiber*, Phys. Rev. A **69**, 013812 (2004).

[26] F. Le Kien, S. Dutta Gupta, V. I. Balykin, and K. Hakuta, *Spontaneous emission of a cesium atom near a nanofiber: Efficient coupling of light to guided modes*, Phys. Rev. A **72**, 032509 (2005).

[27] F. Le Kien, V. I. Balykin, and K. Hakuta, *Atom trap and waveguide using a two-color evanescent light field around a subwavelength-diameter optical fiber*, Phys. Rev. A **70**, 063403 (2004).

[28] E. Vetsch, D. Reitz, G. Sagué, R. Schmidt, S. T. Dawkins, and A. Rauschenbeutel, *Optical interface created by laser-cooled atoms trapped in the evanescent field surrounding an optical nanofiber*, Phys. Rev. Lett. **104**, 203603 (2010).

[29] A. Dareau, Y. Meng, P. Schneeweiss, and A. Rauschenbeutel, *Observation of ultrastrong spin-motion coupling for cold atoms in optical microtraps*, Phys. Rev. Lett. **121**, 253603 (2018).

[30] N. V. Corzo, J. Raskop, A. Chandra, A. S. Sheremet, B. Gouraud, and J. Laurat, *Waveguide-coupled single collective excitation of atomic arrays*, Nature **566**, 359–362 (2019).

[31] A. Asenjo-Garcia, M. Moreno-Cardoner, A. Albrecht, H. J. Kimble, and D. E. Chang, *Exponential improvement in photon storage fidelities using subradiance and "selective radiance" in atomic arrays*, Phys. Rev. X **7**, 031024 (2017).

[32] L. Tong, R. R. Gattass, J. B. Ashcom, S. He, J. Lou, M. Shen, I. Maxwell, and E. Mazur, *Subwavelength-diameter silica wires for low-loss optical wave guiding*, Nature **426**, 816–819 (2003).

[33] G. Brambilla, V. Finazzi, and D. J. Richardson, *Ultra-low-loss optical fiber nanotapers*, Opt. Express **12**, 2258 (2004).

[34] J. M. Ward, A. Maimaiti, V. H. Le, and S. Nic Chormaic, *Contributed Review: Optical micro- and nanofiber pulling rig*, Rev. Sci. Instrum. **85**, 111501 (2014).

[35] M. Sumetsky, *Optical fiber microcoil resonator*, Opt. Express **12**, 2303–2316 (2004).

[36] Z. Tian, S. S.-H. Yam, J. Barnes, W. Bock, P. Greig, J. M. Fraser, H.-P. Loock, and R. D. Oleschuk, *Refractive index sensing with Mach–Zehnder interferometer based on concatenating two single-mode fiber tapers*, IEEE Photon. Tech. Lett. **20**, 626–628 (2008).

[37] M. Belal, Z. Song, Y. Jung, G. Brambilla, and T. P. Newson, *Optical fiber microwire current sensor*, Opt. Lett. **35**, 3045–3047 (2010).

[38] A. K. Patnaik, J. Q. Liang, and K. Hakuta, *Slow light propagation in a thin optical fiber via electromagnetically induced transparency*, Phys. Rev. A **66**, 063808 (2002).

[39] F. Le Kien, V. I. Balykin, and K. Hakuta, *Scattering of an evanescent light field by a single cesium atom near a nanofiber*, Phys. Rev. A **73**, 013819 (2006).

[40] F. Le Kien, V. I. Balykin, and K. Hakuta, *Angular momentum of light in an optical nanofiber*, Phys. Rev. A **73**, 053823 (2006).

[41] F. Le Kien, V. I. Balykin, and K. Hakuta, *Light-induced force and torque on an atom outside a nanofiber*, Phys. Rev. A **74**, 033412 (2006).

[42] L. Russell, D. A. Gleeson, V. G. Minogin, and S. Nic Chormaic, *Spectral distribution of atomic fluorescence coupled into an optical nanofibre*, J. Phys. B: At. Mol. Opt. **42**, 185006 (2009).

[43] V. G. Minogin and S. Nic Chormaic, *Manifestation of the van der Waals surface interaction in the spontaneous emission of atoms into an optical nanofiber*, Laser Phys. **20**, 32–37 (2010).

[44] M. C. Frawley, S. Nic Chormaic, and V. G. Minogin, *The van der Waals interaction of an atom with the convex surface of a nanocylinder*, Phys. Scripta **85**, 058103 (2012).

[45] F. Le Kien and A. Rauschenbeutel, *Anisotropy in scattering of light from an atom into the guided modes of a nanofiber*, Phys. Rev. A **90**, 023805 (2014).

[46] A. V. Masalov and V. G. Minogin, *Spontaneous decay rates of the hyperfine structure atomic states into an optical nanofiber*, J. Exp. Theor. Phys. **118**, 714–722 (2014).

[47] K. P. Nayak, P. N. Melentiev, M. Morinaga, F. Le Kien, V. I. Balykin, and K. Hakuta, *Optical nanofiber as an efficient tool for manipulating and probing atomic fluorescence*, Opt. Express **15**, 5431–5438 (2007).

[48] K. P. Nayak, M. Das, F. Le Kien, and K. Hakuta, *Spectroscopy of near-surface atoms using an optical nanofiber*, Opt. Commun. **285**, 4698–4704 (2012).

[49] S. M. Spillane, G. S. Pati, K. Salit, M. Hall, P. Kumar, R. G. Beausoleil, and M. S. Shahriar, *Observation of nonlinear optical interactions of ultralow levels of light in a tapered optical nanofiber embedded in a hot rubidium vapor*, Phys. Rev. Lett. **100**, 233602 (2008).

[50] S. M. Hendrickson, M. M. Lai, T. B. Pittman, and J. D. Franson, *Observation of two-photon absorption at low power levels using tapered optical fibers in rubidium vapor*, Phys. Rev. Lett. **105**, 173602 (2010).

[51] M. J. Morrissey, K. Deasy, Y. Wu, S. Chakrabarti, and S. Nic Chormaic, *Tapered optical fibers as tools for probing magneto-optical trap characteristics*, Rev. Sci. Instrum. **80**, 053102 (2009).

[52] M. Das, A. Shirasaki, K. P. Nayak, M. Morinaga, F. Le Kien, and K. Hakuta, *Measurement of fluorescence emission spectrum of few strongly driven atoms using an optical nanofiber*, Opt. Express **18**, 17154–17164 (2010).

[53] K. P. Nayak and K. Hakuta, *Single atoms on an optical nanofibre*, New J. Phys. **10** (2008).

[54] J. A. Grover, P. Solano, L. A. Orozco, and S. L. Rolston, *Photon-correlation measurements of atomic-cloud temperature using an optical nanofiber*, Phys. Rev. A **92**, 013850 (2015).

[55] R. Kumar, V. Gokhroo, K. Deasy, and S. Nic Chormaic, *Autler-Townes splitting via frequency up-conversion at ultralow-power levels in cold Rb87 atoms using an optical nanofiber*, Phys. Rev. A **91**, 053842 (2010).

[56] R. Kumar, V. Gokhroo, and S. Nic Chormaic, *Multi-level cascaded electromagnetically induced transparency in cold atoms using an optical nanofibre interface*, New J. Phys. **17**, 123012 (2015).

[57] C. Sayrin, C. Clausen, B. Albrecht, P. Schneeweiss, and A. Rauschenbeutel, *Storage of fiber-guided light in a nanofiber-trapped ensemble of cold atoms*, Optica **2**, 353–356 (2015).

[58] D. E. Chang, L. Jiang, A. V. Gorshkov, and H. J. Kimble, *Cavity QED with atomic mirrors*, New J. Phys. **14**, 063003 (2012).

[59] J. Busch and A. Beige, *Generating single-mode behavior in fiber-coupled optical cavities*, Phys. Rev. A **82**, 053824 (2010).

[60] E. Kyoseva, A. Beige, and L. C. Kwek, *Coherent cavity networks with complete connectivity*, New J. Phys. **14**, 023023 (2012).

[61] F. Le Kien and K. Hakuta, *Cavity-enhanced channeling of emission from an atom into a nanofiber*, Phys. Rev. A **80**, 053826 (2009).

[62] K. P. Nayak, F. Le Kien, Y. Kawai, K. Hakuta, K. Nakajima, H. T. Miyazaki, and Y. Sugimoto, *Cavity formation on an optical nanofiber using focused ion beam milling technique*, Opt. Express **19**, 14040–14050 (2011).

[63] C. Wuttke, M. Becker, S. Brückner, M. Rothhardt, and A. Rauschenbeutel, *Nanofiber Fabry-Perot microresonator for nonlinear optics and cavity quantum electrodynamics*, Opt. Lett. **37**, 1949–1951 (2012).

[64] S. Kato and T. Aoki, *Strong coupling between a trapped single atom and an all-fiber cavity*, Phys. Rev. Lett. **115**, 093603 (2015).

[65] W. Li, J. Du, V. G. Truong, and S. Nic Chormaic, *Optical nanofiber-based cavity induced by periodic air-nanohole arrays*, Applied Phys. Lett. **110**, 253102 (2017).

[66] P. Schneeweiss, S. Zeiger, T. Hoinkes, A. Rauschenbeutel, and J. Volz, *Fiber ring resonator with a nanofiber section for chiral cavity quantum electrodynamics and multimode strong coupling*, Opt. Lett. **42**, 85–88 (2017).

[67] S. K. Ruddell, K. E. Webb, I. Herrera, A. S. Parkins, and M. D. Hoogerland, *Collective strong coupling of cold atoms to an all-fiber ring cavity*, Optica **4**, 576–579 (2017).

[68] N. V. Corzo, B. Gouraud, A. Chandra, A. Goban, A. S. Sheremet, D. V. Kupriyanov, and J. Laurat, *Large Bragg reflection from one-dimensional chains of trapped atoms near a nanoscale waveguide*, Phys. Rev. Lett. **117**, 133603 (2016).

[69] H. L. Sørensen, J. B. Béguin, K. W. Kluge, I. Iakoupov, A. S. Sørensen, J. H. Müller, E. S. Polzik, and J. Appel, *Coherent backscattering of light off one-dimensional atomic strings*, Phys. Rev. Lett. **117**, 133604 (2016).

[70] P. Solano, P. Barberis-Blostein, F. K. Fatemi, L. A. Orozco, and S. L. Rolston, *Super-radiance reveals infinite-range dipole interactions through a nanofiber*, Nat. Commun. **8**, 1857 (2017).

[71] Y. Zhou, Z. Chen, and J.-T. Shen, *Single-photon superradiant emission rate scaling for atoms trapped in a photonic waveguide*, Phys. Rev. A **95**, 043832 (2017).

[72] D. F. Kornovan, N. V. Corzo, J. Laurat, and A. S. Sheremet, *Extremely subradiant states in a periodic one-dimensional atomic array*, Phys. Rev. A **100**, 063832 (2019).

[73] A. Kuzmich, W. P. Bowen, A. D. Boozer, A. Boca, C. W. Chou, L.-M. Duan, and H. J. Kimble, *Generation of nonclassical photon pairs for scalable quantum communication with atomic ensembles*, Nature **423**, 731–734 (2003).

[74] T. Chanelière, D. N. Matsukevich, S. D. Jenkins, T. A. B. Kennedy, M. S. Chapman, and A. Kuzmich, *Quantum telecommunication based on atomic cascade transitions*, Phys. Rev. Lett. **96**, 093604 (2006).

[75] L. M. Duan, M. D. Lukin, J. I. Cirac, and P. Zoller, *Long-distance quantum communication with atomic ensembles and linear optics*, Nature **414**, 413–418 (2001).

[76] E. S. Fry and R. C. Thompson, *Experimental test of local hidden-variable theories*, Phys. Rev. Lett. **37**, 465–468 (1976).

[77] A. Aspect, P. Grangier, and G. Roger, *Experimental tests of realistic local theories via Bell's theorem*, Phys. Rev. Lett. **47**, 460–463 (1981).

[78] G. Weihs, T. Jennewein, C. Simon, H. Weinfurter, and A. Zeilinger, *Violation of Bell's inequality under strict Einstein locality conditions*, Phys. Rev. Lett. **81**, 5039–5043 (1998).

[79] G. Leuchs and M. Sondermann, *Time-reversal symmetry in optics*, Phys. Scripta **85**, 058101 (2012).

[80] A. K. Ekert, *Quantum cryptography based on Bell's theorem*, Phys. Rev. Lett. **67**, 661–663 (1991).

[81] N. Gisin, G. Ribordy, W. Tittel, and H. Zbinden, *Quantum cryptography*, Rev. Mod. Phys. **74**, 145–195 (2002).

[82] C. F. McCormick, V. Boyer, E. Arimondo, and P. D. Lett, *Strong relative intensity squeezing by four-wave mixing in rubidium vapor*, Opt. Lett. **32**, 178–180 (2007).

[83] T. Horrom, I. Novikova, and E. E. Mikhailov, *All-atomic source of squeezed vacuum with full pulse-shape control*, J. Phys. B. **45**, 124015 (2012).

[84] A. I. Lvovsky. *Squeezed Light*, chapter 5, pages 121–163. John Wiley Sons, Ltd., (2015).

[85] L. Barsotti, J. Harms, and R. Schnabel, *Squeezed vacuum states of light for gravitational wave detectors*, Rep. Prog. Phys. **82**, 016905 (2018).

[86] M. K. Tey, Z. Chen, S. A. Aljunid, B. Chng, F. Huber, G. Maslennikov, and C. Kurtsiefer, *Strong interaction between light and a single trapped atom without the need for a cavity*, Nat. Phys. **4**, 924–927 (2008).

[87] H. Katori, T. Ido, and M. Kuwata-Gonokami, *Optimal design of dipole potentials for efficient loading of Sr atoms*, J. Phys. Soc. JPN **68**, 2479–2482 (1999).

[88] B. Arora, M. S. Safronova, and C. W. Clark, *Magic wavelengths for the np−ns transitions in alkali-metal atoms*, Phys. Rev. A **76**, 052509 (2007).

[89] B. Arora and B. K. Sahoo, *State-insensitive trapping of Rb atoms: Linearly versus circularly polarized light*, Phys. Rev. A **86**, 033416 (2012).

[90] S. Singh, B. K. Sahoo, and B. Arora, *Magnetic-sublevel-independent magic wavelengths: Application to Rb and Cs atoms*, Phys. Rev. A **93**, 063422 (2016).

[91] N. Lundblad, M. Schlosser, and J. V. Porto, *Experimental observation of magic-wavelength behavior of* ^{87}Rb *atoms in an optical lattice*, Phys. Rev. A **81**, 031611 (2010).

[92] A. Derevianko, *Theory of magic optical traps for Zeeman-insensitive clock transitions in alkali-metal atoms*, Phys. Rev. A **81**, 051606 (2010).

[93] F. Le Kien, V. I. Balykin, and K. Hakuta, *State-insensitive trapping and guiding of cesium atoms using a two-color evanescent field around a subwavelength-diameter fiber*, J. Phys. Soc. JPN **74**, 910–917 (2005).

[94] C. Lacroûte, K. S. Choi, A. Goban, D. J. Alton, D. Ding, N. P. Stern, and H. J. Kimble, *A state-insensitive, compensated nanofiber trap*, New J. Phys. **14**, 023056 (2012).

[95] S. Singh, B. Arora, B. K. Sahoo, and Y.-M. Yu, *Magic wavelengths for optical-lattice based Cs and Rb active clocks*, Atoms **8**, 79 (2020).

[96] J. Lee, J. A. Grover, J. E. Hoffman, L. A. Orozco, and S. L. Rolston, *Inhomogeneous broadening of optical transitions of 87Rb atoms in an optical nanofiber trap*, J. Phys. B: At. Mol. Opt. **48**, 165004 (2015).

[97] G. Tkachenko, F. Lei, and S. Nic Chormaic, *Polarisation control for optical nanofibres by imaging through a single lens*, J. Opt. **21**, 125604 (2019).

[98] C. Cohen-Tannoudji, J. Dupont-Roc, and G. Grynberg, *Atom–photon interactions: Basic processes and applications*, American Association of Physics Teachers (1993).

[99] H. J. Metcalf and P. van der Straten, *Laser cooling and trapping*, Springer-Verlag, New York (1999).

[100] A. R. Edmonds, *Angular momentum in quantum mechanics*, New Jersey: Princeton University Press (1974).

[101] D. A. Varshalovich, A. N. Moskalev, and V. K. Khersonskii, *Quantum theory of angular momentum*, Singapore: World Scientific Publishing (2008).

[102] I. I. Sobelman, *Atomic spectra and radiative transitions*, Springer Science & Business Media (2012).

[103] R. Loudon, *The quantum theory of light*, OUP Oxford (2000).

[104] F. Le Kien, P. Schneeweiss, and A. Rauschenbeutel, *Dynamical polarizability of atoms in arbitrary light fields: general theory and application to cesium*, Eur. Phys. J. D **67**, 1–16 (2013).

[105] F. Atoneche and A. Kastberg, *Simplified approach for quantitative calculations of optical pumping*, Eur. J. Phys. **38**, 045703 (2017).

[106] D. A. Steck. *Rubidium 87 D line data*, (2001).

[107] L. Russell, K. Deasy, M. J. Daly, M. J. Morrissey, and S. Nic Chormaic, *Sub-Doppler temperature measurements of laser-cooled atoms using optical nanofibres*, Meas. Sci. Technol. **23**, 015201 (2011).

[108] L. Russell, R. Kumar, V. B. Tiwari, and S. Nic Chormaic, *Measurements on release–recapture of cold 85Rb atoms using an optical nanofibre in a magneto-optical trap*, Opt. Commun. **309**, 313–317 (2013).

[109] L. Russell, R. Kumar, V. B. Tiwari, and S. Nic Chormaic, *Investigation of a 85Rb dark magneto-optical trap using an optical nanofibre*, Meas. Sci. Technol. **25**, 055203 (2014).

[110] R. Kumar, V. Gokhroo, K. Deasy, A. Maimaiti, M. C. Frawley, C. Phelan, and S. Nic Chormaic, *Interaction of laser-cooled 87Rb atoms with higher order modes of an optical nanofibre*, New J. Phys. **17**, 013026 (2015).

[111] R. Kumar, V. Gokhroo, V. B. Tiwari, and S. Nic Chormaic, *Temperature measurement of cold atoms using transient absorption of a resonant probe through an optical nanofibre*, J. Opt. **18**, 115401 (2016).

[112] K. S. Rajasree. *Rydberg excitation and other multiphoton processes in cold rubidium atoms near an optical nanofibre*. PhD thesis, Okinawa Institute of Science and Technology, (2020).

[113] A. W. Snyder and J. Love, *Optical waveguide theory*, Springer Science & Business Media (2012).

[114] F. Le Kien, T. Busch, V. G. Truong, and S. Nic Chormaic, *Higher-order modes of vacuum-clad ultrathin optical fibers*, Phys. Rev. A **96** (2017).

[115] T. Nieddu. *Optical nanofibers for multiphoton processes and selective mode interactions with rubidium.* PhD thesis, Okinawa Institute of Science and Technology, (2019).

[116] S. P. Mekhail. *Optical fiber probes for in-vivo neuronal compressive microendoscopy and mode analysis in nanofibers.* PhD thesis, Okinawa Institute of Science and Technology, (2019).

[117] M. Sadgrove, M. Sugawara, Y. Mitsumori, and K. Edamatsu, *Polarization response and scaling law of chirality for a nanofibre optical interface*, Sci. Rep. **7**, 17085 (2017).

[118] R. Mitsch, C. Sayrin, B. Albrecht, P. Schneeweiss, and A. Rauschenbeutel, *Quantum state-controlled directional spontaneous emission of photons into a nanophotonic waveguide*, Nat. Commun. **5**, 5713 (2014).

[119] C. Sayrin, C. Junge, R. Mitsch, B. Albrecht, D. O'Shea, P. Schneeweiss, J. Volz, and A. Rauschenbeutel, *Nanophotonic optical isolator controlled by the internal state of cold atoms*, Phys. Rev. X **5**, 041036 (2015).

[120] A. Goban, K. S. Choi, D. J. Alton, D. Ding, C. Lacroûte, M. Pototschnig, T. Thiele, N. P. Stern, and H. J. Kimble, *Demonstration of a state-insensitive, compensated nanofiber trap*, Phys. Rev. Lett. **109**, 033603 (2012).

[121] E. Vetsch, S. T. Dawkins, R. Mitsch, D. Reitz, P. Schneeweiss, and A. Rauschenbeutel, *Nanofiber-based optical trapping of cold neutral atoms*, IEEE J. Sel. Top. Quant. **18**, 1763–1770 (2012).

[122] T. Ray, R. K. Gupta, V. Gokhroo, J. L. Everett, T. Nieddu, K. S. Rajasree, and S. Nic Chormaic, *Observation of the ^{87}Rb $5S_{1/2}$ to $4D_{3/2}$ electric quadrupole transition at 516.6 nm mediated via an optical nanofibre*, New J. Phys. **22**, 062001 (2020).

[123] F. Le Kien, T. Ray, T. Nieddu, T. Busch, and S. Nic Chormaic, *Enhancement of the quadrupole interaction of an atom with the guided light of an ultrathin optical fiber*, Phys. Rev. A **97**, 013821 (2018).

[124] J. D. Jackson, *Classical electrodynamics*, Wiley, New York, 3rd edition (1999).

[125] R. C. Hilborn, *Einstein coefficients, cross sections, f values, dipole moments, and all that*, Am. J. Phys. **50**, 982–986 (1982).

[126] B. Sayer, R. Wang, J. C. Jeannet, and M. Sassi, *Absorption measurements of quadrupole transition probabilities 6S-nD in caesium vapour*, J. Phys. B: At. Mol. Opt. **4**, L20–L23 (1971).

[127] C. Camy-Peyret, J. M. Flaud, L. Delbouille, G. Roland, J. W. Brault, and L. Testerman, *Quadrupole transitions of the* $1 \leftarrow 0$ *band of* N_2 *observed in a high resolution atmospheric spectrum*, J. Phys. Lett.: Paris **42**, 279–283 (1981).

[128] S. Tojo, M. Hasuo, and T. Fujimoto, *Absorption enhancement of an electric quadrupole transition of cesium atoms in an evanescent field*, Phys. Rev. Lett. **92**, 053001 (2004).

[129] B. M. Roberts, V. A. Dzuba, and V. V. Flambaum, *Nuclear-spin-dependent parity nonconservation in* S-$D_{5/2}$ *and* S-$D_{3/2}$ *transitions*, Phys. Rev. A **89**, 012502 (2014).

[130] M. Babiker, C. R. Bennett, D. L. Andrews, and L. C. Dávila Romero, *Orbital angular momentum exchange in the interaction of twisted light with molecules*, Phys. Rev. Lett. **89**, 143601 (2002).

[131] S. Tojo, T. Fujimoto, and M. Hasuo, *Precision measurement of the oscillator strength of the cesium* $6^2S_{1/2} \rightarrow 5^2D_{5/2}$ *electric quadrupole transition in propagating and evanescent wave fields*, Phys. Rev. A **71**, 012507 (2005).

[132] E. A. Chan, S. A. Aljunid, G. Adamo, N. I. Zheludev, M. Ducloy, and D. Wilkowski, *Coupling of atomic quadrupole transitions with resonant surface plasmons*, Phys. Rev. A **99**, 063801 (2019).

[133] S. Pucher, P. Schneeweiss, A. Rauschenbeutel, and A. Dareau, *Lifetime measurement of the cesium* $5\,^2D_{5/2}$ *state*, Phys. Rev. A **101**, 042510 (2020).

[134] V. E. Lembessis and M. Babiker, *Enhanced quadrupole effects for atoms in optical vortices*, Phys. Rev. Lett. **110**, 083002 (2013).

[135] K. Shibata, S. Tojo, and D. Bloch, *Excitation enhancement in electric multipole transitions near a nanoedge*, Opt. Express **25**, 9476 (2017).

[136] K. Sakai, T. Yamamoto, and K. Sasaki, *Nanofocusing of structured light for quadrupolar light-matter interactions*, Sci. Rep. **8**, 7746 (2018).

[137] U. Teppner and P. Zimmermann, *Lifetime measurements of the lowest* ^2D*-states in K I and Rb I using electric quadrupole excitation*, Astron. Astrophys. **64**, 215–217 (1978).

[138] J. Nilsen and J. Marling, *Oscillator strengths of the first forbidden lines of rubidium*, J. Quant. Spectrosc. Radiat. Transf. **20**, 327 – 329 (1978).

[139] D. Tong, S. M. Farooqi, E. G. M. van Kempen, Z. Pavlovic, J. Stanojevic, R. Côté, E. E. Eyler, and P. L. Gould, *Observation of electric quadrupole transitions to Rydberg nd states of ultracold rubidium atoms*, Phys. Rev. A **79**, 052509 (2009).

[140] F. Ponciano-Ojeda, S. Hernández-Gómez, O. López-Hernández, C. Mojica-Casique, R. Colín-Rodríguez, F. Ramírez-Martínez, J. Flores-Mijangos, D. Sahagún, R. Jáuregui, and J. Jiménez-Mier, *Observation of the* $5P_{3/2} \rightarrow 6P_{3/2}$ *electric-dipole-forbidden transition in atomic rubidium using optical-optical double-resonance spectroscopy*, Phys. Rev. A **92**, 042511 (2015).

[141] C. Mojica-Casique, F. Ponciano-Ojeda, S. Hernández-Gómez, O. López-Hernández, J. Flores-Mijangos, F. Ramírez-Martínez, D. Sahagún, R. Jáuregui, and J. Jiménez-Mier, *Control of electronic magnetic state population via light polarization in the* $5P_{3/2} \rightarrow 6P_{3/2}$ *electric quadrupole transition in atomic rubidium*, J. Phys. B: At. Mol. Opt. **50**, 025003 (2016).

[142] B. Shore, *The theory of coherent atomic excitation*, Taylor & Francis (1991).

[143] H. S. Moon, H. Y. Ryu, S. H. Lee, and H. S. Suh, *Precision spectroscopy of Rb atoms using single comb-line selected from fiber optical frequency comb*, Opt. Express **19**, 15855–15863 (2011).

[144] R. Roy, P. C. Condylis, Y. J. Johnathan, and B. Hessmo, *Atomic frequency reference at 1033 nm for ytterbium (Yb)-doped fiber lasers and applications exploiting a rubidium (Rb)* $5S_{1/2}$ *to* $4D_{5/2}$ *one-colour two-photon transition*, Opt. Express **25**, 7960–7969 (2017).

[145] T. Nieddu, T. Ray, K. S. Rajasree, R. Roy, and S. Nic Chormaic, *Simple, narrow, and robust atomic frequency reference at 993 nm exploiting the rubidium (Rb)* $5S_{1/2}$ *to* $6S_{1/2}$ *transition using one-color two-photon excitation*, Opt. Express **27**, 6528–6535 (2019).

[146] M. M. Salour, *Ultra-high-resolution two-photon spectroscopy in atomic and molecular vapors*, Ann. Phys.: New York **111**, 364 – 503 (1978).

[147] M. S. Safronova and U. I. Safronova, *Critically evaluated theoretical energies, lifetimes, hyperfine constants, and multipole polarizabilities in Rb87*, Phys. Rev. A **83**, 052508 (2011).

[148] E. Gomez, F. Baumer, A. D. Lange, G. D. Sprouse, and L. A. Orozco, *Lifetime measurement of the* $6S$ *level of rubidium*, Phys. Rev. A **72**, 012502 (2005).

[149] J. E. Simsarian, L. A. Orozco, G. D. Sprouse, and W. Z. Zhao, *Lifetime measurements of the* $7P$ *levels of atomic francium*, Phys. Rev. A **57**, 2448–2458 (1998).

[150] R. F. Gutterres, C. Amiot, A. Fioretti, C. Gabbanini, M. Mazzoni, and O. Dulieu, *Determination of the* ^{87}Rb $5P$ *state dipole matrix element and radiative lifetime from the photoassociation spectroscopy of the* Rb_2 $0_g^-(P_{3/2})$ *long-range state*, Phys. Rev. A **66**, 024502 (2002).

[151] V. A. Dzuba, V. V. Flambaum, and B. Roberts, *Calculation of the parity-violating 5S-6S E1 amplitude in the rubidium atom*, Phys. Rev. A **86**, 062512 (2012).

[152] S. Okaba, T. Takano, F. Benabid, T. Bradley, L. Vincetti, Z. Maizelis, V. Yampol'skii, F. Nori, and H. Katori, *Lamb-Dicke spectroscopy of atoms in a hollow-core photonic crystal fibre*, Nat. Commun. **5**, 4096 (2014).

[153] K. S. Rajasree, R. K. Gupta, V. Gokhroo, F. Le Kien, T. Nieddu, T. Ray, S. Nic Chormaic, and G. Tkachenko, *Spin selection in single-frequency two-photon excitation of alkali-metal atoms*, Phys. Rev. Research **2**, 033341 (2020).

[154] K. Shimoda, *High-resolution laser spectroscopy*, Springer-Verlag (2014).

[155] B. C. Jacobs and J. D. Franson, *All-optical switching using the quantum Zeno effect and two-photon absorption*, Phys. Rev. A **79**, 063830 (2009).

[156] S. M. Hendrickson, C. N. Weiler, R. M. Camacho, P. T. Rakich, A. I. Young, M. J. Shaw, T. B. Pittman, J. D. Franson, and B. C. Jacobs, *All-optical-switching demonstration using two-photon absorption and the Zeno effect*, Phys. Rev. A **87**, 023808 (2013).

[157] K. W. Martin, G. Phelps, N. D. Lemke, M. S. Bigelow, B. Stuhl, M. Wojcik, M. Holt, I. Coddington, M. W. Bishop, and J. H. Burke, *Compact optical atomic clock based on a two-photon transition in rubidium*, Phys. Rev. Applied **9**, 014019 (2018).

[158] J. D. Franson, T. B. Pittman, and B. C. Jacobs, *Zeno logic gates using micro-cavities*, J. Opt. Soc. Am. B **24**, 209–213 (2007).

[159] G. Grynberg and B. Cagnac, *Doppler-free multiphotonic spectroscopy*, Rep. Prog. Phys. **40**, 791 (1977).

[160] F. Biraben, B. Cagnac, and G. Grynberg, *Experimental evidence of two-photon transition without Doppler broadening*, Phys. Rev. Lett. **32**, 643–645 (1974).

[161] M. D. Levenson and N. Bloembergen, *Observation of two-photon absorption without Doppler broadening on the* $3S - 5S$ *transition in sodium vapor*, Phys. Rev. Lett. **32**, 645–648 (1974).

[162] S. Wang, J. Yuan, L. Wang, L. Xiao, and S. Jia, *A stable frequency standard based on the one-color two-photon 5S–7S transition of rubidium at 760 nm*, Laser Phys. Lett. **16**, 125204 (2019).

[163] N. Bloembergen, M. D. Levenson, and M. M. Salour, *Zeeman effect in the two-photon* $3S-5S$ *transition in sodium vapor*, Phys. Rev. Lett. **32**, 867–869 (1974).

[164] S. Gulde, H. Häffner, M. Riebe, G. Lancaster, C. Becher, J. Eschner, F. Schmidt-Kaler, I. L. Chuang, and R. Blatt, *Quantum information processing with trapped Ca+ ions*, Philos. T. Roy. Soc. A **361**, 1363–1374 (2003).

[165] T. W. Hänsch, *Nobel Lecture: Passion for precision*, Rev. Mod. Phys. **78**, 1297–1309 (2006).

[166] T. W. Hänsch, S. A. Lee, R. Wallenstein, and C. Wieman, *Doppler-free two-photon spectroscopy of hydrogen* $1S - 2S$, Phys. Rev. Lett. **34**, 307–309 (1975).

[167] A. Matveev, C. G. Parthey, K. Predehl, J. Alnis, A. Beyer, R. Holzwarth, T. Udem, T. Wilken, N. Kolachevsky, M. Abgrall, D. Rovera, C. Salomon, P. Laurent, G. Grosche, O. Terra, T. Legero, H. Schnatz, S. Weyers, B. Altschul, and T. W. Hänsch, *Precision measurement of the hydrogen* $1S-2S$ *frequency via a 920-km fiber link*, Phys. Rev. Lett. **110**, 230801 (2013).

[168] K. D. Bonin and T. J. McIlrath, *Two-photon electric-dipole selection rules*, J. Opt. Soc. Am. B **1**, 52–55 (1984).

[169] N. Melikechi and L. Allen, *Two-photon electric-dipole selection rules and nondegenerate real intermediate states*, J. Opt. Soc. Am. B **3**, 41–44 (1986).

[170] K. Y. Bliokh, Y. Gorodetski, V. Kleiner, and E. Hasman, *Coriolis effect in optics: Unified geometric phase and spin-Hall effect*, Phys. Rev. Lett. **101**, 030404 (2008).

[171] G. Tkachenko, I. Toftul, C. Esporlas, A. Maimaiti, F. Le Kien, V. G. Truong, and S. Nic Chormaic, *Light-induced rotation of dielectric microparticles around an optical nanofiber*, Optica **7**, 59–62 (2020).

[172] F. Le Kien and A. Rauschenbeutel, *Negative azimuthal force of nanofiber-guided light on a particle*, Phys. Rev. A **88**, 063845 (2013).

[173] F. Le Kien, J. Q. Liang, K. Hakuta, and V. I. Balykin, *Field intensity distributions and polarization orientations in a vacuum-clad subwavelength-diameter optical fiber*, Opt. Commun. **242**, 445–455 (2004).

[174] M. F. Andersen, C. Ryu, P. Cladé, V. Natarajan, A. Vaziri, K. Helmerson, and W. D. Phillips, *Quantized rotation of atoms from photons with orbital angular momentum*, Phys. Rev. Lett. **97**, 170406 (2006).

[175] R. Jones, G. Buonaiuto, B. Lang, I. Lesanovsky, and B. Olmos, *Collectively enhanced chiral photon emission from an atomic array near a nanofiber*, Phys. Rev. Lett. **124**, 093601 (2020).

[176] C. S. Wood, S. C. Bennett, D. Cho, B. P. Masterson, J. L. Roberts, C. E. Tanner, and C. E. Wieman, *Measurement of parity nonconservation and an anapole moment in cesium*, Science **275**, 1759–1763 (1997).

[177] B. J. Wundt, C. T. Munger, and U. D. Jentschura, *Quantum dynamics in atomic-fountain experiments for measuring the electric dipole moment of the electron with improved sensitivity*, Phys. Rev. X **2**, 041009 (2012).

[178] A. D. Tranter, H. J. Slatyer, M. R. Hush, A. C. Leung, J. L. Everett, K. V. Paul, P. Vernaz-Gris, P. K. Lam, B. C. Buchler, and G. T. Campbell, *Multiparameter optimisation of a magneto-optical trap using deep learning*, Nat. Commun. **9**, 4360 (2018).

[179] J.-B. Béguin, E. M. Bookjans, S. L. Christensen, H. L. Sørensen, J. H. Müller, E. S. Polzik, and J. Appel, *Generation and detection of a sub-Poissonian atom number distribution in a one-dimensional optical lattice*, Phys. Rev. Lett. **113**, 263603 (2014).

[180] S. T. Dawkins, R. Mitsch, D. Reitz, E. Vetsch, and A. Rauschenbeutel, *Dispersive optical interface based on nanofiber-trapped atoms*, Phys. Rev. Lett. **107**, 243601 (2011).

[181] C. G. Townsend, N. H. Edwards, C. J. Cooper, K. P. Zetie, C. J. Foot, A. M. Steane, P. Szriftgiser, H. Perrin, and J. Dalibard, *Phase-space density in the magneto-optical trap*, Phys. Rev. A **52**, 1423–1440 (1995).

[182] R. K. Hanley, P. Huillery, N. C. Keegan, A. D. Bounds, D. Boddy, R. Faoro, and M. P. A. Jones, *Quantitative simulation of a magneto-optical trap operating near the photon recoil limit*, J. Mod. Optic. **65**, 667–676 (2018).

[183] P. B. Wigley, P. J. Everitt, A. van den Hengel, J. W. Bastian, M. A. Sooriyabandara, G. D. McDonald, K. S. Hardman, C. D. Quinlivan, P. Manju, C. C. N. Kuhn, I. R. Petersen, A. N. Luiten, J. J. Hope, N. P. Robins, and M. R. Hush, *Fast machine-learning online optimization of ultra-cold-atom experiments*, Sci. Rep. **6**, 25890 (2016).

[184] E. T. Davletov, V. V. Tsyganok, V. A. Khlebnikov, D. A. Pershin, D. V. Shaykin, and A. V. Akimov, *Machine learning for achieving Bose-Einstein condensation of thulium atoms*, Phys. Rev. A **102**, 011302 (2020).

[185] K. Schawinski, C. Zhang, H. Zhang, L. Fowler, and G. K. Santhanam, *Generative adversarial networks recover features in astrophysical images of galaxies beyond the deconvolution limit*, Mon. Not. R. Astron. Soc. **467**, L110–L114 (2017).

[186] J. Wang, Y. Ma, L. Zhang, R. X. Gao, and D. Wu, *Deep learning for smart manufacturing: Methods and applications*, J. Manuf. Syst. **48**, 144–156 (2018).

[187] Y. LeCun, Y. Bengio, and G. Hinton, *Deep learning*, Nature **521**, 436–444 (2015).

[188] I. Goodfellow, Y. Bengio, and A. Courville, *Deep learning*, MIT Press (2016).

[189] D. Hendrycks and K. Gimpel, *Gaussian error linear units (gelus)*, arXiv preprint arXiv:1606.08415 (2016).

[190] A. Krogh and J. Hertz, *A simple weight decay can improve generalization*, Adv. Neur. In. **4** (1991).

[191] D. P. Kingma and J. Ba, *Adam: A method for stochastic optimization*, arXiv preprint arXiv:1412.6980 (2014).

[192] R. H. Byrd, P. Lu, J. Nocedal, and C. Zhu, *A limited memory algorithm for bound constrained optimization*, SIAM J. Sci. Comput. **16**, 1190–1208 (1995).

[193] P. Solano, F. K. Fatemi, L. A. Orozco, and S. L. Rolston, *Dynamics of trapped atoms around an optical nanofiber probed through polarimetry*, Opt. Lett. **42** (2017).

[194] A. S. Zibrov, M. D. Lukin, L. Hollberg, and M. O. Scully, *Efficient frequency up-conversion in resonant coherent media*, Phys. Rev. A **65**, 051801 (2002).

[195] F. E. Becerra, R. T. Willis, S. L. Rolston, and L. A. Orozco, *Nondegenerate four-wave mixing in rubidium vapor: The diamond configuration*, Phys. Rev. A **78**, 013834 (2008).

[196] R. T. Willis, F. E. Becerra, L. A. Orozco, and S. L. Rolston, *Four-wave mixing in the diamond configuration in an atomic vapor*, Phys. Rev. A **79**, 033814 (2009).

[197] G. Walker, A. S. Arnold, and S. Franke-Arnold, *Trans-spectral orbital angular momentum transfer via four-wave mixing in Rb vapor*, Phys. Rev. Lett. **108**, 243601 (2012).

[198] M. Parniak and W. Wasilewski, *Interference and nonlinear properties of four-wave-mixing resonances in thermal vapor: Analytical results and experimental verification*, Phys. Rev. A **91**, 023418 (2015).

[199] A. M. Akulshin, I. Novikova, E. E. Mikhailov, S. A. Suslov, and R. J. McLean, *Arithmetic with optical topological charges in stepwise-excited Rb vapor*, Opt. Lett. **41**, 1146–1149 (2016).

[200] R. F. Offer, J. W. C. Conway, E. Riis, S. Franke-Arnold, and A. S. Arnold, *Cavity-enhanced frequency up-conversion in rubidium vapor*, Opt. Lett. **41**, 2177–2180 (2016).

[201] D. J. Whiting, R. S. Mathew, J. Keaveney, C. S. Adams, and I. G. Hughes, *Four-wave mixing in a non-degenerate four-level diamond configuration in the hyperfine Paschen–Back regime*, J. Mod. Optic. **65**, 713–722 (2018).

[202] R. F. Offer, D. Stulga, E. Riis, S. Franke-Arnold, and A. S. Arnold, *Spiral bandwidth of four-wave mixing in Rb vapour*, Commun. Phys. **1**, 84 (2018).

[203] R. W. Boyd, *Nonlinear optics*, Academic Press (2020).

[204] N. Bloembergen, *Conservation laws in nonlinear optics∗*, J. Opt. Soc. Am. **70**, 1429–1436 (1980).

[205] A. M. Akulshin, R. J. McLean, A. I. Sidorov, and P. Hannaford, *Coherent and collimated blue light generated by four-wave mixing in Rb vapour*, Opt. Express **17**, 22861–22870 (2009).

[206] A. Vernier, S. Franke-Arnold, E. Riis, and A. S. Arnold, *Enhanced frequency up-conversion in Rb vapor*, Opt. Express **18**, 17020–17026 (2010).

[207] P. Kolchin, S. Du, C. Belthangady, G. Y. Yin, and S. E. Harris, *Generation of narrow-bandwidth paired photons: Use of a single driving laser*, Phys. Rev. Lett. **97**, 113602 (2006).

[208] J. K. Thompson, J. Simon, H. Loh, and V. Vuletic, *A high-brightness source of narrowband, identical-photon pairs*, Science **313**, 74–77 (2006).

[209] Q.-F. Chen, B.-S. Shi, M. Feng, Y.-S. Zhang, and G.-C. Guo, *Non-degenerate nonclassical photon pairs in a hot atomic ensemble*, Opt. Express **16**, 21708–21713 (2008).

[210] R. T. Willis, F. E. Becerra, L. A. Orozco, and S. L. Rolston, *Correlated photon pairs generated from a warm atomic ensemble*, Phys. Rev. A **82**, 053842 (2010).

[211] B. Srivathsan, G. K. Gulati, B. Chng, G. Maslennikov, D. Matsukevich, and C. Kurtsiefer, *Narrow band source of transform-limited photon pairs via four-wave mixing in a cold atomic ensemble*, Phys. Rev. Lett. **111** (2013).

[212] A. M. Akulshin, R. J. McLean, E. E. Mikhailov, and I. Novikova, *Distinguishing nonlinear processes in atomic media via orbital angular momentum transfer*, Opt. Lett. **40**, 1109–1112 (2015).

[213] J. E. Sharping, M. Fiorentino, A. Coker, P. Kumar, and R. S. Windeler, *Four-wave mixing in microstructure fiber*, Opt. Lett. **26**, 1048–1050 (2001).

[214] H. Takesue and K. Inoue, *Generation of polarization-entangled photon pairs and violation of Bell's inequality using spontaneous four-wave mixing in a fiber loop*, Phys. Rev. A **70**, 031802 (2004).

[215] M. Halder, J. Fulconis, B. Cemlyn, A. Clark, C. Xiong, W. J. Wadsworth, and J. G. Rarity, *Nonclassical 2-photon interference with separate intrinsically narrowband fibre sources*, Opt. Express **17**, 4670–4676 (2009).

[216] A. R. McMillan, J. Fulconis, M. Halder, C. Xiong, J. G. Rarity, and W. J. Wadsworth, *Narrowband high-fidelity all-fibre source of heralded single photons at 1570 nm*, Opt. Express **17**, 6156–6165 (2009).

[217] A. A. Shukhin, J. Keloth, K. Hakuta, and A. A. Kalachev, *Heralded single-photon and correlated-photon-pair generation via spontaneous four-wave mixing in tapered optical fibers*, Phys. Rev. A **101**, 053822 (2020).

[218] A. M. Yao and M. J. Padgett, *Orbital angular momentum: origins, behavior and applications*, Adv. Opt. Photon. **3**, 161–204 (2011).

[219] S. Franke-Arnold, L. Allen, and M. Padgett, *Advances in optical angular momentum*, Laser & Photon. Rev. **2**, 299–313 (2008).

[220] L. Allen, M. W. Beijersbergen, R. J. C. Spreeuw, and J. P. Woerdman, *Orbital angular momentum of light and the transformation of Laguerre-Gaussian laser modes*, Phys. Rev. A **45**, 8185–8189 (1992).

[221] B. E. A. Saleh and M. C. Teich, *Fundamentals of photonics*, John Wiley & Sons (2019).

[222] V. Gerginov and K. Beloy, *Two-photon optical frequency reference with active ac Stark shift cancellation*, Phys. Rev. Applied **10**, 014031 (2018).

[223] Y. Ohtake, T. Ando, N. Fukuchi, N. Matsumoto, H. Ito, and T. Hara, *Universal generation of higher-order multiringed Laguerre-Gaussian beams by using a spatial light modulator*, Opt. Lett. **32**, 1411–1413 (2007).

[224] N. Prajapati, N. Super, N. R. Lanning, J. P. Dowling, and I. Novikova, *Optical angular momentum manipulations in a four-wave mixing process*, Opt. Lett. **44**, 739–742 (2019).

[225] J. Petersen, J. Volz, and A. Rauschenbeutel, *Chiral nanophotonic waveguide interface based on spin-orbit interaction of light*, Science **346**, 67–71 (2014).

[226] A. Browaeys, D. Barredo, and T. Lahaye, *Experimental investigations of dipole–dipole interactions between a few Rydberg atoms*, J. Phys. B: At. Mol. Opt. **49**, 152001 (2016).

[227] B. Olmos, M. Müller, and I. Lesanovsky, *Thermalization of a strongly interacting 1D Rydberg lattice gas*, New J. Phys. **12**, 013024 (2010).

[228] K. S. Rajasree, T. Ray, K. Karlsson, J. L. Everett, and S. Nic Chormaic, *Generation of cold Rydberg atoms at submicron distances from an optical nanofiber*, Phys. Rev. Res. **2**, 012038 (2020).

[229] M. Daly, V. G. Truong, C. F. Phelan, K. Deasy, and S. N. Chormaic, *Nanostructured optical nanofibres for atom trapping*, New J. Phys. **16**, 053052 (2014).

[230] C. M. Bishop and N. M. Nasrabadi, *Pattern recognition and machine learning*, Springer (2006).

Appendix A

Guided Modes of a Step-Index Fiber

A.1 Eigenvalue Equations

We consider a step-index fiber that is a dielectric cylinder of radius a and refractive index n_1 surrounded by an infinite background medium of refractive index n_2, where $n_2 < n_1$. The wave equation of light propagation in such a fiber can be derived from Maxwell's equations and is given by [113],

$$\nabla^2 \boldsymbol{\mathcal{E}} - \mu_0 \epsilon(\mathbf{r}) \frac{\partial^2 \boldsymbol{\mathcal{E}}}{\partial t^2} = -\vec{\nabla}\left(\frac{\boldsymbol{\mathcal{E}}}{\epsilon(\mathbf{r})} \cdot \vec{\nabla}\epsilon(\mathbf{r})\right). \tag{A.1}$$

Here, $\boldsymbol{\mathcal{E}}$ denotes the electric field vector, μ_0 the vacuum permeability, and ϵ the electric permittivity of the medium. The wave equation for the magnetic field $\boldsymbol{\mathcal{H}}$ takes the same form as Equation A.1. For a cylindrical symmetric waveguide, it is convenient to derive the field components in cylindrical coordinates (r, θ, φ), and the solutions of Equation A.1 for the axial component take the simple form of

$$\begin{bmatrix} \mathcal{E}_z(\mathbf{r}, t) \\ \mathcal{H}_z(\mathbf{r}, t) \end{bmatrix} = \begin{bmatrix} \mathcal{E}_z(r, \varphi) \\ \mathcal{H}_z(r, \varphi) \end{bmatrix} e^{i(\omega t - \beta z)}, \tag{A.2}$$

where β is the axial propagation constant of the field. Moreover, employing Maxwell's equations in cylindrical coordinates, the radial and azimuthal components can be expressed in terms of $\mathcal{E}_z$ and $\mathcal{H}_z$

$$\begin{aligned}
\mathcal{E}_r &= \frac{-i\beta}{\omega^2\mu\epsilon - \beta^2}\left(\frac{\partial \mathcal{E}_z}{\partial r} + \frac{\omega\mu}{\beta}\frac{\partial \mathcal{H}_z}{r\partial\varphi}\right) \\
\mathcal{E}_\varphi &= \frac{-i\beta}{\omega^2\mu\epsilon - \beta^2}\left(\frac{\partial \mathcal{E}_z}{r\partial\varphi} - \frac{\omega\mu}{\beta}\frac{\partial \mathcal{H}_z}{\partial r}\right) \\
\mathcal{H}_r &= \frac{-i\beta}{\omega^2\mu\epsilon - \beta^2}\left(\frac{\partial \mathcal{H}_z}{\partial r} - \frac{\omega\epsilon}{\beta}\frac{\partial \mathcal{E}_z}{r\partial\varphi}\right) \\
\mathcal{H}_\varphi &= \frac{-i\beta}{\omega^2\mu\epsilon - \beta^2}\left(\frac{\partial \mathcal{H}_z}{r\partial\varphi} + \frac{\omega\epsilon}{\beta}\frac{\partial \mathcal{E}_z}{\partial r}\right).
\end{aligned} \tag{A.3}$$

The solution of the whole problem can now be reduced to solving the wave equation for the z-component,

$$\left[\partial_r^2 + \frac{1}{r}\partial_r + \frac{1}{r^2}\partial_\varphi^2 + \kappa^2\right] \begin{bmatrix}\mathcal{E}_z(r,\varphi)\\ \mathcal{H}_z(r,\varphi)\end{bmatrix} = 0, \tag{A.4}$$

where $\kappa^2 = \mu_0\epsilon\omega^2 - \beta^2 = n^2k_0^2 - \beta^2$. The equation is separable with ansatz

$$\begin{bmatrix}\mathcal{E}_z(r,\varphi)\\ \mathcal{H}_z(r,\varphi)\end{bmatrix} = R(r)e^{\pm il\varphi}, \quad l \in \{0,1,2,\ldots\}. \tag{A.5}$$

Inserting Equation A.5 into Equation A.4 gives a Bessel differential equation for $R(r)$

$$\left[\partial_r^2 + \frac{1}{r}\partial_r + \left(\kappa^2 - \frac{l^2}{r^2}\right)\right] R(r) = 0. \tag{A.6}$$

For any lossless modes confined to the core, the axial propagation constant β is restricted as given by

$$n_2k_0 < \beta < n_1k_0. \tag{A.7}$$

The general solutions of Equation A.6 are Bessel functions of order l depending on the sign of κ^2 such that

$$R(r) = AJ_l(\kappa r) + BY_l(\kappa r), \kappa^2 > 0, \tag{A.8}$$
$$R(r) = CI_l(\kappa r) + DK_l(\kappa r), \kappa^2 < 0. \tag{A.9}$$

Here, $J_l(\kappa r)$ and $Y_l(\kappa r)$ are the Bessel functions of the first and second kind, and $I_l(\kappa r)$ and $K_l(\kappa r)$ are the modified Bessel functions of the first and second kind, respectively, all of order l. Since, Y_l is singular at $r = 0$ and I_l diverges as $r \to \infty$, $B = C = 0$ for physically reasonable solutions. The field components E_z and H_z can now be expressed inside the core ($r < a$) as

$$E_z(\mathbf{r},t) = A_E J_l(hr)\exp\{i(\omega t \pm l\varphi - \beta z)\}, \tag{A.10}$$
$$H_z(\mathbf{r},t) = A_H J_l(hr)\exp\{i(\omega t \pm l\varphi - \beta z)\}, \tag{A.11}$$
$$\text{with } h = \sqrt{n_1^2k_0^2 - \beta^2}, \tag{A.12}$$

and outside the core ($r > a$) as

$$E_z(\mathbf{r},t) = D_E J_l(qr)\exp\{i(\omega t \pm l\varphi - \beta z)\}, \tag{A.13}$$
$$H_z(\mathbf{r},t) = D_H J_l(qr)\exp\{i(\omega t \pm l\varphi - \beta z)\}, \tag{A.14}$$
$$\text{with } q = \sqrt{\beta^2 - n_2^2k_0^2}. \tag{A.15}$$

The normalization constants A_E, A_H, D_E and D_H as well as β can be obtained by considering the boundary conditions. The tangential components $E_{\varphi,z}$, $H_{\varphi,z}$ are continuous

at the core-cladding boundary, i.e.,

$$\begin{aligned} E_{\varphi,z}(r=a)|_{core} &= E_{\varphi,z}(r=a)|_{cladding}, \\ H_{\varphi,z}(r=a)|_{core} &= H_{\varphi,z}(r=a)|_{cladding}. \end{aligned} \tag{A.16}$$

These considerations together with Equations A.1, A.2, A.3, A.12, and A.15 yield the following relations for the constants A_E, A_H, D_E and D_H

$$\begin{aligned} A_E J_l(ha) - D_E K_l(qa) &= 0 \\ A_E\left[\frac{i(\pm l)}{h^2 a}J_l(ha)\right] + A_H\left[-\frac{\omega\mu_0}{h\beta}J_l'(ha)\right] + D_E\left[\frac{i(\pm l)}{q^2 a}K_l(ha)\right] + D_H\left[-\frac{\omega\mu_0}{q\beta}K_l'(ha)\right] &= 0 \\ A_H J_l(ha) - D_H K_l(qa) &= 0 \\ A_E\left[\frac{\omega\epsilon_1}{h\beta}J_l'(ha)\right] + A_H\left[\frac{i(\pm l)}{h^2 a}J_l(ha)\right] + D_E\left[\frac{\omega\epsilon_2}{q\beta}K_l'(qa)\right] + D_H\left[\frac{i(\pm l)}{q^2 a}K_l(qa)\right] &= 0 \end{aligned} \tag{A.17}$$

Equation A.17 has a solution only when the determinant of the coefficients vanishes. This requirement leads to the mode condition that determines the propagation constant β of each mode

$$\left(\frac{J_l'(ha)}{haJ_l(ha)} + \frac{K_l'(qa)}{qaK_l(qa)}\right)\left(\frac{n_1^2 J_l'(ha)}{haJ_l(ha)} + \frac{n_2^2 K_l'(qa)}{qaK_l(qa)}\right) = l^2\left[\left(\frac{1}{ha}\right)^2 + \left(\frac{1}{qa}\right)^2\right]\left(\frac{\beta}{k_0}\right)^2. \tag{A.18}$$

The coefficients A_E, A_H, D_E and D_H can be determined by employing the solution for β and the power of the electromagnetic field.

$$\begin{aligned} \frac{D_E}{A_E} &= \frac{J_l(ha)}{K_l(ha)}, \\ \frac{A_H}{A_E} &= \frac{i\beta(\pm l)}{\omega\mu_0}\left[\left(\frac{1}{ha}\right)^2 + \left(\frac{1}{qa}\right)^2\right]\left(\frac{J_l'(ha)}{haJ_l(ha)} + \frac{K_l'(qa)}{qaK_l(qa)}\right)^{-1} \\ \frac{D_H}{A_E} &= \frac{D_E A_H}{A_E^2} \end{aligned} \tag{A.19}$$

The factor A_E can be determined from the total transmitted power P via the relation,

$$A_E = \sqrt{\frac{4\mu_0\omega P}{\pi a^2\beta}}(D_{in} + D_{out})^{-1/2}, \tag{A.20}$$

with

$$\begin{aligned} D_{in} = (1-s)(1+(1-s)\frac{\beta^2}{h^2})(J_0^2(ha) + J_1^2(ha)) \\ + (1+s)(1+(1+s)\frac{\beta^2}{h^2})(J_2^2(ha) - J_1(ha)J_3(ha)), \end{aligned} \tag{A.21}$$

$$D_{out} = \big[(1-s)(1-(1-s)\frac{\beta^2}{q^2})(K_0^2(qa) - K_1^2(qa)) \\ + (1+s)(1-(1+s)\frac{\beta^2}{q^2})(K_2^2(qa) - K_1(qa)K_3(qa))\big]. \tag{A.22}$$

To write the above expressions we used the notation s given by

$$s = \left[\left(\frac{1}{ha}\right)^2 + \left(\frac{1}{qa}\right)^2\right]\left(\frac{J_l'(ha)}{haJ_l(ha)} + \frac{K_l'(qa)}{qaK_l(qa)}\right)^{-1}. \tag{A.23}$$

A.1.1 Fundamental mode HE_{11}

The expression of the electric field components for a quasi-circularly polarized fundamental mode are given as follows.
Outside the fiber (where $r > a$):

$$E_r(r,\varphi,z,t) = -iA_E\frac{\beta}{2h}\left[(1-s)J_0(hr) - (1+s)J_2(hr)\right]\exp i(\omega t \pm \varphi - \beta z), \\ E_\varphi(r,\varphi,z,t) = \pm A_E\frac{\beta}{2h}\left[(1-s)J_0(hr) + (1+s)J_2(hr)\right]\exp i(\omega t \pm \varphi - \beta z), \\ E_z(r,\varphi,z,t) = A_E J_1(hr)\exp i(\omega t \pm \varphi - \beta z). \tag{A.24}$$

Inside the fiber (where $r < a$):

$$E_r(r,\varphi,z,t) = -iA_E\frac{\beta}{2q}\frac{J_1(ha)}{K_1(qa)}\left[(1-s)K_0(hr) + (1+s)K_2(hr)\right]\exp i(\omega t \pm \varphi - \beta z), \\ E_\varphi(r,\varphi,z,t) = \pm A_E\frac{\beta}{2q}\frac{J_1(ha)}{K_1(qa)}\left[(1-s)K_0(hr) - (1+s)K_2(hr)\right]\exp i(\omega t \pm \varphi - \beta z), \\ E_z(r,\varphi,z,t) = A_E\frac{J_1(ha)}{K_1(ha)}K_1(hr)\exp i(\omega t \pm \varphi - \beta z). \tag{A.25}$$

Appendix B

Explicit expressions for $u_{ij}^{(q)}$ matrices

The expressions for the $u_{ij}^{(q)}$ matrices are taken directly from [123].

$$
\begin{aligned}
u^{(2)} &= \frac{1}{2}\begin{pmatrix} 1 & -i & 0 \\ -i & -1 & 0 \\ 0 & 0 & 0 \end{pmatrix}, \\
u^{(1)} &= \frac{1}{2}\begin{pmatrix} 0 & 0 & -1 \\ 0 & 0 & i \\ -1 & i & 0 \end{pmatrix}, \\
u^{(0)} &= \frac{1}{\sqrt{6}}\begin{pmatrix} -1 & 0 & 0 \\ 0 & -1 & 0 \\ 0 & 0 & 2 \end{pmatrix}, \\
u^{(-1)} &= \frac{1}{2}\begin{pmatrix} 0 & 0 & 1 \\ 0 & 0 & i \\ 1 & i & 0 \end{pmatrix}, \\
u^{(-2)} &= \frac{1}{2}\begin{pmatrix} 1 & i & 0 \\ i & -1 & 0 \\ 0 & 0 & 0 \end{pmatrix}.
\end{aligned}
\tag{B.1}
$$

Appendix C

Explicit expressions for $\{\boldsymbol{A} \otimes \boldsymbol{B}\}_{Kq}$ tensors

$$
\begin{aligned}
\{\boldsymbol{A} \otimes \boldsymbol{B}\}_{0,0} &= -\frac{1}{\sqrt{3}} (\boldsymbol{A} \cdot \boldsymbol{B}), \\
\{\boldsymbol{A} \otimes \boldsymbol{B}\}_{1,-1} &= \frac{1}{\sqrt{2}} (A_0 B_{-1} - A_{-1} B_0), \\
\{\boldsymbol{A} \otimes \boldsymbol{B}\}_{1,0} &= -\frac{1}{\sqrt{2}} (A_1 B_{-1} - A_{-1} B_1), \\
\{\boldsymbol{A} \otimes \boldsymbol{B}\}_{1,1} &= \frac{1}{\sqrt{2}} (A_1 B_0 - A_0 B_1), \\
\{\boldsymbol{A} \otimes \boldsymbol{B}\}_{2,-2} &= A_{-1} B_{-1}, \\
\{\boldsymbol{A} \otimes \boldsymbol{B}\}_{2,-1} &= \frac{1}{\sqrt{2}} (A_{-1} B_0 + A_0 B_{-1}), \\
\{\boldsymbol{A} \otimes \boldsymbol{B}\}_{2,0} &= \frac{1}{\sqrt{6}} (A_1 B_{-1} + 2 A_0 B_0 + A_{-1} B_1), \\
\{\boldsymbol{A} \otimes \boldsymbol{B}\}_{2,1} &= \frac{1}{\sqrt{2}} (A_1 B_0 + A_0 B_1), \\
\{\boldsymbol{A} \otimes \boldsymbol{B}\}_{2,2} &= A_1 B_1.
\end{aligned}
\tag{C.1}
$$

Appendix D

Deep Learning

In general machine learning refers to any process that attempts to find an algorithmic solution to a particular problem using computational means. This is typically achieved by starting with some mathematical model representing a map from inputs to outputs and iteratively adjusting the free parameters until a desired output is achieved. The process of incrementally adjusting the model parameters is referred to as training/learning. This will not necessarily be a unique model, but it is a model with some measure of accuracy. A model is good if it is able to generalize and perform well on task outside the set of training data.

Construction of a model that can represent data in some meaningful way and potentially provide a useful mapping is a problem that has existed in machine learning since its conception. Deep learning techniques provide a convenient and computationally efficient means to perform such a mapping. Deep learning in essence refers to the representation of a mapping from input to output data using multiple layers of adaptive nonlinear elements.

D.1 Artificial neural networks (ANNs)

The building blocks of deep learning approaches are known as ANNs, which are layers of connected elements which can be used to approximate functions. The term neural network has its origins in attempts to find mathematical representations of information processing in biological brains [230]. A base structure of such a neural network is an artificial neuron that performs the mapping

$$f(\mathcal{X}) = h(\mathcal{X} \cdot \mathbf{W} + \mathbf{B}), \tag{D.1}$$

where $\mathcal{X}$ is the input data, $f(\mathcal{X})$ is the output, h is some nonlinear activation function where the input is scaled by some weight matrix $\mathbf{W}$, and $\mathbf{B}$ is a bias term. This structure can be used to represent a function through a feed-forward neural network model also known as multilayer perceptron, where multiple layers of the base structure with adaptive parameters describe a series of functional transformations to approximate a target function. The function can be represented in the form of a network diagram as shown in Figure D.1. Typically as the complexity of the function we wish to approximate increases so will the number of layers and neurons needed to represent this

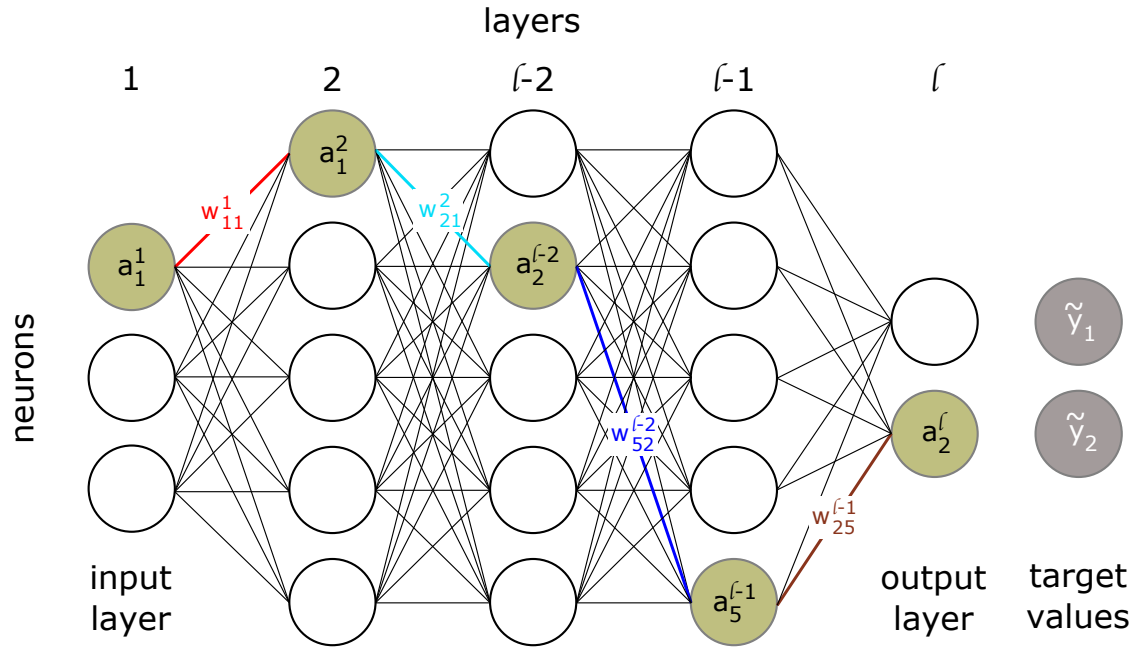

Figure D.1: Neural network diagram for a fully-connected five layers network. The input to output mapping is achieved through three hidden layers consisting neurons connected with weight parameters represented by links between the nodes. The output of the network together with the target values determines the cost function for the network.

function.

D.2 Network training

The goal of training is to be able to find the set of network parameters for which the model function approximates an arbitrary target function. Let us suppose we have some model $f(\mathcal{X};\boldsymbol{\theta})$ such that the mapping $f : \mathcal{X} \to \mathcal{Y}$ is subject to the model parameters $\boldsymbol{\theta}$. The goal is to be able to determine $\boldsymbol{\theta}$. In particular, for each parameter $\theta_i \in \boldsymbol{\theta}$, the aim is to find a set of rules that can be iteratively applied to reach an accurate representation of the desired function. A simple rule is gradient descent that adds small corrections to the parameters proportional to the gradient of a cost function at each time step

$$\theta_i^{t+1} = \theta_i^t - \eta \frac{\partial C\left(\mathcal{X}, \theta_i^t\right)}{\partial \theta_i}, \tag{D.2}$$

where the t in the superscript denotes the time step, $C\left(\mathcal{X}, \theta_i^t\right)$ is the cost function and η is an adaptive scaling factor that describes the learning rate [191]. A cost function is some measure of accuracy of the model, rather its deviation from actual target value, the choice of which depends on the specific application. One such choice of cost function

is the mean squared error (MSE) given by

$$\text{MSE} = \frac{1}{N}\sum_{i=1}^{m}\left(\mathcal{Y}_i - \tilde{\mathcal{Y}}_i\right)^2, \tag{D.3}$$

where $\tilde{\mathcal{Y}}$ are the target values and m is the number of samples of training data.

D.3 Backpropagation

It is clear from Equation D.2 that we need an efficient technique for evaluating the gradient of the cost function for a neural network. In a general feed-forward network (see Figure D.1), each unit (neuron) computes a weighted sum of its inputs of the form

$$a_j^{m+1} = h\left(\sum_i w_{ji}^m a_i^m + b_i^m\right) \tag{D.4}$$

where h is a nonlinear activation function, a_i^m are the neurons in the m-th layer, b_i^m are the associated biases, and w_{ji}^m are the weights representing the strengths of the connections between the neurons in the consecutive layers. Our aim is to determine $\partial C/\partial\theta$ where the parameters, θ, are the weights, biases, and values of each neurons. We introduce a notation z_j^{m+1}, such that

$$z_j^{m+1} = \sum_i w_{ji}^m a_i^m + b_i^m. \tag{D.5}$$

Now consider the evaluation of the derivative of the cost, C, with respect to a weight w_{ji}^{l-1} associated with the final layer, l. The partial derivative of the cost function can be expressed explicitly using chain rule as

$$\frac{\partial C}{\partial w_{ji}^{l-1}} = \frac{\partial z_j^l}{\partial w_{ji}^{l-1}}\frac{\partial a_j^l}{\partial z_j^l}\frac{\partial C}{\partial a_j^l}. \tag{D.6}$$

Each of these terms can be calculated easily. The first term is simply the output from the previous neuron, a_i^{l-1}. The second term is the derivative of the activation function. And the final term is the change in cost with respect to the output of the network. For mean squared error with a single training it is simply reduces to $2(a_k^l - \tilde{y}_k)$.

Similarly the partial derivative of the cost with respect to weights, w_{ji}^{l-2} can be expressed as

$$\frac{\partial C}{\partial w_{ji}^{l-2}} = \frac{\partial z_j^{l-1}}{\partial w_{ji}^{l-2}}\frac{\partial a_j^{l-1}}{\partial z_j^{l-1}}\frac{\partial C}{\partial a_j^{l-1}}. \tag{D.7}$$

The expression is similar to the one in Equation D.6, with the first term simply being the output of neuron in the previous layer, a_i^{l-2}, and the second term being the derivative of the activation function. The third term corresponds to the change in cost due to change in the neuron a_j^{l-1}. Any change in a_j^{l-1} affects the cost through all the connections in l-th layer. The third term is then obtained by summing over all the

neurons in the final layer,

$$\frac{\partial C}{\partial a_j^{l-1}} = \sum_k \frac{\partial z_k^l}{\partial a_j^{l-1}} \frac{\partial a_k^l}{\partial z_k^l} \frac{\partial C}{\partial a_k^l}. \tag{D.8}$$

The first term is w_{kj}^{l-1}. The second and the third term are common to the ones in Equation D.6 and are calculated to find the gradient of the cost for final layer. Once calculated these terms could be propagated backwards to subsequently calculate the gradients with respect to the parameters in every preceding layers. This is how back-propagation works. Starting with the final layer, the gradients with respect to all the network parameters could be computed.